GROWTH, OPTICAL AND STRUCTURAL INVESTIGATION OF SIGE NANOSTRUCTURES

Ioana Carmen Mărcuș

PhD thesis

Supervisor: Dr. Maria Isabel Alonso Carmona

Co-Supervisor: Dr. Alejandro Goñi

Tutor UAB: Prof. Javier Rodriguez-Viejo

Physics Department

Universidad Autónoma de Barcelona - ICMAB

2012

Instituto de Ciencia de Materiales de Barcelona - ICMAB

Nanostructured Optoelectronic Materials

Universidad Autónoma de Barcelona

GROWTH, OPTICAL AND STRUCTURAL INVESTIGATION OF SIGE NANOSTRUCTURES

Ioana Carmen Mărcuș

PhD thesis

2012

Summary

The main purpose of this thesis has been to develop a new process in order to achieve reproducible control of the dimensions and spatial location of Ge nanostructures (islands and nanowires) formed on Si substrates. In this context, our primary objective was to form bi-dimensional arrays of Au nanoclusters using mass-filtered focused ion beam (FIB) with Au^{2+} ions and to use them as patterns to nucleate the Ge nanostructures.

The **first chapter** is dedicated to a review of: 1) Si and Ge fundamental properties, 2) generalities about the SiGe alloy layers, and 3) growth of the self assembled Ge islands and nanowires. Details about the nanostructure growth mode are exposed. The nanowire growth mechanism – vapor liquid solid (VLS) – is described along with the Au behavior as a catalyst.

Chapter 2 gives an overview of the patterning (focused ion beam) and growth (molecular beam epitaxy) techniques. Besides them, methods for sample characterization from a morphological and optical point of view are described.

The **third chapter** is devoted to investigate the influence of Ge nanoclustering on the composition and strain determination of $Si_{1-x}Ge_x/Si$ alloys. The cause of the large scatter of the phonon frequency values measured by Raman for relaxed alloy layers that is found in the literature was revealed as due to Ge nanoclustering effects. This phenomenon occurs in SiGe alloy layers as a result of employing nonequilibrium epitaxial growth methods such as molecular beam epitaxy. The obtained alloy layers presenting Ge nanoclusters were thermally treated and the effect of the cumulative annealings of randomizing the Ge atom distribution within the alloy layer was demonstrated. Additionally, we proved that the strain and composition of the SiGe alloy layers can be evaluated and determined by performing a single Raman measurement. An analytical/graphical method to estimate the Ge composition and strain status within the SiGe alloy layers independent of their strain status was elaborated.

The growth of the Ge nanostructures on patterned Si substrates was investigated and is presented in **chapter 4**. For this purpose a three step process was developed, based mainly on: i) focused ion beam (FIB) patterning, ii) annealing and iii) molecular beam epitaxy growth. Si substrates with different crystallographic orientations [(001) and (111)] were patterned using a FIB equipment with Au^{2+} ions. Pattern evolution as a consequence of the employed FIB parameters was examined, and their progress with the thermal treatments performed using a large range of temperatures and times was explored. The formation of AuSi clusters inside the FIB patterned areas during the annealings was achieved. Depending on the ion dose used to pattern the substrates, after Ge deposition, both islands and/or nanowires were formed. The effect of the Au amount and hole dimensions on the growth mode, morphology, and two-dimensional ordering of the nanostructures was investigated.

Resumen

El propósito principal de esta tesis ha sido desarrollar un nuevo proceso con el fin de lograr el control reproducible de las dimensiones y la ubicación espacial de nanoestructuras (islas y nano hilos) de Ge sobre sustratos de Si. En este contexto, nuestro objetivo básico era formar matrices bidimensionales de nanocúmulos de Au utilizando haces de iones focalizados (FIB) de Au^{2+} con filtro de masas y posteriormente utilizarlos como patrón para la nucleación de nanoestructuras de Ge.

El **primer capítulo** está dedicado a la revisión de: 1) las propiedades fundamentales de Si y Ge, 2) generalidades sobre las capas de aleación de SiGe y 3) el crecimiento de islas y nano hilos de Ge auto-ensamblados. Se han expuesto los detalles sobre el modo de crecimiento de las nanoestructuras. El mecanismo de crecimiento para los nano hilos - vapor líquido sólido (VLS) - se describe junto con el comportamiento del Au como catalizador.

El **segundo capítulo** ofrece una visión general de las tecnologías de grabado (haces de iones focalizados) y crecimiento (epitaxia por haces moleculares). Además, se describen los métodos para la caracterización de las muestras, tanto morfológica como desde un punto de vista óptico.

El **tercer capítulo** está dedicado a investigar la influencia de la formación de nanocúmulos de Ge sobre la determinación de la composición y de la tensión de capas de aleaciones de $Si_{1-x}Ge_x/Si$. La causa de la gran dispersión de los valores de las frecuencias Raman de fonones medidos en capas de aleación relajadas que se encuentra en los datos de la literatura se reveló que estaba relacionada con la existencia de los nanocúmulos de Ge. Su presencia dentro de las capas de aleación de SiGe es el resultado de haber empleado métodos de crecimiento epitaxial de no equilibrio, tales como la epitaxia por haces moleculares. Las capas de aleación obtenidas en este trabajo que contenían nanocúmulos de Ge se trataron térmicamente y el efecto de dichos recocidos acumulativos para conseguir una disposición aleatoria de los átomos de Ge dentro de la

capa de aleación fue demostrado. Adicionalmente, hemos demostrado que la tensión de las capas de SiGe y su composición pueden ser evaluadas y determinadas mediante la realización de una sola medición Raman. Se elaboró también un método gráfico para estimar la composición en Ge y el estado de tensión dentro de las capas de aleación de SiGe independiente de su estado de tensión.

El crecimiento de las nanoestructuras de Ge en substratos de Si grabados se ha presentado en el **cuarto capítulo**. Se ha investigado y desarrollado un proceso en tres pasos basado principalmente en: i) el uso de haces de iones focalizados (FIB) para obtener los patrones, ii) recocido y iii) el crecimiento de nanoestructuras mediante epitaxia por haces moleculares (MBE). Se grabaron sustratos de silicio con distintas orientaciones cristalográficas (Si (001) y Si (111)) usando un equipo de haces de iones de Au^{2+} focalizados. Se examinó la variación de los patrones en función de los parámetros FIB empleados, y se exploró su evolución al realizar tratamientos térmicos utilizando una amplia gama de temperaturas y tiempos. Durante los recocidos se logró la formación de cúmulos de AuSi dentro de las áreas grabadas con el FIB. Después de la deposición de Ge se formaron islas y/o nano hilos dependiendo de la dosis de iones utilizada para grabar los sustratos. También se investigó el efecto de la cantidad de Au y de las dimensiones de los hoyos sobre el modo de crecimiento y la morfología de las nanoestructuras formadas.

TABLE OF CONTENTS

Chapter 1. Fundamentals of *SiGe* semiconductors

1.1 Properties of Si, Ge materials……………………………..…………………1

1.1.1 Elements of silicon and germanium…………………..………….....2

1.2 GeSi/Si nanostructures……………………………….……..…………….....…6

1.2.1 Model of thin film growth………………………..…………….…..….7

1.2.2 $Si_{1-x}Ge_x$ alloy layers…………………………………..…..…....…….8

1.2.3 Ge islands formation on Si substrates……………..………….…….12

1.2.3.1 Self assembly of Ge islands on Si substrates ……………..…15

1.3 Nanowires…………………………………………………..……………17

1.3.1 What is a nanowire?..17

1.3.2 Semiconductor nanowires………………………………………..17

1.3.3 Short history of the Si, Ge nanowires …………………………...…18

1.3.4 Nanowire growth ………………………………………….…………19

1.3.4.1 Nanowire growth techniques……………………….…………20

1.3.4.2 Vapor Liquid Solid mechanism………………………...…21

1.3.4.3 Gold as catalyst……………………..…………………....23

1.4 Bibliography…………………………………………………………..…..26

Chapter 2. Experimental techniques

2.1 Patterning and growth methods……………………………………………34
2.1.1 Focused Ion Beam……………………………………………...…34
2.1.1.1 Generalities…………………………………………….34
2.1.1.2 Focused ion beam equipment description………….……....36
2.1.2 Molecular Beam Epitaxy……………………………………...38
2.1.2.1 Molecular Beam Epitaxy overview……………………38
2.1.2.1 Molecular Beam Epitaxy equipment description…………40
2.2 Optical characterization techniques………………………...……...…..43
2.2.1 Raman spectroscopy…………………………………………….43
2.2.2 X-ray Diffraction…………………………………………...…44
2.2.3 Spectroscopic ellipsometry………………………………………..44
2.3 Imaging techniques…………………………………………………………46
2.3.1 Atomic Force Microscopy……………………………………….46
2.3.2 Scanning Electron Microscopy…………………………………..47
2.4 Bibliography…………………………………………………………………48

Chapter 3. Influence of Ge nanoclustering on the determination by Raman scattering of composition and strain in $Si_{1-x}Ge_x$/Si alloys

3.1 State of the art and motivation……………………………………………50
3.2 Samples growth conditions…………………………………………………53
3.3 Some theoretical considerations……………………………………….…..56
3.4 Origin of the scatter in the ω_0 values…………………………………...58
3.5 Determination of Ge content through a single Raman measurement…...66
3.6 Conclusions…………………………………………………………………74
3.7 Bibliography……………………………………………………….…...…75

Chapter 4. Growth of Ge nanostructures on *focused ion beam* patterned Si substrates

4.1 Introduction…………………………………………………………………....79
4.2 Samples preparation…………………………………………………………..81
4.3 Self assembled Ge islands growth on Si substrates patterned by a focused ion beam……………………………………………………………………………...84
4.3.1 Ultra fast grabbing process – single scan……………………….....84
4.3.2 Ultra fast grabbing process – multiple scans………………………86
4.3.3 AuSi clusters formation inside the FIB imaged areas…………...…90
4.4 Ge nanostructures formation on hole patterned Si substrates…………..92
4.4.1 Focused ion beam parameters influence on the Si substrates morphology……………………………………………………………………..…..92
4.4.2 Influence of the annealing conditions on the evolution of Si patterned substrates morphology…………………………………………………………….....100
4.4.2.1 Evolution of the Si patterned substrates morphology with annealing conditions……………………………………………………101
4.4.2.2 AuSi clusters formation inside patterned Si substrates….109
4.4.3 Growth of Ge nanostructures on hole patterned Si substrates as a function of ion dose……………………………………………………………………..112
4.4.3.1 Low ion dose…………………………………………......112
4.4.3.2 Intermediate ion dose…………………………………....123
4.3.3.3 High ion dose……………………………………………142
4.5 Conclusions…………………………………………………………...146
4.6 Bibliography…………………………………………………………148

Acknowledgments……………………………………………………………....153

List of publications and conferences attended...…….……………………....155

Chapter 1

Fundamentals of *SiGe* semiconductors

1.1 Properties of Si, Ge materials

Silicon (Si) is the material dominating semiconductor industry since 1970s, and Si based devices nowadays account for over 97% of all microelectronics. The reason is very simple. Silicon is the cheapest microelectronic technology for integrated circuits [1]. Furthermore, Si is the second richest element available in the earth crust, so we should not be worried about the natural resources. However, the electric and optical properties of Si itself, such as low carrier mobilities and indirect bandgap, make it less ideal and efficient for some advanced microelectronic devices. For this reason, significant studies have been carried out for the past two decades in order to improve the material properties of Si by various approaches, among which Silicon-Germanium (SiGe) technology is one of the most important and promising ways. Germanium (Ge) addition to Si implies different characteristics for the resulting alloy materials, offering new applications in a wide range of electronic devices [2].

The first paper on silicon and germanium can be traced back to 1955, presenting results on the magneto-resistance of SiGe alloys [3]. The first mention of a SiGe device was actually in the patent for the bipolar transistor where the idea of a SiGe heterojunction bipolar transistor (HBT) was discussed [4]. Such a transistor required epitaxial growth of Si/SiGe heterostructures and this was not achieved until 1975 using molecular beam epitaxy [5]. Since then the study of the heterostructures was mainly

motivated by the possible application in micro and nanoelectronic devices. The field has substantially extended in the 1980s, being dominated by the development of growth technology, then in the 1990s by HBT developments and the beginning of the 2000s has been dominated by strained-Si complementary metal - oxide - semiconductor (CMOS). The new requirements of much more complex heterostructures in the new device architectures demanded to develop further knowledge and techniques in terms of growth and characterizations, in order to obtain such high-quality SiGe/Si heterostructures with desired material properties.

1.1.1 Elements of silicon and germanium

Both, Si and Ge crystallize in the diamond lattice structure. This structure can be regarded as two face centered cubic (fcc) Bravais lattices displaced to each other one quarter of the space diagonal. In the diamond lattice, each atom is bonded to four equivalent nearest-neighbor atoms located at the corner positions of a tetrahedron. One conventional cubic cell contains four such tetrahedrons. The diamond structure for column IV elements (Si and Ge in this particular case) is the result of the directional covalent bonding through sharing the four valence electrons of one atom with its four nearest neighbors. A conventional cubic cell of diamond lattice with lattice constant a_0 is depicted in figure 1.1, where the covalent bonds between neighboring atoms are represented by the rods.

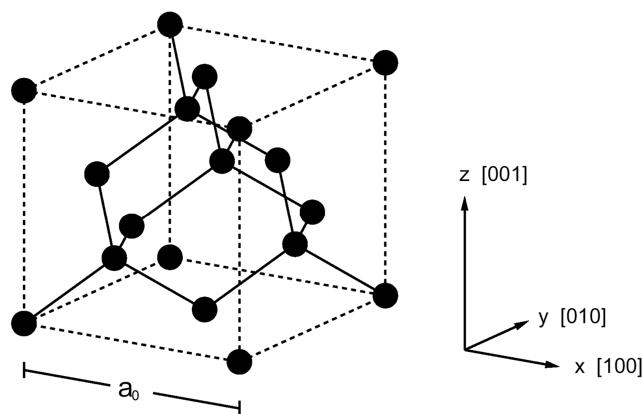

Figure 1.1. *Diamond lattice structure of Si and Ge.*

At 300 K, the lattice constants of Si and Ge are 5.4310 Å and 5.6575 Å, respectively [6]. The reciprocal lattice of the fcc Bravais lattice for the diamond structure is the body-centered cubic (bcc) lattice. Figure 1.2 shows the first Brillouin zone of fcc lattice, together with indications of high symmetry points and lines.

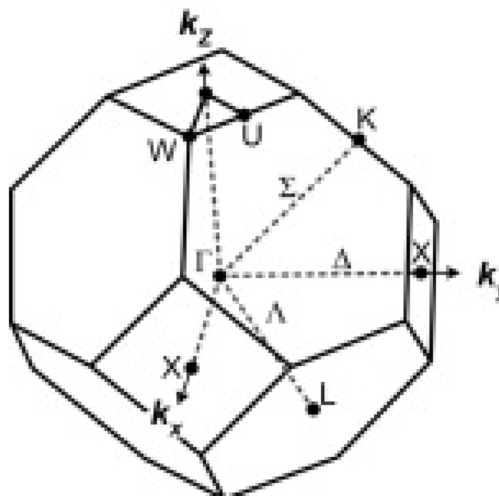

Figure 1.2. *The first Brillouin zone of fcc lattice. Important symmetry points (Γ, X, L, K, W, and U) and lines (Δ Λ, and Σ) are indicated.*

Si and Ge are both indirect bandgap semiconductors, where the lowest conduction band minima and highest valence band maxima are located at different positions in reciprocal space (***k*** space). The valence band maximum for Si and Ge is located at ***k***=0 (i.e. Γ-point), corresponding to the degenerate heavy-hole (HH) and light-hole (LH) subbands. The spin-orbit (SO) subband is lower in energy by the spin-orbit splitting energy Δ_{SO}. The major difference between Si and Ge occurs in the conduction band. Si has six-fold degenerate conduction band minima at $\boldsymbol{k}\approx 0.85\times(2\pi/a)$ away from the Γ-point along the Δ-directions (<100> - directions) towards X-points. The conduction band minima for Ge are located at L points along <111> - directions at the Brillouin zone boundary.

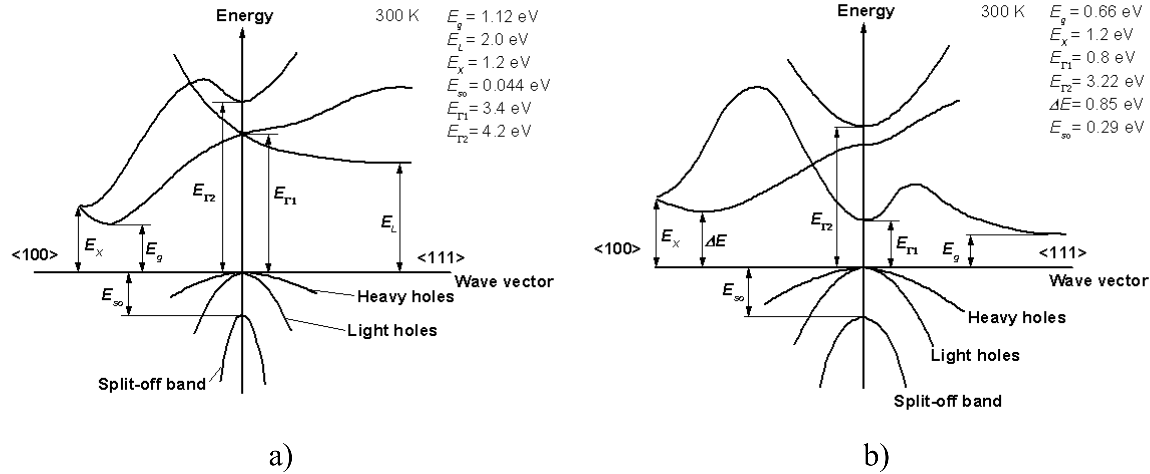

Figure 1.3. *Band structure of (a) Si and (b) Ge. Figures extracted from http://www.ioffe.rssi.ru/SVA/NSM/Semicond/SiGe/bandstr.html [7].*

The band structures for the two elements - Si and Ge - are presented in figure 1.3. A comparison between silicon and germanium properties is presented in table 1.1, in order to point out the differences between the two elements.

Table 1.1. Important physical constants of intrinsic Si and Ge at 300 K.

Property	**Silicon**	**Germanium**
Atomic number	14	32
Relative atomic mass	28.0855[8]	72.59[8]
Lattice Constant *a* (Å)	5.431 [9]	5.6575[9]
Lattice mismatch to Si (%)	0	4.2
Melting Point (°C)	1414 [10]	938.3 [10]
Thermal conductivity κ (W/cm°C)	1.5 [11]	0.6 [11]
Effective electron masses (m_0)		
m_l	0.916 [12]	1.59 [12]
m_t	0.191 [12]	0.082 [12]
Effective heavy-hole mass m_{hh} (m_0)	0.537 [12]	0.284 [12]
Effective light-hole mass m_{lh} (m_0)	0.153 [12]	0.044 [12]
Mobility (bulk)		
Electron μ_e (cm^2/V s)	1500 [12]	3900 [12]

Hole μ_h (cm^2/V s)	450 [12]	1900 [12]
Band gap (bulk)		
Direct (eV)	3.4 [7]	0.8 [7]
Indirect (eV)	1.12 [7]	0.66 [7]

1.2 GeSi/Si nanostructures

Due to the conservation constrains for energy and momentum, the band-to-band optical transitions in indirect bandgap semiconductors usually involve interactions with phonons, which causes slow and inefficient transition processes. Therefore, Si, Ge and their alloys are in general considered as poor materials for most optical applications, especially for light emission. With the development of epitaxial growth and other fabrication techniques, semiconductor nano-structures can nowadays be obtained with a precise control down to atomic scale. As the geometrical dimension of nanometer-size structures is comparable with the de Broglie wavelength of the carriers, *quantum mechanical effects* take place. In particular, these quantum structures provide the possibility to enhance the optical properties of indirect bandgap semiconductor systems, such as Ge/Si. A quantum structure can be formed, for example, by embedding a semiconductor within another semiconductor having a larger bandgap. Energy barriers arising at abrupt heterointerfaces due to sharp band discontinuities lead to the ***quantum confinement effect of carriers***. The characteristics of confined carriers are described through the *density of states* (DOS), defined as the number of electronic states per unit volume and energy.

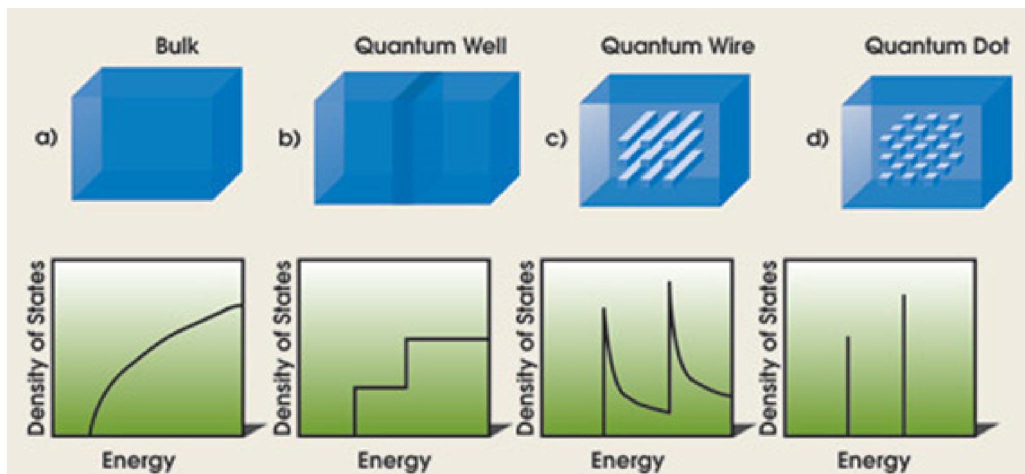

Figure 1.4. *Schematic illustrations of a bulk, quantum well, quantum wire and quantum dot structure, together with plots of their corresponding density of states. Figure extracted from reference 14.*

Depending on the physical shape of the narrow-gap material and hence the dimension of carrier confinement, semiconductor quantum structures can be classified as ***quantum wells*** (QW), ***quantum wires*** (QWr), and ***quantum dots*** (QD) [15], as shown in figure 1.4. Utilizing the tunable bandgap energy of SiGe coupled with strain effects, all kinds of quantum structures can be formed. Reduction in size in one or more dimensions causes a discrete energy spectrum.

1.2.1 Model of thin film growth

The growth of epitaxial (homogenous or heterogeneous) thin films on a single crystal surface depends critically on the interaction strength between adatoms and the surface. It is well known that there are three types of growth modes for heterogeneous epitaxial growth including the Ge/Si system: the Frank-van der Merwe [16], Stranski-Krastanow [17], and Volmer-Weber [18] modes, named after the original researchers. Schematic representation of the three main growth modes is presented in figure 1.5. The typical layer-by-layer growth is referred to as ***Frank-van der Merwe*** growth, which is required to fabricate high-quality large films for practical applications. During Frank-van der Merwe growth, adatoms attach preferentially to surface sites resulting in atomically smooth, fully formed layers. This layer-by-layer growth is two dimensional (2D), indicating that complete films form prior to growth of subsequent layers. ***Stranski-Krastanow*** growth is an intermediary process characterized by both 2D layer and 3D island growth, where growth starts in a layer-by-layer mode during the first few atomic layers, and then forms 3D islands beyond a certain thickness, which is usually referred to as *critical thickness*. Critical layer thickness is highly dependent on the chemical and physical properties, such as surface energies and lattice parameters, of the substrate and film. In this type of growth the strain energy due to the lattice mismatch is reduced by islands formation. An increase of surface energy due to the greater surface/bulk ratio of a dots collection with respect to a 2D growth partially compensates the decrease in energy [19]. For some heterogeneous epitaxial growth conditions, where there is, for example, a substantial lattice mismatch, layer-by-layer growth is impossible and only 3D islands are formed. This growth is referred to as ***Volmer-Weber*** growth. In Volmer-Weber growth, adatom-adatom interactions are stronger than those of the adatom with the surface, leading to the formation of three-dimensional adatom clusters or islands. The growth

modes are determined by equilibrium of the energy balance between surface energy of the layer, substrates and islands, interfacial energy between them and elastic strain energy associated with lattice mismatch.

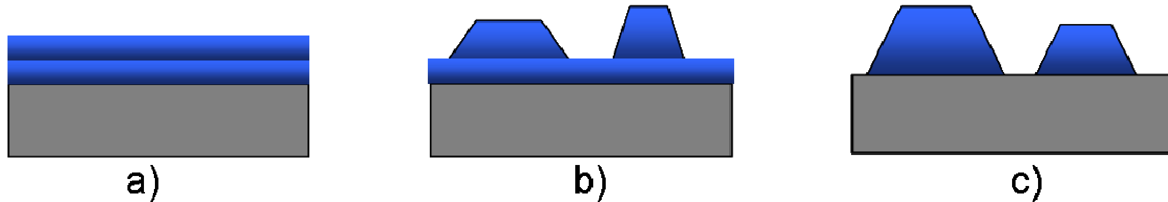

Figure 1.5. *Thin film growth modes: a) Frank-van der Merwe (FM: layer-by-layer), b) Stranski-Krastanow (SK: layer plus island), and c) Volmer-Weber (VW: island formation).*

1.2.2 $Si_{1-x}Ge_x$ alloy layers

Silicon-germanium alloys are one the most studied semiconductors and a large amount of data has been published. The alloy exhibits complete solid solubility across the entire phase space. Below, ~170 K, theory suggests there could be a spinodal decomposition regime. However, the atomic mobilities at such a temperature would prevent decomposition of an existing alloy on any time scale. The Si-Ge phase diagram is shown in figure 1.6 [20]. The equilibrium spinodal decomposition boundary in the lower figure is the solid curve, while the dashed curve shows the expected region of strong instability. The low-temperature spinodal is expected based on the parameters found for fitting the melting behavior.

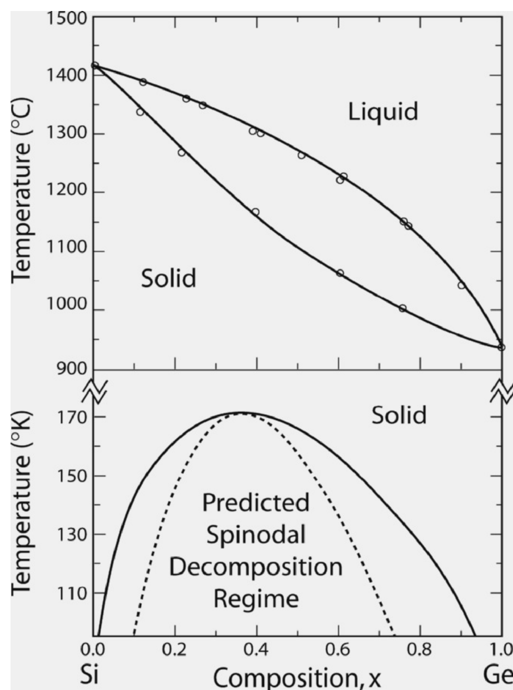

Figure 1.6. *The phase diagram for Si-Ge binary alloys. Figure extracted from reference 20.*

Since silicon and germanium have the same crystallographic structure and are completely miscible, they can form $Si_{1-x}Ge_x$ alloys with x ranging from 0 to 1. SiGe alloys have a fcc Bravais lattice with the diamond structure. The lattice constant (a_{SiGe}) of $Si_{1-x}Ge_x$ across the entire x range has been measured by Dismukes et al. [9]. Alloy lattice constant versus composition is shown in figure 1.7. The experimental results revealed a slight deviation of ~10^{-4} Å from Vegard's law:

$$a_{SiGe} = a_{Si}(1-x) + a_{Ge} \cdot x \qquad 1.1$$

where a_{SiGe}, a_{Si}, a_{Ge} are the lattice parameters for SiGe alloy, Si and Ge.

The nonlinear dependence of the SiGe unstrained lattice constant on Ge composition is well approximated by the equation 1.2 [21], with higher precision:

$$a_{SiGe} = a_{Si}(1-x) + a_{Ge} \cdot x - 0.026174 \cdot x \cdot (1-x) \qquad 1.2$$

In the above equations $a_{Si} = 5.4310$ Å is the lattice constant for Si, and $a_{Ge} = 5.6575$ Å is the lattice constant for Ge [6]. One should be cautious on using these values because they are temperature dependent, and the results at this level of accuracy are for 300 K. The values at other temperatures will be significantly modified.

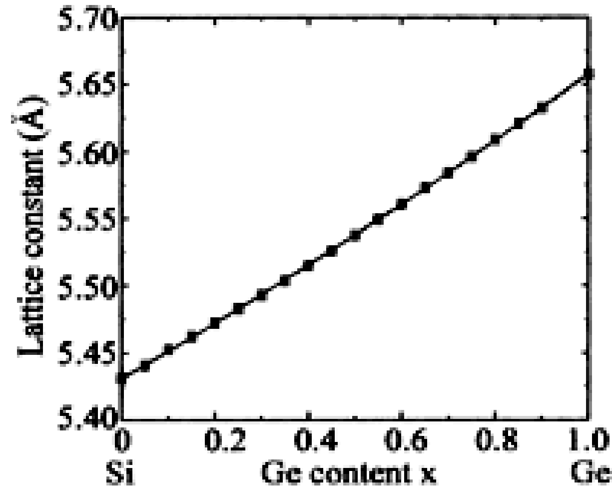

Figure 1.7. *$Si_{1-x}Ge_x$ alloy layer lattice constant (a_{SiGe}) as a function of Ge composition (x).*

Due to the misfit of 4.2% between Ge and Si, the alloy lattice parameter will be higher than that of the Si, as represented in figure 1.8 (relaxed case). When a thin semiconductor layer is epitaxially grown on another semiconductor substrate with a different lattice parameter, the in-plane lattice constant of the layer could be constrained to fit with that of the substrate. This so-called *pseudomorphic* growth mode (see figure 1.8) thus introduces the biaxial elastic strain in the growth plane of the epilayer [22]. As the layer material tries to preserve its volume, the uniaxial strain governed by the Poisson effect is simultaneously generated in the direction perpendicular to the growth plane, resulting in a tetragonal distortion of the lattice. However, there exits a limit for accommodating the lattice mismatch between two semiconductors by elastic strain. The mismatch between film and substrate is usually accommodated by a network of misfit dislocations lying in the interface and by elastic strain of the film [23]. The structures start to relax plastically and tend to recuperate the cubic symmetry with lattice parameter characteristic for a SiGe relaxed alloy. The deposition of pseudomorphic SiGe layers requires low temperature process technique [2].

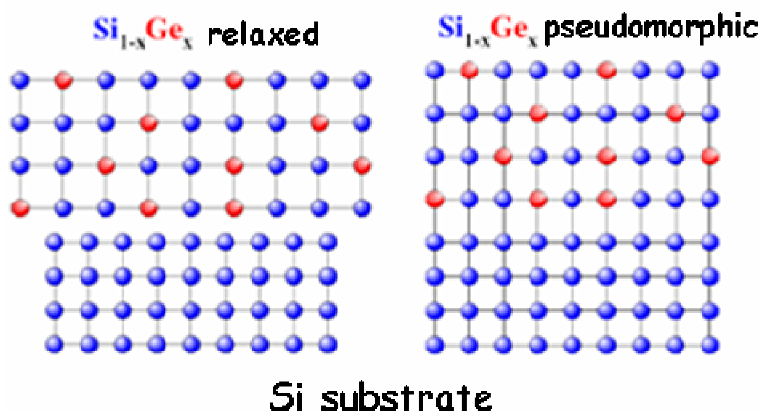

Figure 1.8. *Heteroepitaxial growth of $Si_{1-x}Ge_x$ alloy layers on Si substrates: left hand – relaxed case, and right hand – pseudomorphic growth.*

Phase diagram for semiconductor alloys was calculated (see figure 1.6), but many crystal growth methods result in non-equilibrium materials. Because of their strong bonds and refractory natures, semiconductors usually have low atomic diffusion rates. Consequently, if an alloy can be induced to form during growth of the material, it is generally found to be sufficiently stable to be used, if not heated too much. Such an alloy, which is thermodynamically unstable but kinetically stable, is referred to as ***metastable***. At room temperature these materials are often estimated, based on extrapolations from high temperature data, to be stable over effectively infinite times. Metastable alloys have been deposited as epitaxial thin films on a variety of substrates by a variety of techniques such as CVD and MBE. The Matthews and Blakeslee [24] critical thickness versus composition is plotted in figure 1.9 and corresponds to the boundary between the stable and metastable regions. The critical thickness limitation and the thermal stability (metastable layers) of strained SiGe films on Si cause severe limitations for the integration into Si process technology [2].

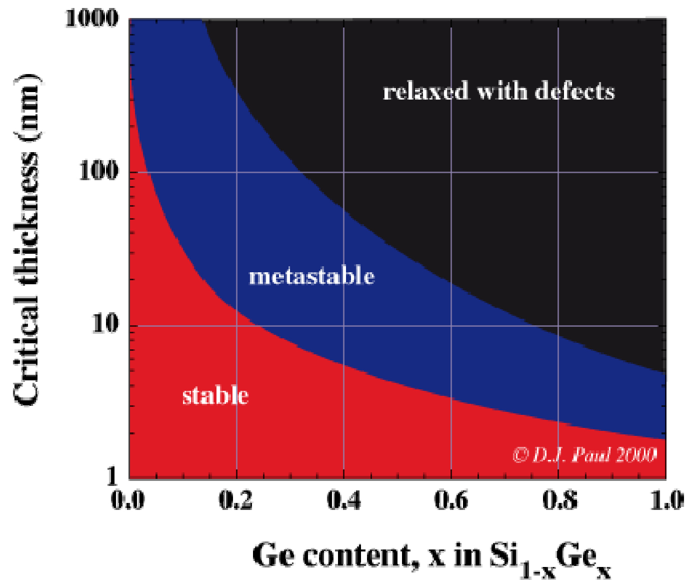

Figure 1.9. *The critical thickness versus Ge fraction for pseudomorphic $Si_{1-x}Ge_x$ layers grown on bulk (100) silicon. Figure also included the metastable curve for MBE growth at 550ºC. Figure extracted from reference 1.*

1.2.3 Ge islands formation on Si substrates

The growth of Ge on Si occurs in the Stranski-Krastanow mode [25], it begins initially in a layer-by-layer manner, followed by 3D Ge ***islands*** formation. The formation of the Ge islands is driven by the surface strain resulting from the lattice mismatch of ~4.2%. The growth of Ge on Si substrates has been extensively studied with a variety of surface analysis techniques [26-30], such as reflection high-energy electron diffraction (RHEED), Auger electron spectroscopy (AES), and low-energy electron diffraction (LEED). The value of the critical thickness ranges from 3 to 10 monolayers (MLs) before the start of appearance of Ge islands [31]. The actual number of MLs may vary with the growth temperature, growth techniques, or with the presence of a surfactant on the substrate. The formation of the Ge islands on Si substrates with different orientations is a spontaneous nucleation process. The two major island shapes are ***pyramids*** with small volumes and ***domes*** with much higher volume (see figure 1.10b). The appearance of two island varieties is referred to as *bimodal distribution* [32]. The dominant facet for pyramidal shapes is {105} which forms an angle of 11.3º with the substrate surface, while

domes are multifaceted, the most common facet being {113} with a 25º angle. Facets with other angles with respect to the surface can be also found. On passing from pyramids to domes shapes the relaxation level of mechanical stress in increased.

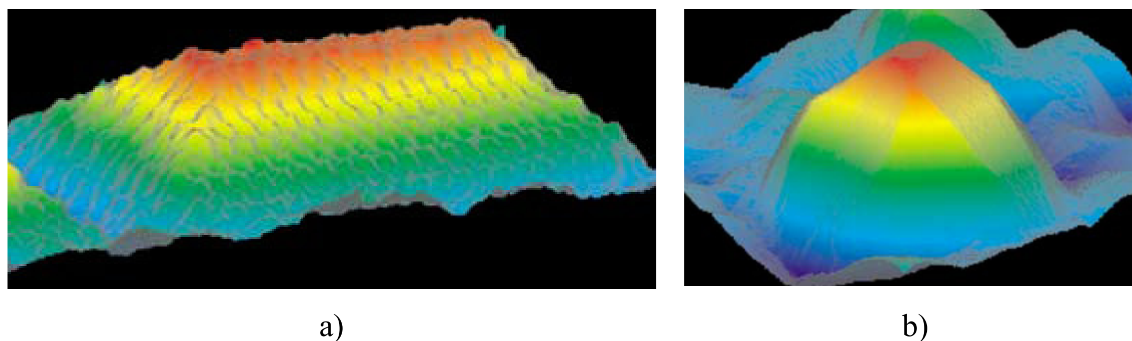

a) b)

Figure 1.10. *Perspective representation of a scanning transmission microscopy (STM) image of huts with facets {105} (a), and a multiple faceted dome (b). Figures extracted from reference 32.*

Besides these two islands types other shapes were observed too. Small islands can have pyramidal shape with a square base or elongated (in <100> or <010> directions) shape called ***huts*** with two trapezoidal and two triangular sides (see figure 1.10a). Depending on the growth temperature and the Ge amount deposited large pyramidal islands with a flat top, also known as ***truncated pyramids*** [15] were obtained. Large germanium deposition rate can generate the formation of ***superdomes***, which are the combination of some smaller islands. This size distribution of the islands is known as *trimodal or multimodal distribution* [33]. Figure 1.11 presents the phase diagram for different islands types as a function of the deposited amount and growth temperature as reported by Cimalla et al. [34].

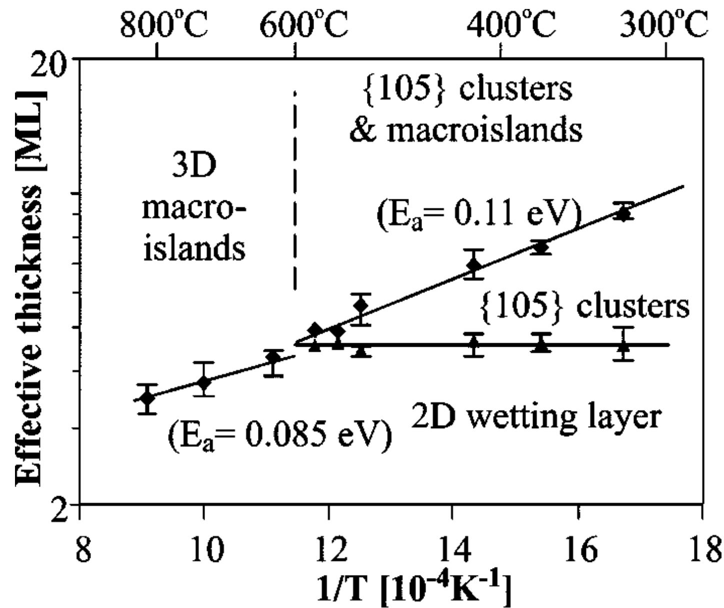

Figure 1.11. *Arrhenius plot of the Ge amount (equivalent to ML) at the transition from 2D to 3D growth and at the coalescence of {105} clusters to macroislands. Error bars correspond to experiments at three different growth rates. By macroislands are defined domes and superdomes types. Figure extracted from reference 34.*

In the growth process a central role is played by the Si substrate orientation. On both (001) and (111) Si substrate orientations the growth begins with a wetting layer (SK growth). Ge growth on a Si(001) substrate follows by the formation of islands with a square based and single faceted pyramids, and low aspect ratio. The growth involves a shape transition from small pyramids to multi faceted, round domes with high aspect ratio, allowing a higher degree of elastic strain relaxation [35, 36]. During the growth, island composition changes from nearly 100 % to 50 %, due to the increased intermixing with the Si substrate [37, 38]. On a (111) Si substrate the island density is usually lower than for the (001) orientation, and island size is larger. Their shape depends on the step direction on the substrates [39]. Theoretical models [39, 40-43] to explain the growth mechanism of the islands were developed.

1.2.3.1 Self assembly of Ge islands on Si substrates

For many practical applications of islands (quantum dots) in fields like micro and nanoelectronics, magnetism or molecular electronics it is needed to achieve a fine control of their size, density and position. Quantum dots (QDs) have to present some characteristic in order to be used in room temperature working devices like: i) QD size have to be so small to allow obtaining deep localized states due to the confinement; ii) QDs should present high uniformity and high volume filling factor; and iii) the material should be defects free [37, 41].

On a planar surface Ge islands nucleate randomly [42], without any order. The two main ways of ordering the islands are ***self-ordered*** and substrate ***pattern ordered***. The major challenge is to obtain self assembled islands arrays with predetermined positions. Island nucleation can be controlled by kinetics (surface diffusion barrier, sticking coefficient, etc.) and/or by energetic parameters (surface energy, step-edge energy, stress relaxation, chemistry, etc.). In the islands, self-ordering the atomic steps is expected to act as nucleation centers. The position of the islands can be controlled by the relative location of the steps. It was proved that step influence is a function of substrate orientation, stronger influences from it were observed on Si(111) as compared to Si(001) [44]. The strain can be also used to tune the islands position.

For substrate patterning various methods such as optical [46-48], holographic [49-51], electron beam [50-52], focused ion beam [53-55] as well as extreme UV interference lithography [56, 57] have been used, and different pattern geometries, including stripes [46, 49, 50], mesas [47], and pits with various sizes and shapes [48, 51-58] have been employed. For site-control of deposited quantum dots, the pattern morphology has to be controlled and the growth conditions tuned to the given template structure [50-58]. By now, patterns with different shapes and dimensions were successfully used to achieve an increased control in the Ge islands position on Si substrates [59, 60]. In addition, besides the shape of the pattern morphology, the growth conditions also determine quantum dot location on the surface. Temperature influence on the position of Ge islands grown on FIB patterned substrates was also reported [61]. All mentioned factors influence island position on patterned surfaces, being reported their formation at the center of the pits [51-58], in the middle of the grooves [49, 50], at sidewall [49, 50], at edges or ridges [46, 47, 52, 54, 56, 57]. Since patterns preservation is limited by the temperature range for thermal

treatments, a buffer layer was growth to remove surface roughness and/or defects produced by the patterning process [51, 53]. During buffer growth, however, the pattern morphology rapidly changes and directly influences the further growth of the islands, a high control of the process being required for the reproducibility of the results. The growth mechanism of the (Ge) islands on patterned surfaces changes compared to flat surfaces [62]. Both the pit-pattern period, as well as the amount of deposited Ge per area establishes the quantity of available material for the formation of a single island [62]. For planar substrates the excess of Ge deposition results in the incorporation of dislocations in the largest islands, and, subsequently, the formation of Ge rich super domes.

1.3 Nanowires

1.3.1 What is a nanowire?

Nanowires (NWs) are defined as nanostructures that have a thickness or diameter constrained to tens of nanometers or less and an unconstrained length (normally in the range of micrometers). Due to their aspect ratio (length/width ratio) of 1000 or more, nanowires are often referred to as one-dimensional (1D) materials. For device fabrication these nanostructures present particular interest as they exhibit quantum confinement effects in two dimensions, while the third is unrestricted [63]. The electrons in nanowires are quantum confined laterally and occupy energy levels that are different from the continuum of energy levels or bands in bulk materials.

In addition to general material properties as found in their bulk (3D) or thin-film (2D) counterparts, 1D semiconducting nanowires own some very unique properties such surface sensitivity, low leakage current, and scalability [64]. Basically, when structures approach the ~100 nm size regime their properties may change with decreasing size for the same atomic composition. In any case, 1D nanostructures are superior to their counterparts with larger dimensions. Their unique properties make them attractive candidates for many possible devices, founding lots of practical applications in electronics, optoelectronics, chemistry and even medicine field. Many different types of nanowires were reported, including metallic (e.g. Ni, Pt, Au) [65, 66], semiconducting (e.g. Si, Ge, ZnO, InAs, GaN) [67-72], insulating (e.g. SiO_2, TiO_2) [73, 74] but also molecular or organic [75]. In this work, the main interest is focused on semiconductor nanowires, particularly Ge NWs.

1.3.2 Semiconductor nanowires

Semiconductor nanowires are potential alternatives to conventional planar metal-oxide-semiconductor field-effect transistor (MOSFETs). Ge is attractive to build up devices due to its superior electronic properties with respect to Si and its compatibility with Si CMOS processing in contrast to III-V materials. Nanowire field-effect transistors

(FETs) have a unique electronic structure which can be exploited. Particularly, Ge NWs can serve as active channel material of a FET, and have to be assembled directly on insulator layer, electrically decoupled from silicon substrate. Nanowire based FET using high-k dielectrics in a top-gate geometry was reported [76]. Low temperature synthesis is necessary to implement ‘‘post-integration’’ of nanowire devices into CMOS platform in a hybrid chip technology (e.g., embedded nanowire memory array) to avoid unfavorable impact of added thermal treatments on the existing silicon devices [64].

Silicon and germanium nanowires have been studied for some years. Nanowire-based optoelectronic devices [77], including solar cells [78-80], photo detectors [81-83], photo resistors [84], optical modulators [85], light sources [63, 85, 86], visible light detectors [63] were stated.

1.3.3 Short history of Si, Ge nanowires

The formation of the Si nanowires was reported for the first time by Treuting and Arnold [87] in the 50s. They reported on the growth of Si “whiskers” with <111> orientation. At that time the name whisker was mostly employed. In the 60s Wagner and Ellis [88] proposed as growth mechanism for the formation of one dimensional whiskers with a seed catalyst the Vapor Liquid Solid (VLS). Their pioneer work opened new research fields for the investigation of the fundamental aspects of the wires growth. Until now this mechanism is the most used one for the growth of nanowires. Much attention was also paid to semiconductors, especially silicon and germanium, for a better understanding of more fundamental issues about the growth mechanism.

Research progress in this area during the years is quite impressive, the field winning more followers every year. The evolution during the last 50 years of the papers based on Si whisker, Si nanowires and Ge nanowires is shown in figure 1.12, to better see the research interest on this topic. In the 90s Si nanowires publication suffers a boom and outperformed whisker one. The research on the Si nanowires experienced a remarkable increase in intensity and is until today of great interest. Compared to Si nanowires, the Ge ones are less reported, but in the last years received an increased attention. The graph reflects the interest on Si and Ge nanowires.

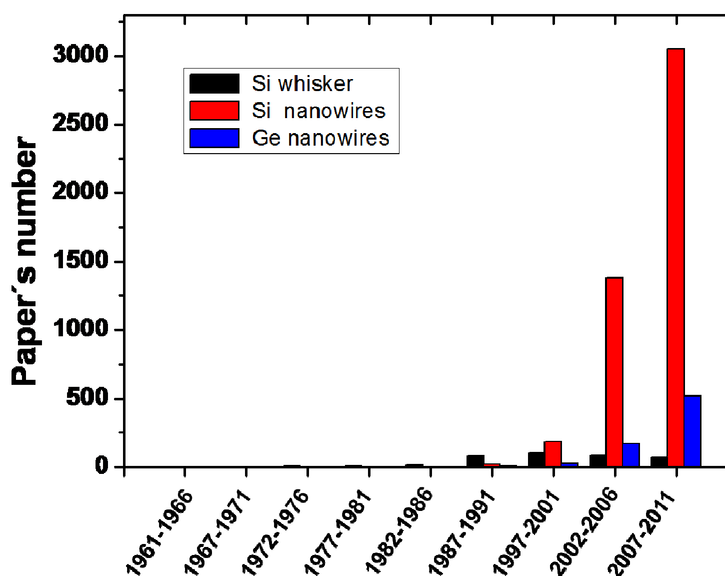

Figure 1.12. *Histogram of whisker, Si, and Ge nanowires based papers as a function of publication data. Source: ISI Web of Knowledge; search date November 2011.*

1.3.4 Nanowire growth

To produce the nanostructures in general, nanowires in particular, two general ways are accepted: “top-down“ and “bottom-up”. Using ***top-down*** approach the nanoscale dimensions are achieved using especially lithographic techniques. As starting point are used bulk materials of desired composition. The main problem with this approach is when the scale is reduced; is not so easy to find techniques that easily allow carving out the ultra small structures. Besides, the uniformity and quality of the nanostructures are also difficult to control. ***Bottom-up*** method imitates nature’s way of self-assembling atoms to produce increasingly large structures. The uniform and ordered nanostructures can be formed in solution, as particle in a vapor, or on solid substrates, using for the growth vapor or liquid sources. Over the past decade the epitaxial growth of nanowires won much attention and expanded rapidly. During the epitaxial growth, nanowire parameters like crystalline structure, length, diameter and even chemical composition can be well controlled [89-91].

1.3.4.1 Nanowire growth techniques

Semiconductor nanowires usually present the same crystal structure as bulk semiconductors. In order to obtain them, the crystal growth rate in one dimension has to be enhanced, and/or suppressed in the other dimensions. The two main types of nanowire growth are: template-directed and free-standing. Nanostructure growth by direct template with well defined shapes (figure 1.13a) is possible mainly by suppression of the growth in other dimensions [92]. In the case of the nanowire growth using a v-groove template (figure 1.13b) the nucleation takes place along the length of the template [93]. The so called "freestanding" nanowires are normally grown from one nucleation point, with confinement generated by the relative growth rates of the different dimensions. To grow these nanowires a lot of materials from vapor or solid and different substrates (or no substrates at all) can be used. Their size can be reduced to nanometric scale, but the integration within new devices is not so easy to achieve. The majority of the freestanding nanowires grow with the help of small seed particles of a foreign material (typically a metal) (figure 1.13c) [88]. The growth mode implying presence of droplets to promote nanowire growth was called Vapour Liquid Solid (VLS). Catalyst particles can be in solid or liquid phase, normally are not consumed during the growth process and induce an increase of the growth rate in one direction. More details on this growth mechanism can be found in next subsection. The last case presented in figure 1.13d show nanowire growth which does not need a seed particle. Oxide assisted growth and selected-area epitaxy are the most used ways to grow the nanowires from this category. The nanostructures formed in this way are of great interest for applications presenting high quality and highly controlled morphology and size, and overcome the contamination problems present for particle assisted nanowires.

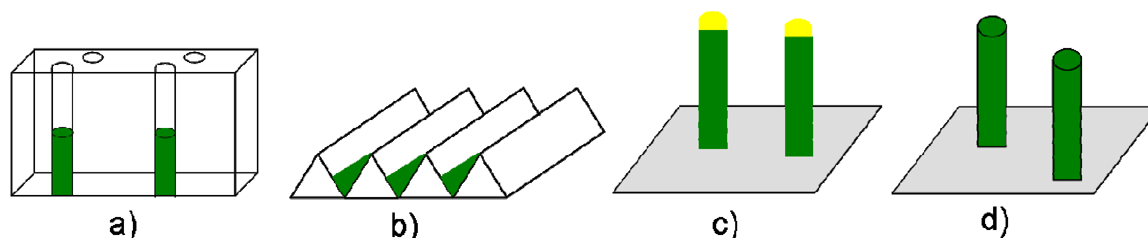

Figure 1.13. *Nanowire growth techniques: a) NW growth directed by a template; b) V-groove directed template growth; c) Particle-assisted freestanding growth; d) Particle-free (self-assembled) freestanding NW growth.*

Many growth techniques were used to form nanowires with different dimensions such as chemical vapor deposition (CVD) [94, 95], metal organic chemical vapor deposition (MOCVD) [96], pulsed laser deposition (PLD) [97, 98], microwave plasma (MP) [99, 100], and molecular beam epitaxy (MBE) [101, 102]. A wide range of growth conditions were employed. The various growth techniques are quite different and the choise of the most suitable one is difficult and has to be based on the applications. In this work, for the formation of the nanostructures was chosen as growth technique the molecular beam epitaxy; more details about it can be found in chapter 2.

1.3.4.2 Vapor Liquid Solid mechanism

There are many methods of growing the nanowires including vapor liquid solid (VLS), solid liquid solid (SLS), vapor solid solid (VSS) and others. Among the vapor based techniques, the VLS is the most used one and seems to be the most successful for fabricating nanowires with crystalline structure and in large amounts. The name of the ***VLS*** mechanism comes from the fact that growth material from ***vapor*** passes through a ***liquid*** alloy droplet and ends up as ***solid***. In 1963, Wagner and Ellis [88] first proposed as growth mechanism for their whisker vapor liquid solid (VLS) mechanism. Their work was mainly focused on the growth of Si whiskers seeded by Au particles. The two elements (Si and Au) form a liquid alloy at low temperature (360°C) which is stable at growth temperature (800-1100°C) and these Au rich alloys act as preferential nucleation sites for the Si crystal formation. Close to these particles the amount of growth material in

the vapor state is increased compared to elsewhere in the substrate. The two main requirements for VLS are:

i) the presence of some metal impurity on the substrate is mandatory for nanowire growth;

ii) small droplets have to be located during the growth process at the tip of the nanowires.

Characteristic for VLS method is the fact that nanowire formation takes place only in the areas activated by the presence of the metal catalyst. The position and the diameter of the nanowires, and even their physical properties are well correlated with the Au rich droplet characteristics. Alloy droplets of nanometric size are required to be prepared on the substrates, and even so not all the sizes promote the nanowire synthesis [103]. Of course, this is well correlated with the used growth parameters, which will also play an important part in the growth process.

A sketch of the particle-assisted nanowire growth steps is illustrated in figure 1.14. The first requirement, as above mentioned, is the existence of a seed particle on the substrate from which a nanowire will grow. Usually a thin Au layer is deposited on the substrate by sputter deposition or thermal evaporation. Lithography techniques can also be used to controllably manipulate the diameter and position of the droplets. In the following, after reaching growth temperature, the growth material is introduced. A supersaturated state of growth material in Au has to be reached. The droplets of a liquid catalyst are formed on the substrate via eutectic reaction between the semiconductor and the metal, typically Au. These droplets present a sphere, half-sphere or truncated sphere shape. Atoms of the growth material precipitate out of the supersaturated liquid-alloy droplet at the liquid-alloy/solid interface, and the droplet rises from the surface. The supersaturation is required and is induced by the difference in the chemical potential of the components (chemical reactants). In a vacuum deposition system, crystalline nanowires are then grown by a liquid metal-alloy droplet catalyzed chemical or physical vapor deposition process. The Au rich droplets on the surface of the substrate lower the activation energy of normal vapor-solid growth. Nanowire length is controlled by the amount of material introduced (growth time and growth rate).

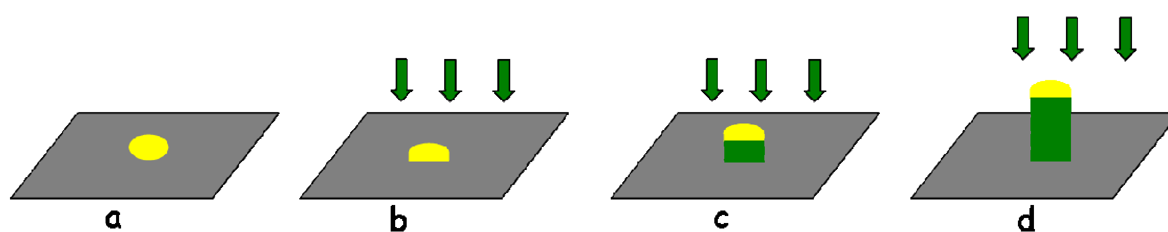

Figure 1.14. *Particle-assisted nanowire growth. a) Metal seed particles are formed and/or deposited on the substrate. b) The substrate is heated to desired growth temperature and the growth material introduced. An alloy starts forming with seed particles. c) Reaching supersaturation point of the growth material and nanowires stars to grow at the particle-crystal interface. d) Continuing the introduction of more material and the nanowires grow at the particle-wire interface.*

1.3.4.3 Gold as catalyst

For nanowire growth using VLS mechanism metal presence is required. In this work was chosen gold as seed material. The structures obtained by Wagner and Ellis [88] presented very often a small metal particle at one end and typically had a diameter that was correlated with that of the wire (or whisker) on which they were observed. Metal particle had usually a hemisphere or truncated sphere and with the flat ends in direct contact with the end of the wire. Since then, Au was employed to promote the growth of nanowires, being the most frequently used catalyst material. The choice of gold as seed particle material is one of convenience, being the catalyst material that best works even if the reasons are not completely understood. The answer to the question: "why Au is such a favourable catalyst?" will facilitate the further choice of use alternative catalyst materials. Beside Au, many materials (typically metals) were used to promote the growth of nanowires. Successful results were obtained on the synthesis of Si or Ge nanowires using as seed for example: Ga [104-106], In [107, 108], Ag [109], Al [110], Bi [111], Ni [112], Cu [112], Pt [112], Ti [113, 114], Fe [115, 116], and others. Metal particles which are used as catalysts have mainly three roles: i) to kinetically promote the growth, ii) to determine the diameter of the nanowires, and iii) to control the position.

Coming back to Au, it presents many ***advantages*** that speak in its favour and which make it suitable as catalyst. Alternatives to Au evaporation are the usage of

colloidal nanoparticles commercially available with diameter between 2 and 250 nm [117], aerosol phase or lithographically produced nanoparticles [118]. High stability of the Au is also another advantage, especially when is needed a certain time between Au deposition and growth steps. Au is known to be relatively inert and does not react with gas-phase carriers including nitrogen, hydrogen and oxygen or with the most common solvents [63]. Au is not a corrosive material, does not react with anything and it is stable in solutions. It forms also low temperature liquid alloys with many materials of interest. Au performs well as a seed particle even for materials with which it does not form liquid alloys, or even solid intermediate phases [63]. The security constrains in the usage of Au are low.

Au presents also ***disadvantages***, through, especially in the semiconductor area. Au presence is a problem because is easily incorporated within the Si and/or Ge nanowires. Gold diffusivity in silicon is quite high, being easily incorporated at low concentration within Si-based devices. It also forms deep-level traps within the Si band gap, destroying the electronic properties. Due to gold presence the resulting nanowires may not be suitable for electronic devices fabrication.

On choosing the proper seed material another important issue that has to be taken in the account is the eutectic temperature of the involved components. It has also to be correlated with the growth technique and the available facilities. In this work, the materials in use were: Au as seed material, Si (substrates material) and Si and Ge as growth materials, and the attention was focused on the ***Au:Si:Ge eutectic***. The melting temperature of the Au:Si alloy reaches a minimum (~ 363°C) when the ratio of its constituents is 4:1 Au:Si. When a liquid Au-Si alloy is slowly cold down, solid Au and Si will precipitate out of the eutectic point. For Au-Ge eutectic point is at almost the same temperature as for Si case, for a composition of the liquid alloy of 28 at. % Ge. Corresponding phase diagram of Au in Si [119] and Au in Ge [120] are shown in figure 1.15. It was reported [121] that at nanometric scale the eutectic point is even lower than the presented values in figure 1.15. Nanowire growth even below the eutectic point was reported in the literature [122]. A difference in Au composition of only 1% makes a lot of difference, by reducing the eutectic point by 40ºC (see figure 1.15b). Furthermore, nanowire growth depends on the growth pressure [120], an important factor especially for the growth techniques far from atmosphere pressure (e.g. MBE).

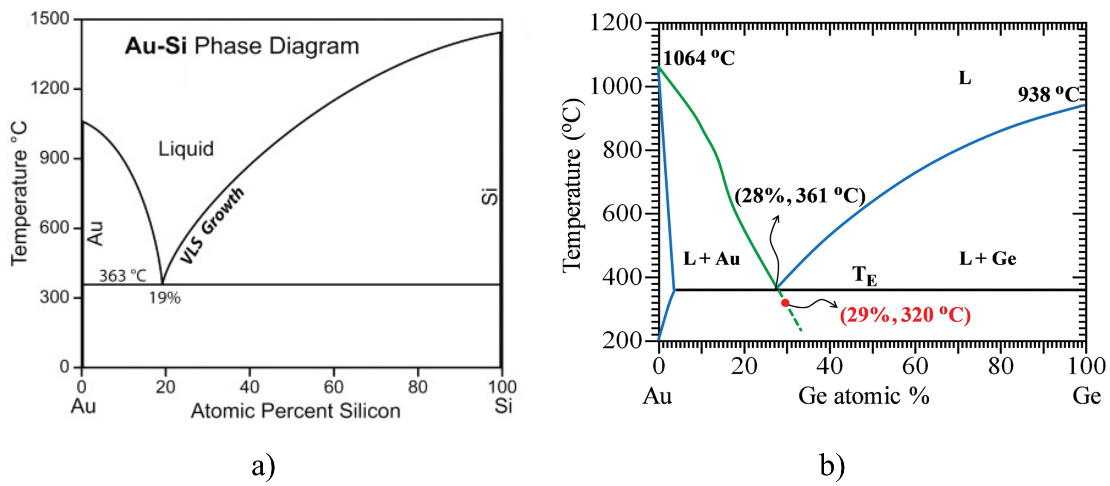

Figure 1.15. *Au-Si (a) and Au-Ge (b) binary alloy phase diagram. Figures extracted from reference 119 and 120.*

1.4 Bibliography

1. D. J. Paul, *Semicond. Sci. Technol*. **2004**, *19*, R75 - R108.

2. J. D. Cressler, *SiGe and Si Strained-Layer Epitaxy for Silicon Heterostructure Devices*, CRC Press Taylor & Francis Group 6000 Broken Sound Parkway NW, Suite 300 Boca Raton, FL 33487-2742, **2008**.

3. M. Glickman, *Physical Review* **1955**, *100*, 1146.

4. H. Kroemer, *Proceedings IRE* **1957**, *45*, 1535.

5. E. Kasper, J.-H. Herzog, H. Kibbel, *Applied Physics* **1975**, *8*, 199.

6. R. H. M. van de Leur, A. J. G. Schellingerhout, F. Tuinstra, J. E. Mooij, *J. Appl. Phys*. **1988**, *64 (6)*, 3043.

7. http://www.ioffe.rssi.ru/SVA/NSM/Semicond/SiGe/bandstr.html

8. C. Nordling and J. Österman, *Physics Handbook for Science and Engineering*, Studentlitteratur, Lund, 6th ed., **1999**.

9. J. P. Dismukes, L. Ekstrom, R. J. Paff, *J. Phys. Chem*. **1964**, *68*, 3021.

10. H.-J. Herzog, in: E. Kasper, and K. Lyutovich (Eds.), *Properties of Silicon Germanium and SiGe:Carbon*, INSPEC, London, p. 48, **2000**.

11. K. W. Böer, *Survey of Semiconductor Physics*, Vol. 1, John Wiley & Sons, Inc., New York, 2nd ed., **2002**.

12. F. Schäffler, in: E. Kasper, and K. Lyutovich, *Properties of Silicon Germanium and SiGe:Carbon*, INSPEC, London, p. 196, **2000**.

13. F. Schäffler, *Semi. Sci. Technol*. **1997**, *12*, 1515.

14. Photonics.com/ Photonics Spectra vol. 42 issue 1, 2008.

15. T. Steiner, *Semiconductor Nanostructures for Optoelectronic Applications*, Artech House, Inc. Boston - London, Inc. 685 Canton Street Norwood, MA 02062, **2004**.

16. F. C. Frank, J. H. Van der Merwe, *Proc. Roy. Soc. Lond. A* **1949**, *198*, 205.

17. I. N. Stranski, L. Krastanow, *Sitzungsber. Akad. Wiss. Wien, Math. – Naturwiss. K1. IIb* **1938**, *146*, 797.

18. M. Volmer, A. Z. Weber, *Phys. Chem*. **1926**, *119*, 277.

19. F. Boscherini, G. Capellini, L. Di Gaspare, F. Rosei, N. Motta, S. Mobilio, *App. Phys. Lett*. **2000**, *76*, 682.

20. A. Rockett, *The materials science of semiconductors*, Springer New York, USA, **2008**.

21. R. Lange, K. E. Junge, S. Zollner S. S. Iyer, A. P. Powell, K. Eberl, *J. Appl. Phys.* **1996**, *80*, 4578.

22. D. J. Dunstan, *J. Mater. Sci.: Mater. in Electron*. **1997**, *8*, 337.

23. P. M. Money, *Mater. Sci. Engineering*, **1996**, *R17*, 105.

24. J. W. Matthews, A. E. Blakeslee, *J. Cryst. Growth* **1976**, *32*, 265.

25. E. Bauer, *Z. Kristallogr*. **1958**, *110*, 372.

26. B. Sanduijav, D. G. Matei, G. Springholz, *Nanoscale Res. Lett*. **2010**, *5*, 1935.

27. H. - J. Gossmann, L. C. Feldman, W. M. Gibson, *Surf. Sci.* **1985**, *155*, 413.

28. M. Asai, H. Ueba, C. Tatsuyama, *J. Appl. Phys.* **1985**, *58(7)*, 2577.

29. Y. Kataoka, H. Ueba, C. Tatsuyama, *J. Appl. Phys.* **1988**, *63(3)*, 749.

30. V. Le Thanh, P. Boucaud, Y. Zheng, A. Younsi, D. DeHbarre, D. Bouchier, J.-M. Lourtioz, *J. Crystal Growth* **1999**, *201-202*, 1212.

31. J. Venables, *Introduction to Surface and Thin Film Processes*. Cambridge: Cambridge University Press **2000**.

32. B. Voigtlander, *Surface Science Reports* **2001**, *43*, 127.

33. M. Goryll, L. Vescan, H. Lueth, *Thin Solid Films* **1998**, *336*, 244.

34. V. Cimalla, K. Zekentes, *App. Phys. Lett*. **2000**, *77(10)*, 1452.

35. A. Bernardi, M. I. Alonso, A. R. Goñi, J. O. Osso, M. Garriga, *Surface Science* **2007**, *601*, 2783.

36. A. Bernardi, M. I. Alonso, J. S. Reparaz, A. R. Goñi, P. D. Lacharmoise, J. O. Osso, M Garriga, *Nanotechnology* **2007**, *18*, 475401.

37. J. A. Floro, E. Chason, L. B. Freund, R. D. Twesten, R. Q. Hwang, G. A. Lucadamo, *Phys. Rev. B* **1999**, *59*, 1990.

38. M. I. Alonso, M. de la Calle, J. O. Ossó, M. Garriga, A. R. Goñi, *J. App. Phys*. **2005**, *98*, 033530.

39. F. K. LeGoues, M. Hammar, M. C. Reuter, R. M. Tromp, *Surface Science* **1996**, *349*, 249.

40. J. Tersoff, R. M. Tromp, *Phys. Rev. Letter.* **1993**, *70*, 2782.

41. B. J. Spencer, J. Tersoff, *Phys. Rev. Letter.* **1998**, *79*, 4858.

42. F. Liu, *Phys. Rev. Letter*. **2002**, *89*, 246105-1.

43. O. E. Shklyaev, M. J. Beck, M. Asta, M. J. Miksis, P. W. Voorhees, *Phys. Rev. Letter*. **2005**, *94*, 176102.

44. A. Ronda, I. Berbezier, *Physica E* **2004**, *23*, 370.
45. J. Stangl, V. Holý, G. Bauer, *Reviews of Modern Physics* **2004**, *76*, 725.
46. T. I. Kamins, R. S. Williams, *Appl. Phys. Lett*. **1997**, *71*, 1201.
47. T. Schwarz-Selinger, Y. L. Foo, D. G. Cahill, J. E. Greene, *Phys. Rev. B* **2002**, *65*, 125317.
48. J. J. Zhang, M. Stoffel, A. Rastelli, O. G. Schmidt, V. Jovanovic, L. K. Nanver, *Appl. Phys. Lett.* **2007**, *91*, 173115.
49. Z. Zhong, A. Halilovic, M. Muehlberger, F. Schaffler, G. Bauer, *J. Appl. Phys*. **2003**, *93*, 6258.
50. D. G. Matei, B. Sanduijav, G. Chen, G. Hesser, G. Springholz, *J. Crys. Growth* **2009**, *311*, 2220.
51. Z. Zhong, P. Chen, Z. Jiang, G. Bauer, *Appl. Phys. Lett*. **2008**, *93*, 043106.
52. G. Chen, G. Vastola, H. Lichtenberger, D. Pachinger, G. Bauer, W. Jantsch, F. Schaffler, L. Miglio, *Appl. Phys. Lett*. **2008**, *92*, 113106.
53. I. Berbezier, R. Ronda, *Surface Science Reports* **2009**, *64*, 47.
54. J. L. Gray, R. Hull, J. A. Floro, *J. Appl. Phys*. **2006**, *100*, 084312.
55. A. Karmous, I. Berbezier, A. Ronda, R. Hull, J. Graham, *Surf. Sci*. **2007**, *601*, 2769.
56. C. Dais, H. H. Solak, Z. Ekinci, D. Grutzmacher, *J. Appl. Phys. Lett*. **1998**, *92*, 143102.
57. T. Stoica, V. Shushunova, C. Dais, H. Solak, D. Gruetzmacher, *Nanotechnology* **2007**, *18*, 455307.
58. D. Kitayama, T. Yoichi, Y. Suda, *Thin Solid Films* **2006**, *508*, 203.
59. A. Portavoce, M. Kammler, R. Hull, M. C. Reuter, F. M. Ross, *Nanotechnology* **2006**, *17*, 4451.
60. M. Kammler, R. Hull, M. C. Reuter, F. M. Ross, *J. Appl. Phys.* **2003**, *82*, 1093.
61. A. Pascale, I. Berbezier, A. Ronda, P. C. Kelires, *Phys. Rev. B* **2008**, *77*, 075311.
62. F. Hackl, M. Grydlik, M. Brehm, H. Groiss, F. Schaffler, T. Fromherz, G. Bauer, *Nanotechnology* **2011**, *22*, 165302.
63. K. A. Dick, *Progress in Crystal Growth and Characterization of Materials* **2008**, *54*, 138.
64. B. Yu, X. H. Sun, G. A. Calebotta, G. R. Dholakia, M. Meyyappan, *J. Cluster Science* **2006**, *17(4)*, 579.
65. H.-P. Liang, Y.-G. Guo, J.-S. Hu, C.-F. Zhu, L.-J. Wan, C.-L. Bai, *Inorg. Chem*. **2005**, *44*, 3013.

66. S. Xiong, R. Molecke, M. Bosch, P. R. Schunk, C. J. Brinker, *J. Am. Chem. Soc.* **2011**, *133*, 11410.
67. P. Werner, N. D. Zacharov, G. Gerth, L. Schubert, U. Gösele, *Int. J. Mat. Res*. **2006**, *97(7)*, 1008.
68. A. Kramer, M. Albrecht, T. Boeck, T. Remmele, P. Schramm, R. Fornari, *Superlattices and Microstructures* 2009, 46, 277.
69. S.-G. Ihn, J.-I. Song, *Nanotechnology* **2007**, *18*, 355603.
70. G. E. Cirlin, V. G. Dubrovskii, I. P. Soshnikov, N. V. Sibirev, Y. B. Samsonenko, A. D. Bouravleuv, J. C. Harmand, F. Glas, *Phys. Status Solidi RRL* **2009**, *3*, 112.
71. I. Miccoli, P. Prete, F. Marzo, D. Cannoletta, N. Lovergine, *Cryst. Res. Technol.* **2011**, *46(8)*, 795.
72. F. M. Ross, *Rep. Prog. Phys*. **2010**, *73*, 114501.
73. T. Kita, S. Nishimoto, Y. Kameshima, M. Miyake, *J. Am. Ceram. Soc*. **2010**, *93(9)*, 2427.
74. G. Wang, H. Wang, Y. Ling, Y. Tang, X. Yang, R. C. Fitzmorris, C. Wang, J. Z. Zhang, Y. Li, *Nano Lett*. **2011**, *11*, 3026.
75. M.-P. Chien, N. C. Gianneschi, *Small* **2011**, *7(14)*, 2041.
76. J. Xiang, W. Lu, Y. Hu, Y. Wu, H. Yan, C. M. Liebre, *Nature* **2006**, *441*, 489.
77. L. Cao, J. S. White, J.-S. Park, J. A. Schuller, B. M. Clemens, M. L. Brongersma, *Nature Materials* **2009**, *8*, 643.
78. B. Tian, X. Zheng, T. J. Kempa, Y. Fang, N. Yu, G. Yu, J. Huang, C. M. Liebre, *Nature* **2007**, *449*, 885.
79. M. D. Kelzenberg, D. B. Turner-Evans, B. M. Kayes, M. A. Filler, M. C. Putnam, N. S. Lewis, H. A. Atwater, *Nano Lett*. **2008**, *8*, 710.
80. E. C. Garnett, P. Yang, *J. Am. Chem. Soc*. **2008**, *130*, 9224.
81. Y. Ahn, J. Dunning, J. Park, *Nano Lett*. **2005**, *5*, 1367.
82. Y. Gu, E.-S. Kwak, J. L. Lensch, J. E. Allen, T. W. Odom, L. J. Lauhon, *Appl. Phys. Lett*. **2005**, *87*, 043111.
83. O. Hayden, R. Agarwal, C. M. Lieber, *Nature Mater*. **2006**, *5*, 352.
84. B. Polyakov, B. Daly, J. Prikulis, V. Lisauskas, B. Vengalis, M. A. Morris, J. D. Holmes, D. Erts, *Adv. Mater*. **2006**, *18*, 1812.
85. A. B. Greytak, C. J. Barrelet, Y. Li, C. M. Lieber, *Appl. Phys. Lett*. **2005**, *87*, 151103.
86. M. Huang, S. Mao, H. Feick, H. Yan, Y. Wu, H. Kind, E. Weber, R. Russo, P. Yang, *Science* **2001**, *292*, 1897.

87. R. G. Treuting, S. M. Arnold, *Acta Met*. **1957**, *5*, 598.

88. R. S. Wagner and W. C. Ellis, *Appl. Phys. Lett*. **1964**, *4*, 89.

89. M. S. Gudiksen, L. J. Lauhon, J. Wang, D. C. Smith, C. M. Liebre, *Nature* **2002**, *415*, 617.

90. N. D. Zakharov, P. Werner, G. Gerth, L. Schubert, L. Sokolov, U. Gösele, *J. Cryst. Growth* **2006**, *290*, 6.

91. C.-Y. Wen, M. C. Reuter, J. Bruley, J. Tersoff, S. Kodambaka, E. A. Stach, F. M. Ross, *Science* **2009**, *326*, 1247.

92. R. Adelung, O. C. Aktas, J. Franc, A. Biswas, R. Kunz, M. Elbahri, J. Kanzow, U. Schurmann, F. Faupel, *Nature Materials* **2004**, *3*, 375.

93. A. Gustafsson, F. Reinhardt, G. Biasiol, E. Kapon, *Appl. Phys. Lett*. **1995**, *67(25)*, 3673.

94. H. Jagannathan, M. Deal, Y. Nishi, J. Woodruff, C. Chidsey, P. C. McIntyre, *J. Appl. Phys*. **2006**, *100*, 024318.

95. Y. Sierra-Sastre, S. A. Dayeh, S. T. Picraux, C. A. Batt, *ACSNano* **2010**, *4(2)*, 1209.

96. M. Longo, C. Wiemer, O. Salicio, M. Fanciulli, L. Lazzarini, E. Rotunno, *J. Crystal Growth* **2011**, *315*, 152.

97. M. S. Gudiksen, L. J. Lauhon, J. Wang, D. C. Smith, C. M. Lieber, *Nature* **2002**, *415*, 617.

98. Y. Xia, P. Yang, Y. Sun, Y. Wu, B. Mayers, B. Gates, Y. Yin, F. Kim, H. Yan, *Adv. Mater.* **2003**, *15*, 353.

99. V. Kumar, J. H. Kim, C. Pendyala, B. Chernomordik, M. K. Sunkara, *J. Phys. Chem. C* **2008**, *112,* 17750.

100. F. Zhu, Z. X. Yang, W. M. Zhou, Y. F. Zhang, *Solid State Communications* **2006**, *137*, 177.

101. L. Schubert, P. Werner, N. D. Zakharov, G. Gerth, F. M. Kolb, L. Long, U. Gösele, T. Y. Tan, *Appl. Phys. Lett.* **2004**, *84*, 4968.

102. A. Wolfsteller, N. Geyer, T.-K. Nguyen-Duc, P. Das Kanungo, N. D. Zakharov, M. Reiche, W. Erfurth, H. Blumtritt, S. Kalem, P. Werner, U. Gösele, *Thin Solid Films* **2010**, *518*, 2555.

103. P. Werner, N. D. Zakharov, G. Gerth, L. Schubert, U. Gösele, *Int. J. Mat. Res.* **2006**, *97*, 1008.

104. I. Zardo, L. Yu, S. Conesa-Boj, S. Estrade, P. J. Alet, J. Rossler, M. Frimmer, P. Roca i Cabarrocas, F. Peiro, J. Arbiol, J. R. Morante, A. Fontcuberta i Morral, *Nanotechnology* **2009**, *20*, 155602.

105. P. Meduri, G. U. Sumanasekera, Z. Chen, M. K. Sunkara, J. *Nanoscience and Nanotechnology* **2008**, *8*, 3153.

106. J. Bae, N. N. Kulkarni, J. P. Zhou, J. G. Ekerdt, C.-K. Shih, *J. Crystal Growth* **2008**, *310*, 4407.

107. P. Nguyen, H. T. Ng, M. Meyyappan, *Adv. Mater*. **2005**, *17*, 549.

108. A. Kramer, T. Boeck, P. Schramm, R. Fornari, *Physica E* **2008**, *40*, 2462.

109. C.-Y. Hong, S.-F. Tsai, H.-C. Chang, W.-T. Lin, K.-H. Wu, *J. Nanoscience and Nanotechnology* **2010**, *10(7)*, 4773.

110. Y. Wang, V. Schmidt, S. Senz, U. Gosele, *Nature Nanotechnology* **2006**, *1*, 186.

111. C. Yan, P. S. Lee, *J. Phys. Chem. C* **2009**, *113(6)*, 2208.

112. W. Molnar, A. Lugstein, P. Pongratz, N. Auner, C. Bauch, E. Bertagnolli, *Nano Lett.* **2010,** *10*, 3957.

113. Q. Tang, X. Liu, T. I. Kamins, G. S. Solomon, J. S. Harris, *J. Cryst. Growth* **2003**, *251*, 662.

114. T. I. Kamins, R. S. Williams, D. P. Basile, T. Hesjedal, J. S. Harris, *J. Appl. Phys*. **2001**, *89*, 1008.

115. X. J. Wang, B. Dong, Z. Zhou, *Materials Letters* **2009**, *63*, 1149.

116. I. Ahmad, M. Fay, Y. Xia, X. Hou, A. Kennedy, Y. Zhu, *J. Phys. Chem. C* **2009**, *113,* 1286.

117. M. H. Magnusson, K. Deppert, J.-O. Malm, J.-O. Bovin, L. Samuelson, *Nano Structured Materials* **1999**, *12*, 45.

118. T. Mårtensson, M. Borgstrom, W. Seifert, B. J. Ohlsson, L. Samuelson, *Nanotechnology* **2003**, *14*, 1255.

119. V. Schmidt, J. V. Wittemann, S. Senz, U. Gösele, *Adv. Mater*. **2009**, *21*, 2681.

120. S. Kodambaka, J. Tersoff, M. C. Reuter, F. M. Ross, *Science* **2007**, *316*, 729.

121. K. Dick, T. Dhanasekaran, Z. Zhang, D. Meisel, *J. Am. Chem. Soc*. **2002**, *124*, 2312.

122. H. Adhikari, A. F. Marshall, I. A. Goldthorpe, C. E. D. Chidsey, P. C. McIntyre, *Acs. Nano* **2007**, *1(5)*, 415.

Chapter 2

Experimental techniques

2.1 Patterning and growth methods

2.1.1 Focused Ion Beam

2.1.1.1 Generalities

Since the focused ion beam (FIB) technology was introduced into the semiconductor industry in the early 1980s, it has become a routine analytical tool for IC device analysis, circuit repair and advanced specimen preparation [1, 2].

Various FIB processes have been developed for either *removing* material (direct ion milling, FIB chemical etching) or *depositing* material on a surface (ion implantation, direct ion deposition, FIB chemical deposition, FIB induced nucleation) [3]. Another important FIB application is for *direct lithography patterning* [4]. In addition to milling, sample preparation for transmission electron microscopy (TEM) by FIB has been widely studied and used [5]. The focused ion beam technology is one of the most promising techniques for nanofabrication, because is a mask-less process and provides a great flexibility and simplicity [2]. However, conventional FIB lithography has its own set of problems such as slow writing speed, limited penetration depth of heavier ions and substrate induced damage during exposure with lighter ions [4]. The modern focused ion beam system utilizes a liquid metal ion source (LMIS) at the top of its column to produce ions (usually Ga^+). From there the ions are pulled out and focused into a beam by an

electric field and subsequently passed through apertures, then scanned over the sample surface (figure 2.1).

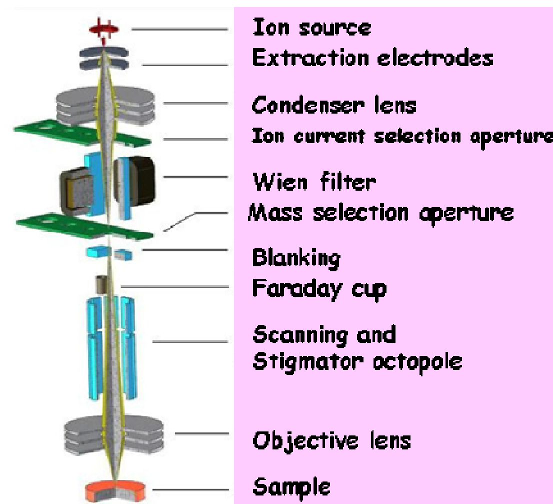

Figure 2.1. *Scheme of the ion column from Orsay Physics.*

Upon impact, the ion-atom collision is either elastic or inelastic in nature. Elastic collisions result in the excavation of the surface atoms - a term called sputtering - and they are the primary cause of the actual modification of the material surface (figure 2.2). Inelastic collisions occur when the ions transfer some of their energy to either the surface atoms or electrons.

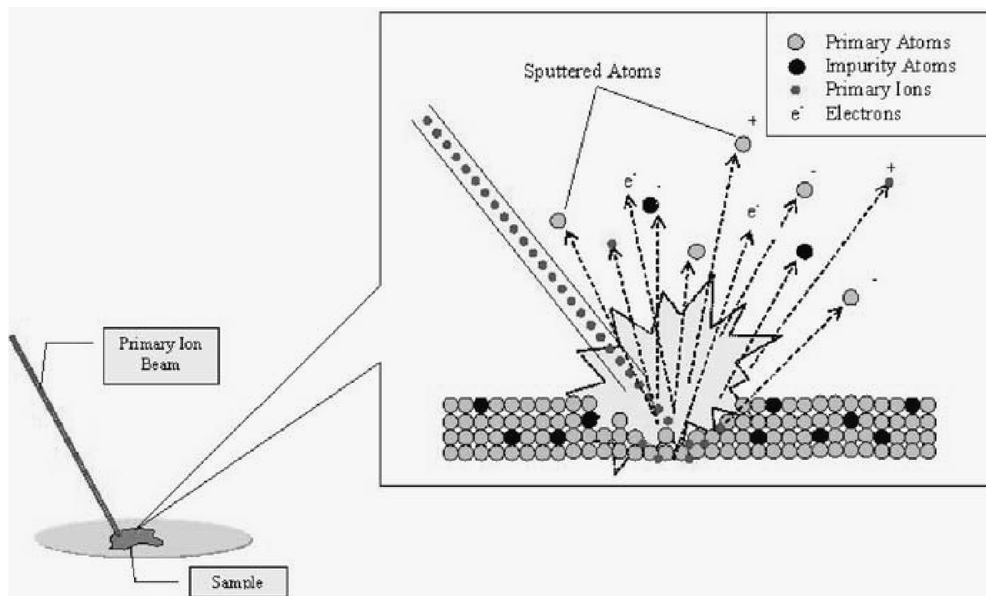

Figure 2.2. *Schematic diagram of the ion beam sputtering process. Figure extracted from reference [6].*

By combining imaging and sample interaction abilities of FIB with the high resolution, non-destructive imaging of SEM new breakthroughs in microscopy research can be achieved. The two-beam system accomplishes just that; by joining focused ion beam and scanning electron microscopy technology in a single machine, the two work symbiotically, achieving tasks beyond the limitations of either individual system. In a two-beam system, the ion beam and the electron beam are placed in fixed positions, with the former coming in at an angle (figure 2.3). The two beams are co-focused at what is called the "coincidence point," typically with a 5 mm working distance. This point is an optimized position for most of the operations taking place within the machine. For a best performance, the ion beam is tilted 45º-52º from the electron beam, allowing SEM imaging and FIB sample modification without having to move the sample. The stage can be controlled and tilted, allowing changes in the sample-beam orientation. In addition to the combined imaging benefits, the two-beam system allows for precise monitoring of FIB operation through the SEM, avoiding the substrate contamination while FIB imaging. In this way, the samples can be imaged in real time with the SEM while the FIB is being used, giving the operator complete control over the milling process. The application of FIB machine related to the surface modification involves its lithographic capabilities in

nanofabrication. It holds clear advantages over other methods in its ability for high resolution patterning and depth of focus.

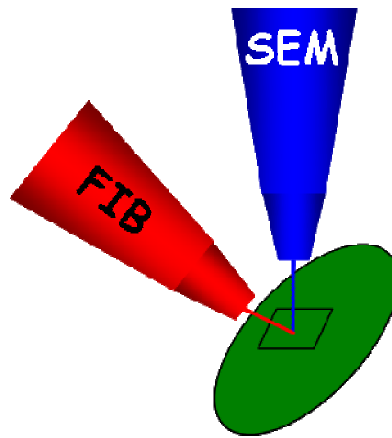

Figure 2.3. *Schematic representation of sample inside the FIB chamber. FIB and SEM are co-focused on the sample.*

2.1.1.2 Focused ion beam equipment description

The ion beam modifications of the Si substrates described in this work were carried out using a commercial FIB Tescan Lyra system with an incorporated SEM. The mass-filtered ultra-high resolution COBRA-FIB from Orsay Physics has an ultimate resolution of 2.5 nm (using Ga^+ ions). This Tescan LYRA1 XMH dual-beam equipment uses a liquid metal alloy ion source (LMAIS), the Wien filter allowing desired ion selection, and the energy can be varied between 5 and 30 KeV. For this work the LMAIS used is an eutectic AuSi alloy heated at 380°C. The patterns were performed with Au^{2+} ions selected with the mass filter (3.27 x 10^{-25} kg) using a mass selection aperture of 20 μm. Under these conditions, the FIB resolution reaches ~15 nm. The minimum lateral dimension of the patterns obtained with this equipment is a diameter around 50 nm as a result of beam size and large Au^{2+} ions (about 1.2 Å). Two procedures were available in order to pattern the substrates: ultra fast grabbing process and milling 2D arrays with different shapes (e.g. circle, rectangle, star, line, etc). A good control of the FIB parameters (e.g. dwell time, probe current, apertures, spot size, overlap, speed, and time/feature) allows for achieving the desired patterning conditions. The dwell time was

increased from the lowest value available (0.8 μs) to 500 μs, while the probe current was varied between 1 and 100 pA. The apertures available within this FIB equipment were between 10 and 50 μm, enabling tailoring ion beam size and implicitly the object sizes. The values of the employed ion doses were also varied in a wide range ($1x10^{-4}$ - $300x10^{-4}$ C/cm^2) as a result of the different combinations of the FIB patterning parameters. Inside the FIB chamber under vacuum ambient the sample is mounted on a holder which can be tilted at different angles. For most samples the holder was tilted at 55º from z axis (SEM) and 90º to FIB (normal incidence). Other configurations, by slightly changing the tilt angle (±2-10º) were employed in order to increase FIB features accuracy and to reduce the material redeposition. The number of the patterned objects can be increased from 1 to a desired value not exceeding the largest available area of 400/400 μm^2 (depending on the objects size and distance between them). FIB equipment allows excellent pattern reproducibility at this large scale. More details about the evolution of patterned features performed on Si substrates with the modification of the FIB parameters can be found in chapter 4.

Some of the notions that will be used later on, were calculated using the following definitions [7]. *Flux* is defined as the time rate of flow of energy; the radiant or luminous power in a beam. In the case of an ion beam flux it is measured as the number of particles flowing through a given area per unit time and has units of $ions/cm^2/s$. The flux is a rate and remains constant for a given set of parameters such as beam current/aperture setting. *Dose* is a general term denoting the quantity of radiation, energy, or particles absorbed by a medium. In the case of an ion beam, dose has units of $ions/cm^2$. Similar to flux, the *beam current* is also a measure of the time rate flow of energy or how many ions are delivered per unit time. The beam current is measured in amperes, which is equivalent to units of charge per unit time or Coulombs(C)/sec.

2.1.2 Molecular Beam Epitaxy

2.1.2.1 Molecular Beam Epitaxy overview

Since 1971 when Cho [8] proposed it, molecular beam epitaxy (MBE) was developed as a means of growing high-purity epitaxial layers. Originally MBE was designed for epitaxial layer by layer deposition only. With MBE high-quality layers with very abrupt interfaces and good control of their thickness, doping, and composition [9] can be manufactured. Beside layers, islands and nanowires were successfully grown by MBE. Nowadays, MBE evolved to a versatile growth technique, being used for the epitaxial growth of semiconductors, metals, superconductors or isolators [9]. This technique is conceptually simple and potentially more controllable than other techniques (e.g. vapor phase epitaxy), making from MBE a research tool used for understanding fundamental processes in crystal growth.

Solid-source molecular beam epitaxy (SS-MBE), one of MBE variations, is a deposition process whose rate is well controlled by the molecular flux from the sources. For SS-MBE, the process starts with physical evaporation of the constituent elements from solid-phase sources at high local temperatures. Resulting thermal-energy molecular or atomic beams subsequently travel through the ultra-high vacuum (UHV) chamber towards the substrate without involving any chemical change. In the particular case, Si and Ge are heated to desired temperature and after reaching the temperature the shutters are opened and they evaporate (figure 2.4). The Si and Ge beams hit the substrate and the atoms diffuse over the surface and bond at surface lattice sites. In the case of semiconductors normally the substrate is heated at some hundred of degree centigrades, because otherwise at low temperature an amorphous layer is formed due to the reduced atoms mobility. Under appropriate conditions, the beam of atoms and molecules will attach to the substrate material and an epitaxial layer will begin to form.

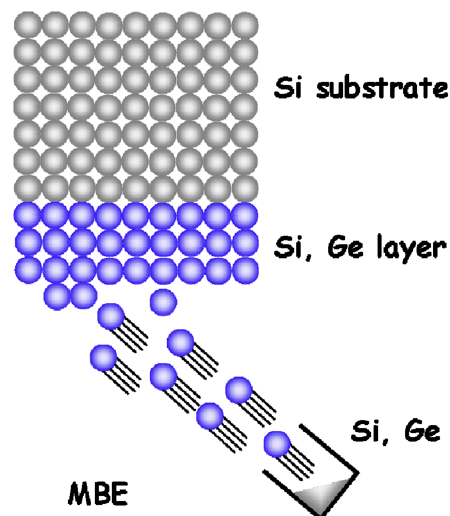

Figure 2.4. *Principle of deposition method used in semiconductor epitaxy. In MBE, atomic beams of the film material hit the substrate surface.*

A part of the fundamental atomic processes that take place during MBE epitaxial growth [9, 10] are schematically shown in figure 2.5.

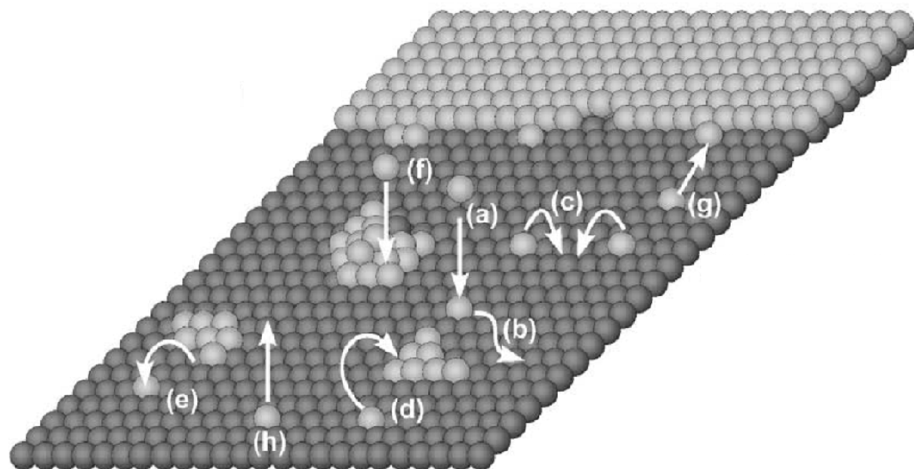

Figure 2.5. *Schematic illustration of fundamental processes on growing surface during MBE epitaxy: a) deposition on the terrace, b) diffusion on the terrace, c) island nucleation, d) attachments of atoms at islands, e) detachments of atoms from islands, f) deposition on an island, g) attachment at a step, h) desorption from the terrace. Figure extracted from reference [10].*

As mentioned, MBE works in UHV environment, making it possible the use of electrons and ions to observe the surface and the film quality during the growth. The most commonly used monitorization technique within MBE systems is the reflection high-energy electron diffraction (RHEED). The RHEED system normally consists of an electron gun which produces a high energy beam with very large incidence angles (grazing incidence) to the substrate surface. The phosphor screen situated on the opposite side displays the reflected electron diffraction pattern. With the help of this diffraction patterns surface geometry and morphology can be determined. Growth rate can be examined *in situ* with the RHEED.

Because of the high degree of control possible with MBE, it is a valuable tool in the development of sophisticated electronic and optoelectronic devices. However, MBE is considered an expensive technique, limiting its use for commercial applications, being restricted to the laboratory to study the high quality films growth conditions.

2.1.2.2 Molecular Beam Epitaxy equipment description

In this work, all the samples were grown by using a solid-source molecular beam epitaxy (SS-MBE) Omicron system, which has been widely used in research laboratories for fundamental material studies due to its special features. The equipment consists of an entry chamber and a growth chamber, with a gate valve situated in between them. The chambers are supported by a pumping system involving an ionic, a turbo-molecular pump and a mechanical rotary vane pump, together with a Ti sublimation pump. After proper baking and source out gassing, a base pressure in the growth chamber is maintained at a level of 10^{-10} mbar, which is normally increased during the growth process (10^{-8} - 10^{-9} mbar). Loading and unloading of the samples into and out of the growth chamber is done in the "Fast Entry Lock" (FEL) chamber. Storage of the wafers is also done in the same entry chamber. The pressure inside this chamber is in the order of 10^{-8} mbar. For contamination reduction the base pressure of MBE equipment is kept at ultra high vacuum level. Equipment refrigeration system is ensured through a water circuit.

In the main growth chamber, there is an electron-gun (e-gun) evaporator for Si and high temperature effusion cell for Ge to supply the constituent elements. P-type doping is provided by a high-temperature boron (B) effusion cell, and n-type doping can be implemented by an antimony (Sb) low temperature effusion cell. The machine is

equipped also with a carbon sublimation source with a pyrolytic graphite filament, and a GaP decomposition cell for phosphorus (P_2). Reflection high-energy electron diffraction (RHEED) (20-30kV) setup is installed for in-situ surface analysis during the growth, and a cross-beam quadrupole mass-spectrometer is used both for residual gas analysis and for flux monitoring. The scheme of the MBE equipment is illustrated in figure 2.6.

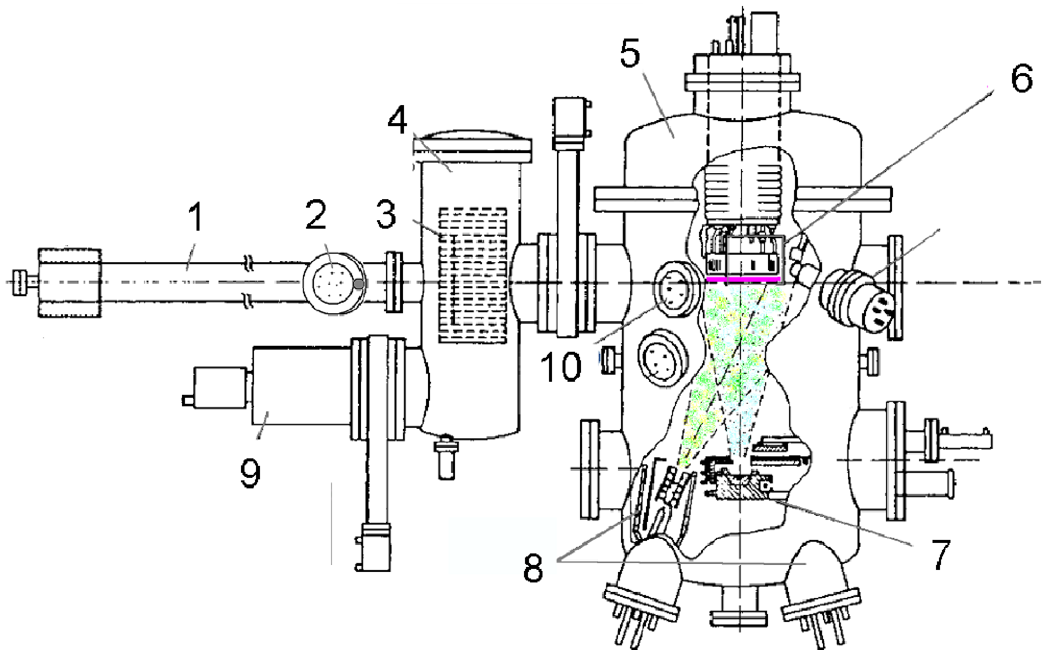

Figure 2.6. *Schematic view of a MBE system: 1. samples transfer bar, 2. window, 3. wafers store holder, 4. FEL chamber, 5. MBE growth chamber, 6. substrate, 7. Si e-gun evaporator, 8. effusion cells for Ge, B, Sb, P_2 and C sublimation source, 9. ion pump, 10. RHEED.*

Heterostructure growth is possible by easily switching (computer controlled) from one source to another. The MBE offers a good control of the growth parameters (vacuum, clean substrate, growth rate, temperature, time) and an oxygen free surface. The MBE deposition can be achieved on 10 cm wafers, but also on samples with a smaller size (1x1, 1.5x1.5 or 2x2 cm^2) by using a special sample holder. The substrates are orientated face down inside the MBE main chamber during the growth process. The continuous rotation of the samples is available (if desired), to promote uniform crystal growth on its surface.

All the thermal treatments of the SiGe alloy samples were performed inside the MBE main chamber in order to avoid the oxidation process. More details about the

specific MBE parameters employed for the growth of each series of samples, and the annealing conditions can be found in the experimental sections (chapter 3 and 4).

2.2 Optical characterization techniques

2.2.1 Raman spectroscopy

The phenomenon of inelastic scattering of light was first postulated by Smekal in 1923 [11] and first observed experimentally in 1928 by Raman and Krishnan [12]. Since then, the phenomenon has been referred to as Raman spectroscopy. Raman scattering leads to the creation or annihilation of elementary excitations in the probed medium. These excitations can be phonons as well as plasmons or other excitations. Creation processes are termed Stokes-scattering, annihilation processes anti-Stokes scattering. Depending on the number of elementary excitations involved, the scattering process is referred to as being of first, second or higher orders [13].

Raman spectroscopy is a spectroscopic technique used to study vibrational, rotational, and other low-frequency modes in a system. It relies on inelastic scattering of monochromatic light, usually from a laser in the visible, near infrared, or near ultraviolet range. The laser light interacts with phonons or other excitations in the system, resulting in the energy of the laser photons being shifted up or down. The shift in energy gives information about the phonon modes in the system [14]. The technique can be applied to all kind of materials in liquid, solid or gaseous phase, offering information about symmetry and crystalline structure, chemical composition, mechanical tensions, sample temperature and so on. Samples measured with this technique do not need any preliminary preparation or any kind of treatments.

Raman spectra were recorded using a Jobin Yvon LabRam HR800 system in a backscattering configuration. In order to minimize the contribution of the Si 2TA arising from the substrate (whose energy is close to that of the Ge-Ge mode) we have used the crossed polarization configuration $z(x,y)\bar{z}$, in which the 2TA mode is Raman forbidden. The samples were excited with the green line (514.5 nm) of an air-cooled argon ion laser, and the spot size of the light focused onto the samples was around 1 μm. The detection of Raman signal was carried out with a Charge Coupled Device (CCD) camera. Since for this setup a confocal microscope is available, micro-Raman experiments were performed.

2.2.2 X-ray Diffraction

X-ray diffraction (XRD) is a powerful and non-destructive material characterization technique, which was used throughout this thesis work for studying various structural properties of SiGe/Si heterostructures, Ge composition, and strain condition. The basic diffraction condition of XRD can be mathematically described by Bragg's law:

$$n\lambda = 2d\sin\theta \qquad 2.1$$

where d is the distance between adjacent diffraction lattice planes that scatter the incident x-rays, λ is the wavelength of the x-ray radiation, θ is half of the angle between the incident and diffracted x-ray beams, and n is an integer representing the order of diffraction [15]. Models for the relation between lattice constant and e.g. germanium-content (x) allow for the determination of x in $Si_{1-x}Ge_x$ layers.

In this work, XRD measurements data for the symmetric reflections were collected using a Siemens D-5000 diffractometer with an incident angle of roughly 68.3º. The x-ray maps of the reciprocal space (q-plots) using two asymmetric reflections (224) and $(\bar{2}\bar{2}4)$ for as grown samples, were recorded using a Bruker D8 with GADDS detector. Asymmetric reflections allow for measuring the lattice parameter in both directions perpendicular and parallel to the surface.

2.2.3 Spectroscopic ellipsometry

The ellipsometry is an optical technique devoted to the analysis of surfaces. It is based on the measurement of the variation of the polarization state of the light after reflection on a surface. The ellipsometry technique has been discovered one hundred years ago but it is only since the early 80's, thanks to the development of electronic and computers that the technique expands largely in numerous fields. Spectroscopic ellipsometry can analyze complex structures such as multilayers, surface and interface roughness, inhomogeneous layers, anisotropic layers and much more. This technique investigates the complex refractive index or dielectric function tensor, which gives access to fundamental physical parameters and is related to a variety of sample properties,

including morphology, anisotropy, crystal quality, chemical composition, effect of confinement, or electrical conductivity [16]. Ellipsometry measures the change of polarization upon reflection or transmission. Typically, ellipsometry is done only in the reflection setup. The exact nature of the polarization change is determined by the sample's properties (thickness, complex refractive index or dielectric function tensor).

Ellipsometry measurements were performed at room temperature using as basic optical setup a rotating polarizer SOPRA ES4G spectral ellipsometer. The light source was a 75W high-pressure Xe arc lamp, and the reflected light was collected by an optical fiber and coupled to double prism/grating monochromator of 750 mm equivalent focal length. As detector we used a multialkali photomultiplier tube sensitive in the range from 1.4 to 5.2 eV.

2.3 Imaging techniques

2.3.1 Atomic Force Microscopy

Atomic force microscopy (AFM) is a widely used technique for studies of topography and other properties of different material surfaces (metals, semiconductors, rigid materials, and biological) [5]. AFM is high-resolution type of scanning probe microscopy, with resolution on the order of fractions of a nanometer. This technique allows for the investigation of the surface, offering a 3D view of the samples. One of the AFM advantages against SEM is the fact that there is no need for vacuum environment.

In AFM, mechanical force interactions acting between a sharp probe and a sample are used for surface imaging. The probe represents a micro machined cantilever with a sharp tip at one end. The tip-sample force causes a static deflection of the cantilever or changes in its dynamic properties. The so-called beam-defection method is a common way to measure the small bending of the cantilever [17], where a laser beam is reflected from the back side of the cantilever, and the beam deflection is monitored by a position-sensitive photodiode. The precise movement of the sample (or the tip) is controlled typically by a piezoelectric scanner. These measurements can be performed on scales from hundreds of microns down to nanometers.

AFM measurements can be operated in three modes: contact mode, non-contact mode, and tapping mode. In the non contact mode, the tip of the cantilever does not contact the sample surface and is held at a small and constant distance from the sample surface. Silicon tips size is in the order of some nanometers (~ 20 nm in our case). The surface topography is obtained by detecting the attractive van der Waals force between the tip and the surface. Non-contact mode AFM does not suffer from tip or sample degradation effects that are sometimes observed after taking numerous scans with contact AFM.

No special treatments were applied to samples before performing the measurements, except HF bath to remove the silicon oxide (where this is indicated). All the topographical images were recorded in non-contact mode, at room temperature using a XE-100 Parker system.

2.3.2 Scanning Electron Microscopy

A scanning electron microscope (SEM) is a type of electron microscope that images a sample by scanning it with a high-energy beam of electrons in a raster scan pattern. The electrons interact with the atoms that make up the sample producing signals that contain information about the samples surface topography, composition, and other properties such as electrical conductivity [5, 14]. The types of signals produced by an SEM include secondary electrons, back- scattered electrons (BSE), characteristic X-rays, light (cathodoluminescence), specimen current and transmitted electrons [5, 14]. In the most common or standard detection mode, secondary electron imaging, the SEM can produce very high-resolution images of a sample surface, revealing details less than 1 nm in size. Back-scattered electrons (BSE) are beam electrons that are reflected from the sample by elastic scattering.

SEM images were recorded with a QUANTA FEI 200 FEG-ESEM system in both configurations: secondary electron and back-scattering. The equipment allows for taking images of the same area in the same time in both configurations. The measurements were performed in vacuum, using different combinations of spot size and energies in order to increase images quality. All the samples must have an appropriate size to fit in the specimen chamber and are generally mounted rigidly on a specimen holder. The tilt of the sample holder was available, and even a 45 degrees tilted holder were used, but all the images presented in this work are top views.

2.4 Bibliography

1. J. Melngailis, *J. Vac. Sci. Techol*. **1987**, *B5(2)*, 469.

2. K. Arshak, M. Mihov, *J. Opto. Adv. Mater*. **2005**, *7(1)*, 193.

3. R. Gerlach, M. Utlaut, Proc. SPIE Charged Particles Detection, Diagnostics, and Imaging, Vol. 4510, 2001.

4. K. Arshak, M. Mihov, A. Arshak, D. McDonagh, D. Sutton, *Microelectronic Engineering* **2004**, *73–74*, 144.

5. N. Yao, Z. L. Wang, Handbook of microscopy for nanotechnology, Kluwer Academic Publisher, 2005.

6. J. Orloff, M. Utlaut, L. Swanson, High Resolution Focused Ion Beams: FIB and Its Applications, Kluwer Academic / Plenum Publishers, New York, 2003.

7. L. A. Giannuzzi, F. A. Stevie, Introduction to focused ion beams: instrumentation, theory, techniques, and practice, Springer USA, 2005.

8. A. Y. Cho, *J. Vac. Sci. Technol*. **1971**, *8*, S31.

9. R. F. C. Farrow, Molecular Beam Epitaxy: Applications to Key Materials, Noyes Publications, New Jersey, USA, 1995.

10. B. Voigtlander, *Surface Science Reports* **2001**, *43*, 127.

11. A. Smekal, *Naturwiss*. **1923**, *11*, 873.

12. C. V. Raman, K. S. Krishnan, *Nature* **1928**, *121(3048)*, 501.

13. E. Smith, G. Dent, Modern Raman Spectroscopy – A Practical Approach, John Wiley & Sons Ltd, West Sussex PO19 8SQ, England 2005.

14. C. P. Poole Jr., F. J. Owens, Introduction to nanotechnology, John Wiley & Sons, Inc., Hoboken, New Jersey, 2003.

15. Z. L. Wang, Characterization of nanophase materials, Wiley VCH Verlag GmbH, 2000.

16. D. K. Schroder, Semiconductor material and device characterization, John Wiley & Sons, Inc., Hoboken, New Jersey, 2006.

17. E. Meyer, H. J. Hug, R. Bennewitz, Scanning Probe Microscopy, Springer, Berlin 2004.

Chapter 3

Influence of Ge nanoclustering on the determination by Raman scattering of composition and strain in $Si_{1-x}Ge_x/Si$ alloys

In this chapter we investigate the influence of Ge nanocluster formation on the vibrational properties of strained $Si_{1-x}Ge_x/Si$ alloy layers with x varied in the 0 - 0.5 range. The spatial distribution of Ge atoms within the alloy layers becomes gradually random as a consequence of the performed sequential thermal annealing steps. Our measurements suggest that the composition dependence of the principal alloy vibrational modes (Ge-Ge, Si-Ge, and Si-Si) for fully random and unstrained alloys is well described by the results previously published by Alonso and Winer [1]. In the general case of an alloy layer with unknown degree of Ge clustering and/or strain relaxation, though, the analysis of the Raman spectra is not straightforward. Hence, we propose an analytical/graphical method to accurately estimate the Ge content and residual strain of SiGe layers exhibiting any Ge clustering degree or strain status, by performing a single Raman measurement, which might be extremely useful in situations where x-ray measurements cannot be conducted. We show that our procedure to treat the Raman data holds for the whole compositional range but with different accuracy depending upon the case, as will be later shown.

3.1 State of the art and motivation

Due to their higher performance as active electronic components compared to pure Si, strained SiGe/Si alloy layers received increasing attention in the last decade. Strained SiGe (s-SiGe) layers are a good alternative to its already well established counterpart because present some advantages such as: larger carrier mobilities [2, 3], higher device switching speeds [4-6], and lower power consumption [7]. Ge was successfully incorporated in a great variety of device architectures such as heterojunction bipolar transistors [8-10] (HBTs), metal-oxide semiconductor field-effect transistors [11-13] (MOSFETs), and optical modulators [14, 15]. The advantages exhibited by this material system partially originate on the different fundamental physical properties of Si and Ge (for details see chapter 1). The larger carrier mobilities [2] exhibited by Ge: μ_e; μ_h = 3900; 1800 cm^2/Vs, compared to those of Si: μ_e; μ_h = 500; 1450 cm^2/Vs imply sharp variations of the electron and hole transport properties of these materials. Hence, the inclusion of Ge in the active layer of Si-based heterostructures is reflected by a substantial increase of the carrier mobilities. Furthermore, the mobilities are affected by the built-in strain which originates from the difference in the lattice constant of Ge (a = 5.658 Å) and Si (a = 5.431 Å). This biaxial ($\varepsilon_{//} = \varepsilon_{xx} = \varepsilon_{yy}$) in-plane strain reduces the cubic crystal symmetry of the SiGe layers leading to the splitting of the heavy- and light-hole valence bands [16], and also to the modification of their effective masses (m_i^*), which influence the carrier mobility ($\mu_i \propto \frac{1}{m_i^*}$). In consequence, the latest development of industry and research requires metrology solutions for the characterization and subsequent precise control of some parameters such as the in-plane strain and alloy composition values, in order to design and fabricate devices with specific transport properties based on strained SiGe layers.

The number of techniques used for strain measurements is quite large; however none of them is without shortcomings when applied to materials used in microelectronics. Among the variety of techniques commonly used for strain and composition determination, x-ray diffraction (XRD) and Raman spectroscopy play a major role. For composition determination other techniques such as Rutherford back-scattering spectroscopy (RBS) and secondary ion mass spectroscopy (SIMS) were employed. The

limitations of these two techniques concern measurement accuracy for thin layers in complicated structures (RBS), and its destructive character (SIMS). However, in some practical situations XRD is not the most convenient technique, e.g., due to the required large crystal lateral size of the samples (typically ~ 1 mm), long measurement time, or due to the necessity of performing angle-resolved measurements or even the need of a synchrotron. Although this technique was applied to a wide range of materials with multiple interests, due to its spatial resolution only the mean value of the stress component can be obtained when is applied for example to lines with μm dimension [17]. In contrast, micro-Raman spectroscopy appears as a suitable alternative since it does not impose any of these technical constraints. Since the diameter of focused laser spot is in micro range (around 1 μm for the visible range) samples typical lateral dimensions are no longer constrained, assuring the successful use for local strain studies.

In theory, by performing a single Raman measurement in back-scattering geometry it is possible to determine a layer composition, providing the in-plane strain, or vice-versa. Several authors already applied this approach to strained SiGe layers [18-22, 24-26], and evidenced in their works the difficulties identified in some situations to reach the desired accuracy. Despite the fact that the underlying mathematics employed to extract composition and/or strain values from the measured Raman spectra is extremely simple, misinterpretation of the experimental results can be easily made due to complex relation between the involved physical parameters. The origin of such drawback of the Raman technique has to be searched and elucidated. In the linear response approximation, the Raman frequencies of the principal alloy vibrational modes (Ge-Ge, Si-Ge and Si-Si) for a biaxially strained SiGe layer read as:

$$\omega^i(x,\varepsilon_{//}) = \omega_0^i(x) + b_s^i(x)\cdot\varepsilon_{//} \tag{3.1}$$

where the superindex i accounts for the Ge-Ge, Si-Ge, or Si-Si vibrational mode, x is the Ge content, $\varepsilon_{//}$ the in-plane strain, ω_0 the phonon frequency for unstrained case, and $b_s(x)$ is the strain shift coefficient. We point out that, strictly speaking, $b_s = b_s(x, \alpha)$ where α accounts for the strain status of the system, since its actual value is determined by the character of the stress being hydrostatic or anisotropic (uniaxial, biaxial, etc.). As revealed in previous works [22, 23], for lower dimensional structures like quantum dots, α strongly depends on the shape of the structure, wetting layer composition, and cap layer thickness. Nevertheless, in the present case of strictly two-dimensional systems, such a

dependence can be neglected due to the pure biaxial nature of the applied stress exerted on the SiGe layers. By performing a single Raman measurement (ω) and with the previous knowledge of ω_0 and b_s, the x or $\varepsilon_{//}$ can be evaluated by means of equation 3.1. Although $b_s^i(x)$ was only recently reported for the whole compositional range by Reparaz et al. [24, 25], and independently calculated by Pezzoli et al. [26], a very poor agreement is found in the literature for the values of $\omega_o^i(x)$. It turns out that the discrepancies appear if the samples were grown using different techniques (see, for example, references 1, 25-27). In consequence, for a given x the determination of $\varepsilon_{//}$ using equation 3.1 results highly unreliable. For example, using the different values for ω_0 reported in references 25 and 27, equation 3.1 give us a difference in $\varepsilon_{//}$ value as high as 1%. Considering that the maximum in-plane strain between Si and Ge is 4.2%, such a high discrepancy is unacceptable. This ambiguity in the values of the unstrained phonon frequency ω_0 in SiGe alloys would, thus, strongly restrict the applicability of the Raman scattering technique alone to the characterization of strained layers of the pure materials. This unfortunate situation constitutes the motivation for the present study.

In this chapter the origin of the large scatter of the ω_0 values reported by the different groups for the unstrained frequency of the optical phonon modes in SiGe alloys [1, 25-27] was investigated. Performing a series of sequential annealing steps to several samples containing a strained SiGe layer with different Ge concentrations, we demonstrate that the formation of Ge nanoclusters during the growth procedure largely determines the value of ω_0 that would be measured by Raman scattering. The optical phonon frequency of the Ge-Ge and Si-Si alloy modes appears to be sensitive to the local composition of the corresponding atomic species. The latter obviously depends on the degree of homogeneity of the sample concerning alloy disorder. Furthermore, we propose a simple analytical/graphical method for the determination of composition and strain in SiGe alloys out of the data from a single Raman measurement. Since the rational of the proposed method takes into account Ge clustering effects, we are able to provide a set of general criteria that allows for the successful processing of the Raman data in almost any experimental situation, irrespective of the degree of alloy disorder and level of strain relaxation of the alloy layers.

3.2 Samples growth conditions

The samples used in this experiment were grown on Si(001) oriented substrates by solid source molecular beam epitaxy (SS-MBE). During all the growth processes the residual pressure of the ultra high vacuum (UHV) inside the MBE growth chamber was ~10^{-9} mbar. In order to desorb the native SiO_2 oxide, the substrates were heated at high temperatures (900ºC), followed by deposition of a thick Si layer (100 nm) while ramping down the temperature from 900 to 500ºC. The temperature of the substrates was maintained constant at 400°C while depositing the alloy layers. The germanium content (x_{Ge}) within the alloy layers was increased from 0 to 0.5, and their thickness was chosen between 7 and 700 nm. A drawing of the grown samples is shown in figure 3.1, offering a general view of the layer sequence. On the one hand, the compositional range used in this work is the one where the differences between the phonon frequencies for relaxed alloy samples determined by different groups, especially for the Ge-Ge phonon, are more pronounced. On the other hand, this interval presents increased interest from the applications point of view. The largest thickness values were chosen to discard the interdiffusion process between the alloy layers and the Si substrates during the annealing steps. A list of all the as grown samples is shown in table 3.1.

Figure 3.1. *Schematic illustration of the $Si_{1-x}Ge_x$ (with $0 < x < 0.5$) alloy samples.*

Table 3.1. $Si_{1-x}Ge_x$ alloy layers thickness (d) for the fabricated samples was determined from optical ellipsometry measurements. Ge composition (x_{xrd}) from x-ray measurements, and calculated one (x_{model}) using the model discussed in section 3.5. All these values are for $Si_{1-x}Ge_x$ alloy layers, grown on a Si(001) oriented substrate, at 400°C by MBE, and before any thermal treatment.

As grown samples	d (nm)	x_{xrd}	x_{model}
A	8	0.15	0.13
B	700	0.18	0.21
C	500	0.22	0.25
D	120	0.4	0.43
E	43	0.44	0.49
F	20	0.47	0.48

As-grown samples were removed from the MBE machine and characterized using spectroscopic ellipsometry, x-ray diffraction (XRD) and Raman spectroscopy. Pieces of the fabricated samples were cut off and re-introduced in the MBE machine in order to perform cumulative thermal annealings for 30 minutes at different temperatures ranging between 400 and 750°C (temperature step was 50ºC). After each annealing step the samples were removed from the chamber for structural and optical inspection, in order to obtain a detailed map of their behavior with thermal treatments. Counting each annealing step, the total number of investigated samples was 48 (6 different concentrations x 8 annealing temperatures). We point out that each annealing stage was performed using the MBE chamber to fully avoid oxidation of the samples due to the low residual pressure of the chamber. Several initial annealing attempts performed in a furnace with Ar (+H_2 ~ 5%) atmosphere had led, despite previous purging of the setup, to strong surface oxidation of the SiGe layers with the consequent evaporation of the silicon oxide at high annealing temperatures. The oxidation process was so strong that implied the reduction of the alloy layers thickness from 500 nm to 410 nm after performing an annealing in furnace with Ar atmosphere at 700°C for 30 minutes. With the purpose of eliminating this strong oxidation process we decided to carry out the experiments inside the MBE chamber in UHV.

Ellipsometry observations were carried out not only for as grown samples, but also after each thermal treatment. The composition, the strain, and the lattice parameter in both out-of-plane (perpendicular) and in-plane (parallel) directions for the pre-annealed samples and the alteration of the SiGe alloy layers parameters after the thermal treatments were investigated by x-ray diffraction (XRD) and Raman measurements performed at room temperature. XRD measurements data for the symmetric reflection (004) were collected for all the investigated samples. X-ray reciprocal space maps (q-plots) around two asymmetric reflections (224) and $(2\bar{2}4)$, were recorded for as-deposited samples and some of the annealed ones. Raman measurements were performed in crossed linear polarization configuration $z(x,y)\bar{z}$, in order to minimize the contribution of the second-order Raman signal (Si 2TA) arising from the Si substrate, whose energy is close to that of the Ge-Ge mode. For all the analyzed samples (before and after thermal treatments) Raman data were collected at four to six different locations on the surface and no significant variations were observed, being within the error bars. In order to precisely determine the composition and strain for the alloy layers, the peak positions have to be determined with high accuracy.

3.3 Some theoretical considerations

When a stress is applied to a solid, it has as consequence the deformation of the crystal structure. In linear response theory the stress is generally written as [28]:

$$\sigma_{ij} = c_{ijkl} \cdot \varepsilon_{kl} \qquad 3.2$$

where σ_{ij} and ε_{kl} are the stress and the strain tensor, respectively, and c_{ijkl} is the fourth-rank tensor corresponding to the elastic constants. The high symmetry of cubic crystals reduces the number of independent components of c_{ijkl} to only three, which expressed in the more comfortable 6x6 matricial form [28] are denoted by C_{11}, C_{12} and C_{44}. In the particular case of a bisotropically stressed layer, it holds $\sigma_{xx} = \sigma_{yy} = \sigma_{//}$, and $\sigma_{zz} = \sigma_{\perp} = 0$. By replacing in equation 3.2 we obtain the two following relations:

$$\sigma_{//} = (C_{11} + C_{12}) \cdot \varepsilon_{//} + C_{12} \cdot \varepsilon_{\perp} \qquad 3.3$$

$$\varepsilon_{\perp} = -\frac{2C_{12}}{C_{11}} \cdot \varepsilon_{//} \qquad 3.4$$

While the equation 3.3 expresses how the stress translates into internal strain, the equation 3.4 stands for the Poisson effect: an in-plane compression/expansion leads to an expansion/compression in the growth direction. In addition, the in-plane strain in the SiGe layers is expressed as $\varepsilon_{//} = \frac{a_{//} - a_{SiGe}}{a_{SiGe}}$, where a_{SiGe} is the lattice constant of the SiGe alloy for $\varepsilon_{ij} = 0(\forall i, j)$. Thus, combining the previous relation with equation 3.1 and 3.4 we obtain a system of two equations, which can be directly related to measurable quantities such as ω^i (obtained from Raman measurements), $a_{//}$ and $a_{\perp}$ (XRD measurements) given by:

$$\omega^i(x, \varepsilon_{//}) = \omega_0^i(x) + b_s^i(x) \cdot \frac{a_{//} - a_{SiGe}(x)}{a_{SiGe}(x)} \qquad 3.5$$

$$\frac{a_{\perp} - a_{SiGe}(x)}{a_{SiGe}(x)} = -\frac{2C_{12}(x)}{C_{11}(x)} \cdot \frac{a_{//} - a_{SiGe}(x)}{a_{SiGe}(x)} \qquad 3.6$$

The equations for $b_s(x)$, $a_{SiGe}(x)$, and $C_{ij}(x)$ are extracted from references 25, 29 and 30, respectively, and are listed in table 3.2. In fact, the determination of x and $\varepsilon_{//}$ can be fully achieved using only equation 3.6 which depends on $a_{//}$ and $a_{\perp}$ only. Nevertheless, as we have already anticipated, it is highly desirable to achieve this only by performing Raman measurements due to the versatility of this technique. The main problem with equation 3.5 is the large scatter in the ω_0^i values, which leads to a large error in the determination of x or $\varepsilon_{//}$. To overcome this inconvenient, the understanding of the origin of the different reported values for ω_0^i is essential. This will naturally lead us to a consistent picture of general validity for the interpretation of the Raman spectra of SiGe alloys. For the sake of clarity, we present first the experimental results and then give an explanation for the observed phenomenology.

Table 3.2. Composition dependence of the strain shift coefficients for the Ge-Ge, Si-Ge, and Si-Si modes extracted from reference 25. Lattice constants and elastic constants extracted from references 29 and 30, respectively. The phonons frequencies at zero strain are extracted from reference 1.

Strain shifts coefficients (cm^{-1})	$b_S^{Ge-Ge}(x) = -190\cdot(x-1)^4 - 460$
	$b_S^{Si-Ge}(x) = -190\cdot(x-1)^4 - 555$
	$b_S^{Si-Si}(x) = -190\cdot(x-1)^4 - 650$
Latice constant (Å)	$a_{SiGe} = 5.431 + 0.198\cdot x + 0.028\cdot x^2$
Elastic constants (GPa)	$C_{11}(x) = 165.77 - 37.24\cdot x$
	$C_{12}(x) = 63.93 - 15.67\cdot x$
Phonon frequency for relaxed samples	$\omega_0^{Ge-Ge}(x) = 284 + 5x + 12x^2$
	$\omega_0^{Si-Ge}(x) = 400 + 29x - 95x^2 + 213x^3 - 170x^4$
	$\omega_0^{Si-Si}(x) = 520 - 68x$

3.4 Origin of the scatter in the ω_0 values

The purpose of this section is to elucidate the origin of the large scatter in the values reported for ω_0 in the literature (see references 1, 24-27). In order to achieve this goal, a series of cumulative sequential annealing steps were performed in samples with different x ranging between 0 and 0.5 (see table 3.1). Figure 3.2 displays representative Raman spectra of the as-grown samples.

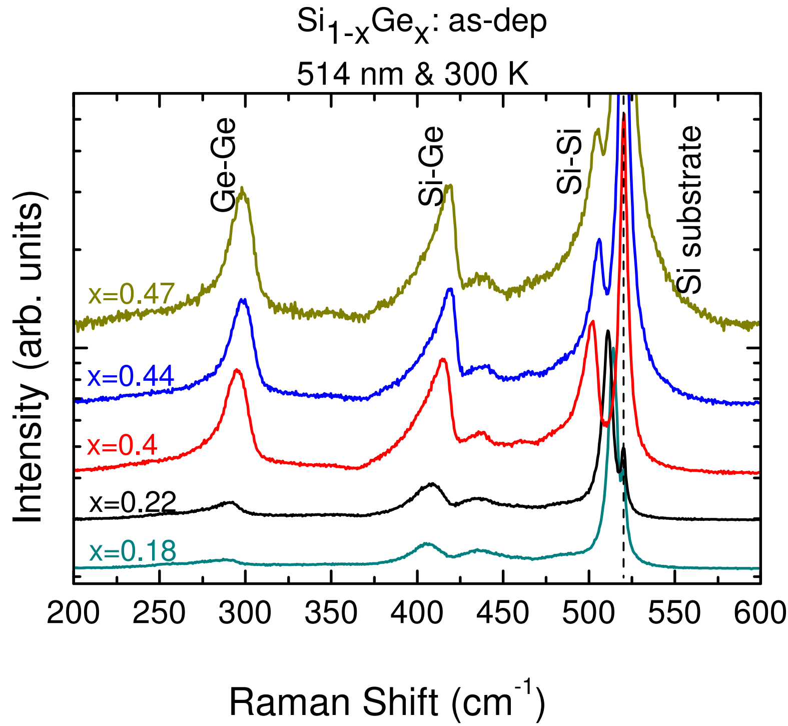

Figure 3.2. *Representative Raman spectra of the $Si_{1-x}Ge_x$ as deposited samples with x = 0.18, 0.22, 0.40, 0.44, 0.47. Peak assignment to the alloy optical modes is indicated. The spectra are plotted in log_{10} scale.*

The strongest peak observed in each spectrum at 520.7 cm^{-1} arises from the Si substrate first-order longitudinal-optical (LO) phonon. For better visualization of the remaining modes, the Si substrate peak intensity has been cut off. Contributions coming from the principal alloy modes are identified in the Raman spectra at lower frequencies as follows: i) $\omega^{GeGe} \sim 300$ cm^{-1}, ii) $\omega^{SiGe} \sim 410$ cm^{-1}, and iii) $\omega^{SiSi} \sim 510$ cm^{-1}. In all the cases the peak intensities have been normalized to that of the LO mode from the Si substrate.

The phonon frequency of each alloy mode for different Ge contents was obtained by fitting the spectra with asymmetric Gaussian line-shapes, whereas for the Si substrate mode a Lorentzian function was used. We anticipate that the Raman spectra of each sample are highly sensitive to the local composition (at the nanoscale) of the alloy layers. Alloys of materials with very dissimilar masses like Si and Ge exhibit peculiar vibrational properties which to a lowest order approximation are roughly described by the so-called one-bond-one-mode model [31]. Within this model, vibrations are highly localized to single bonds, being the main phonon modes of the alloy the ones associated to the three kinds of existing atom pairs Si-Si, Si-Ge, or Ge-Ge. In consequence, the vibrational frequency of each alloy mode is very sensitive to the atomic composition of its immediate environment. Even more important is the fact that the main contribution to the Raman signal stemming from the Ge-Ge and Si-Si modes arises from the Ge and Si-rich regions, respectively. Therefore, in inhomogeneous samples exhibiting certain degree of Ge clustering, the different alloy modes would sense a different average composition and residual strain, the latter in case of a strained alloy layer. In fact, with increasing Ge content the Ge-Ge and Si-Ge modes shift to higher frequencies, whereas the Si-Si mode displays initially a redshift and then a blueshift. Since the alloy layers are all grown epitaxially on Si, the biaxial in-plane strain also increases with Ge content, causing an overall blueshift of the phonon modes. The main issue of this work is to obtain a reliable procedure to separate the contributions to the mode frequency given by equation 3.1 arising from the ω_0 and $\varepsilon_{//}$ terms, which are mixed in the frequency shifts observed in the spectra of figure 3.2 and figure 3.3.

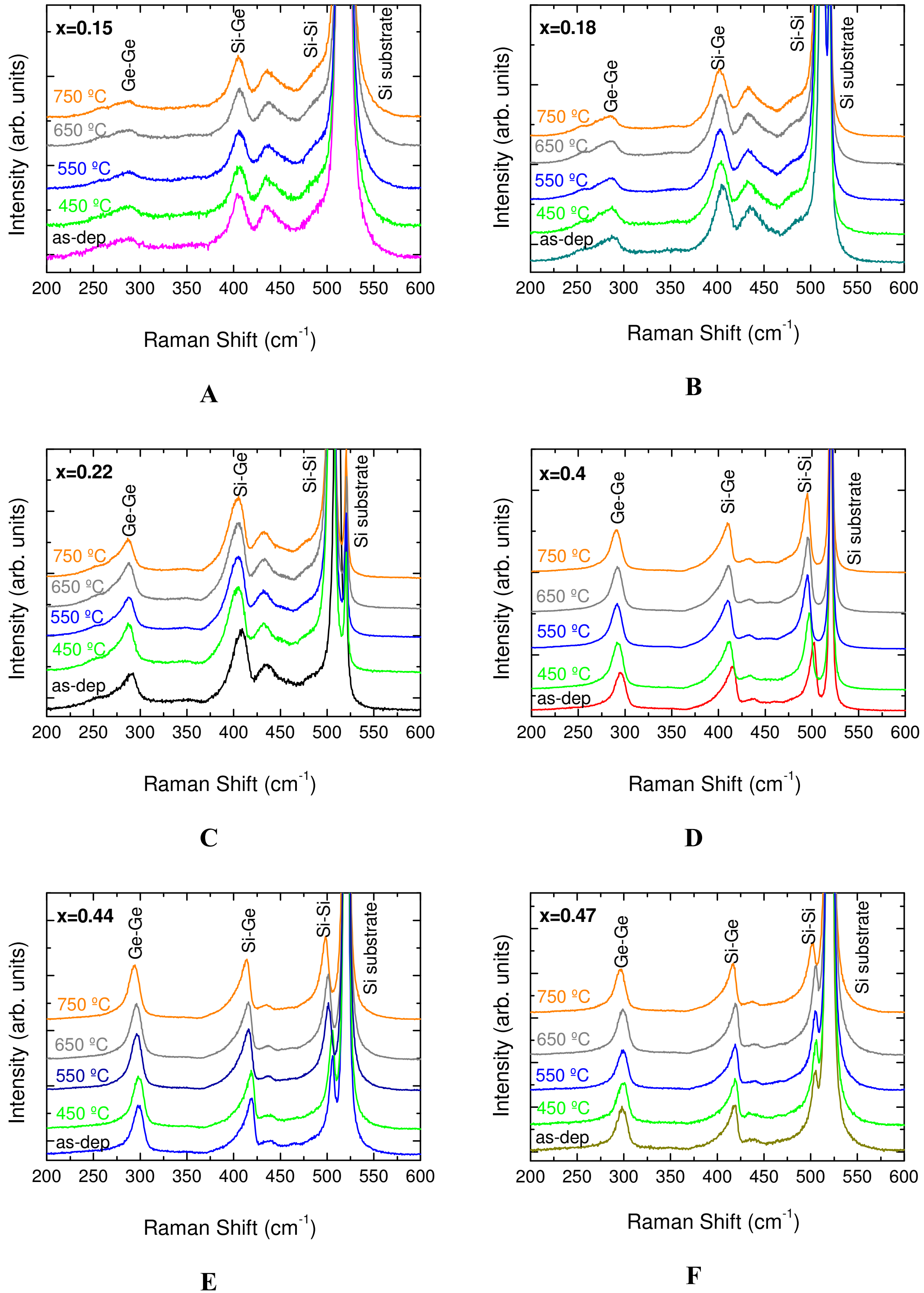

Figure 3.3. *Representative Raman spectra of the as grown samples with x = 0.15 (A), 0.18 (B), 0.22 (C), 0.40 (D), 0.44 (E) and 0.47 (F), and for selected annealing*

temperatures. Peak assignment to the alloy optical modes is indicated. All the spectra were recorded with laser green line (514 nm) at 300K.

The effect of successive thermal annealings on the phonon frequency for all the grown samples is shown in figure 3.3. With increasing annealing temperature, systematic shifts to lower energies were recorded for all the phonon frequencies. Two main candidates appear as responsible for the observed shifts: interdiffusion of Si and Ge between substrate and alloy layer [31] and the combined effect of alloy homogenization by Ge redistribution and strain relaxation within the layers. If interdiffusion occurs, its effect would be to decrease the average Ge content of the layers, which affects in opposite directions the frequencies of the Ge-Ge and Si-Si modes (see figure 3.6).

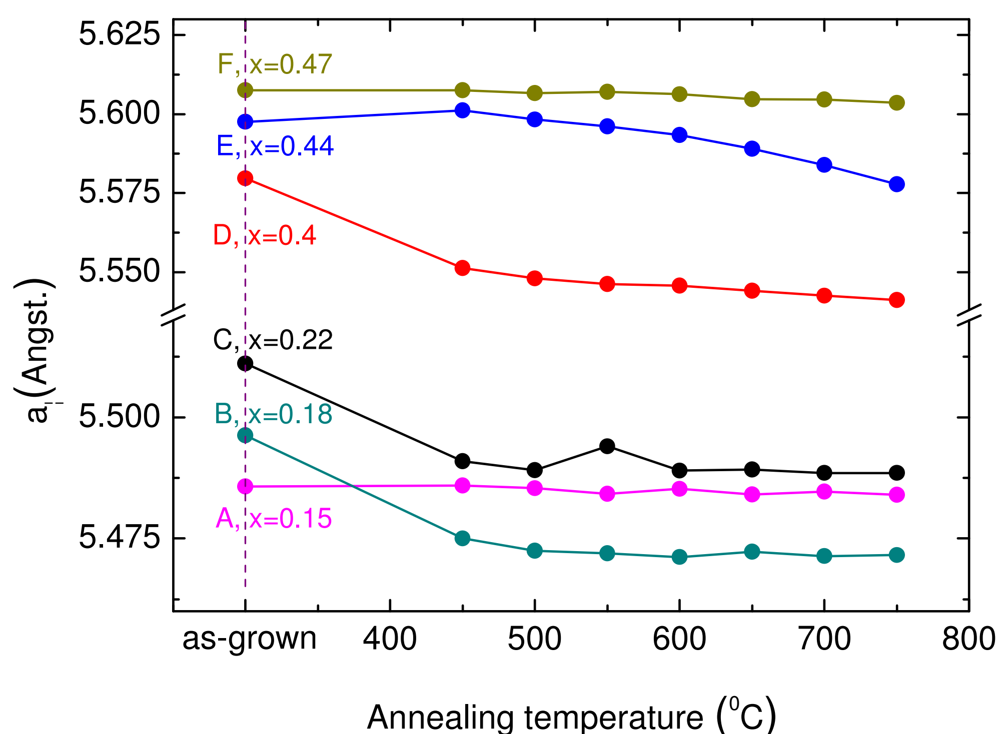

Figure 3.4. *Lattice parameter ($a_\perp$) of the SiGe alloy layers determined by XRD measurements as a function of the annealing temperature for samples A to E. The vertical dashed line corresponds to the as-grown samples.*

A reduction of Ge amount involves a similar behavior for $\varepsilon_{//}$, leading to frequency shifts to lower wavenumbers for all the modes with rates given by b_s^i (see equation 3.5).

In order to discard interdiffusion as the possible cause of the observed frequency shifts upon annealing, we have grown three samples (B, C, and D) with thicknesses large enough to ensure that if interdiffusion with the substrate takes place, its effect is negligible for any practical means. In figure 3.4 the dependence of $a_{\perp}(x)$ on annealing temperature is presented for all the as-grown (thick or thin) alloy layers and thermally treated ones. X-ray reciprocal space maps (not shown) confirmed that all the as-grown samples are pseudomorphic to the Si substrates.

The compositions for the as deposited samples obtained from the XRD measurements were used to calculate some characteristic parameters for the SiGe alloy layers. Obtained values are summarized in table 3.3.

Table 3.3. A summary of the $a_{SiGe}(x)$, $C_{ij}(x)$ and $b_s(x)$ calculated values for SiGe alloy, and their dependence on Ge content within the layers. The equations for the alloy lattice constants and elastic constants used were extracted from the references 29 and 30.

Parameter / **Sample name**	a_{SiGe}	C_{11}	C_{12}	b_{GeGe}	b_{SiSi}	b_{SiGe}
A	5.46	16.01	6.15	-558.48	-748.48	-653.48
B	5.47	15.90	6.11	-545.82	-735.82	-640.82
C	5.48	15.76	6.05	-530.36	-720.36	-625.36
D	5.51	15.08	5.76	-484.56	-674.56	-579.56
E	5.52	14.91	5.69	-477.86	-667.86	-572.86
F	5.53	14.81	5.65	-474.65	-664.65	-569.65

The lattice parameter in parallel direction was calculated by introducing in equation 3.6 the values for the lattice parameter in perpendicular direction illustrated in figure 3.4 and the alloy parameters from table 3.3. The changes recorded for the $a_{//}$ values are coming from the alloy layer relaxation with increasing thermal treatment temperature. Figure 3.4 shows that as the annealing temperature increases, $a_{\perp}$ and $a_{//}$ gradually decrease and increase, respectively, leading to smaller values of $\varepsilon_{//}$ (for details see figure 3.5). This effect is more pronounced for the thicker samples (B, C and D), for which no effects of interdiffusion are expected, indicating almost full relaxation after the

first annealing step. On the contrary, for the thinner samples (A, E and F) strain relaxation is less pronounced, which is easily explained considering that the total elastic energy due to the lattice mismatch with the Si substrate scales linearly with the thickness of the layers. Figure 3.4 constitutes itself an important result since it shows that over a certain thickness, the strained SiGe layers are not stable for increasing temperatures. This might be of crucial importance for a correct design of devices based on strained SiGe layers which are intended to operate above room temperature.

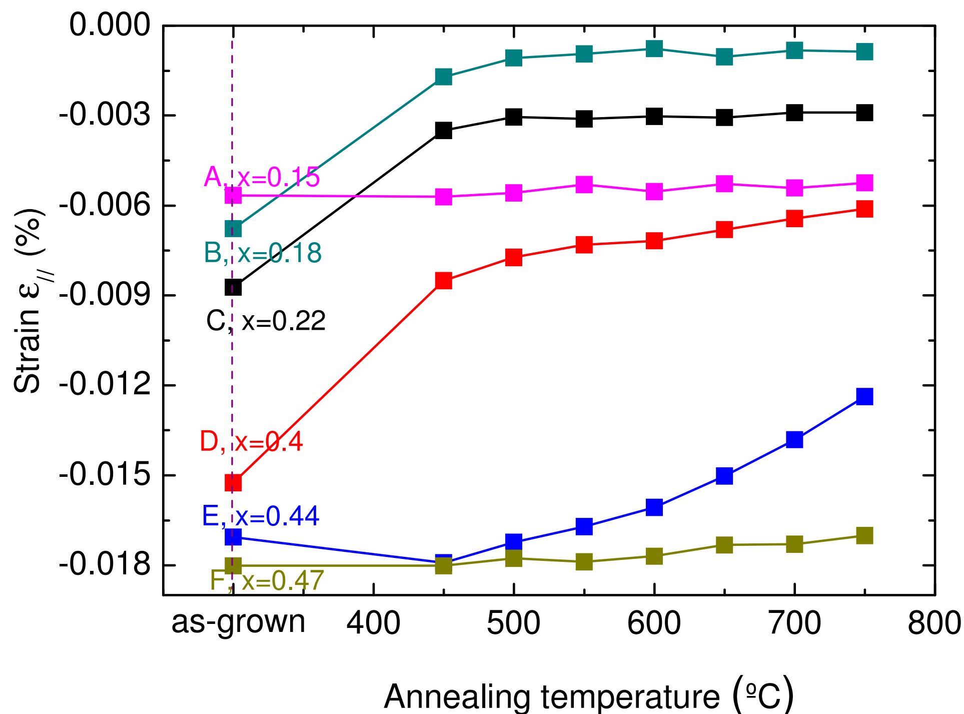

Figure 3.5. *Evolution of the in plane strain ($\varepsilon_{//}$) with the annealing temperature for all the studied samples.*

We turn now to the problem of unrevealing the origin of the sample dependence of ω_0. Taking advantage of the fact that the different samples were investigated by XRD, and of the knowledge of the strain shift coefficients [25], we are able to reverse the problem and compute the value of ω_0 for each sample. According to equations 3.5 and 3.6 this can be solved exactly using the measured values for ω^i and $a_{//}$. For the as-grown samples, since the SiGe layers are pseudomorphic to the substrate ($a_{//} = a_{Si}$) this calculation is straightforward. However, the strain within the layers gradually relaxes ($a_{//}$

$\geq a_{Si}$) as a consequence of the increasing annealing temperature. The computed values of ω_0 for each phonon mode and annealing temperature are shown in figure 3.6. In addition, we have included the reported values from references 1 and 25, which represent two limiting cases for the present set of samples as far as Ge clustering is concerned.

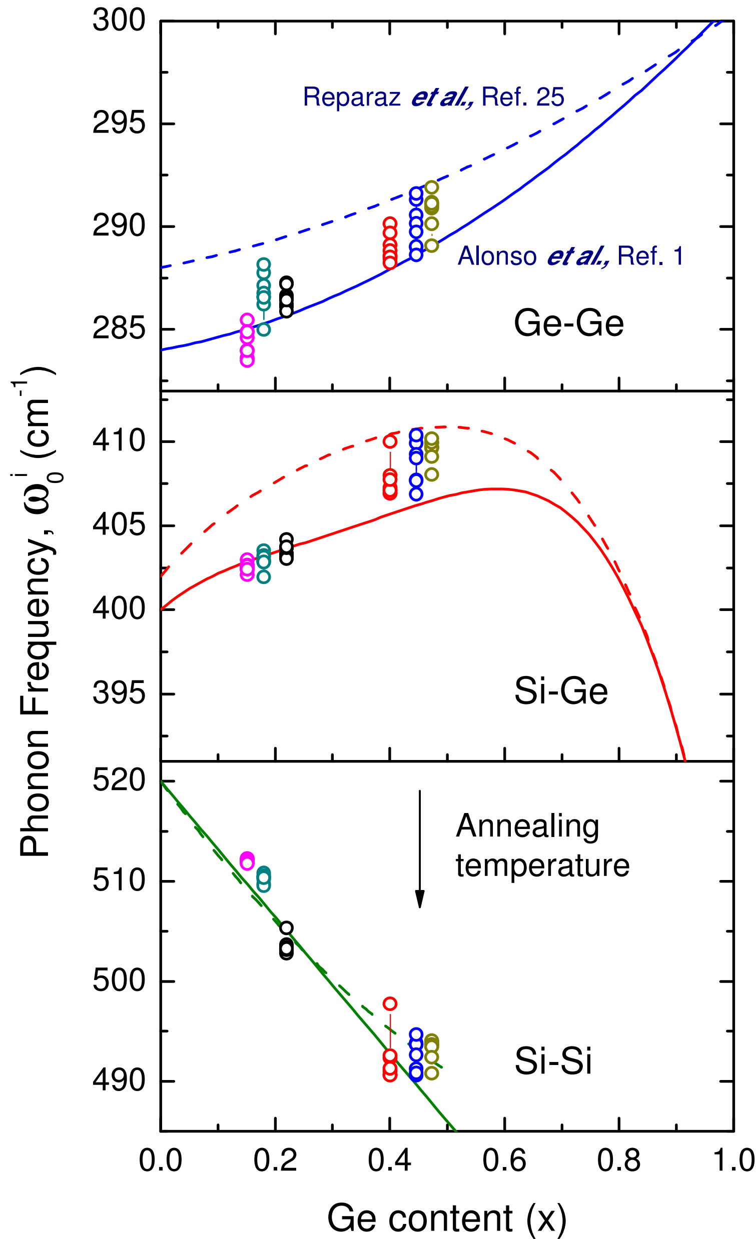

Figure 3.6. *Computed values for* ω_0^i *using equations (3.5) and (3.6) for each vibrational mode and annealing temperature. The dashed and solid curves represent the values for* ω_0^i *from references 1 and 25, respectively.*

The values reported in reference 25 were measured in fully strained samples grown by MBE at 400ºC. Since MBE is an out of equilibrium growth technique, it is known that due to the low deposition temperature, Ge tends to aggregate during the growth of the strained alloy layers. This leads to a non random distribution of the Ge atoms at the nanometric scale [33], which affects the measured values for ω_0. In contrast, the ω_0 values reported in reference 1 arise from samples grown using liquid-phase epitaxy (LPE) which is an equilibrium growth technique and, consequently, the Ge distribution is expected to be as random and homogeneous as possible. The open symbols in figure 3.6 show how the computed values of ω_0 gradually shift from the curve extracted from reference 25 towards those of reference 1. The observed behavior represents the experimental confirmation of our *ansatz* that, despite the fact that the average alloy composition remains essentially constant as revealed by XRD, the distribution of Ge atoms within the layers progressively randomizes with each annealing step, leading to changes in phonon frequencies associated to the progressive dissolution of the Ge clusters.

3.5 Determination of Ge content through a single Raman measurement

In this section is described the procedure by which both x and $\varepsilon_{//}$ can be accurately determined for any strained SiGe layer relying only on a single Raman measurement. To accomplish the proposed objective, we exclusively employ the measured Raman frequencies of the Ge-Ge and Si-Si modes, taking the values of ω_0 extracted from reference 1 as a reference for a random distribution of the Ge atoms within the alloy layer. The Si-Ge mode, in contrast, does not serve to our purpose, due to its approximately flat dependence in the mid-compositional range (see figure 3.6), which makes this mode almost insensitive to composition and/or strain changes.

We demonstrate the procedure choosing as an example the as-grown sample E (x_{xrd} = 0.44) which exhibits the following Raman frequencies: ω^{GeGe} = 299.4 cm^{-1} and ω^{SiSi} = 505.7 cm^{-1}. Applying equation 3.5 independently for each mode we obtain x_{GeGe} = 0.54 and x_{SiSi} = 0.35, which both clearly differ from the average composition x_{xrd} = 0.44, determined by XRD.

The general situation of composition discrepancies determined by the two techniques (Raman and XRD) is schematically illustrated in figure 3.7. In the particular case of sample E, there is a difference of around ±0.1 between the average composition (XRD) and the one determined using the two phonons Ge-Ge and Si-Si (Raman). Depending on the sample initial composition, this difference will not be the same. As the Ge content in the alloy layers is decreased, the composition determined using the Si-Si phonon will be much lower, because this phonon will detect much stronger contribution from the silicon rich regions. On the contrary, for the Ge-Ge phonon an opposite situation to the above described will take place; the contribution will come from Ge rich regions and this phonon would measur a higher Ge content than the average one (see figure 3.7b).

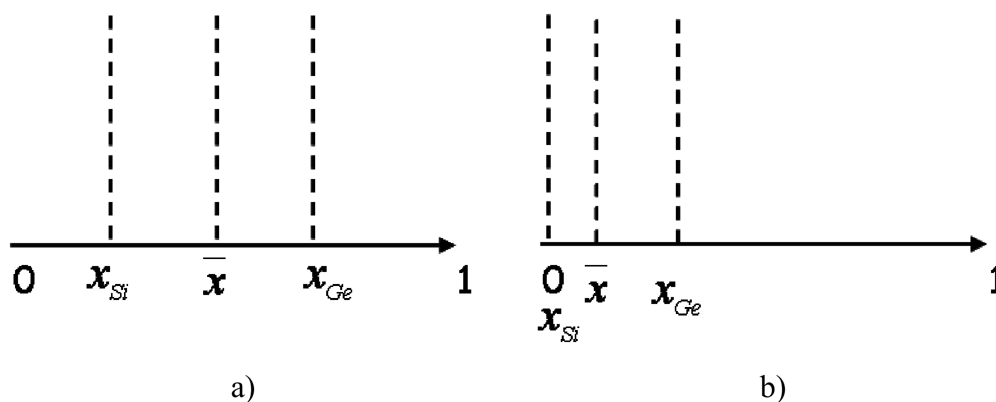

Figure 3.7. *Schematic representation of the average composition ($\bar{x}$ - XRD) and the local ones (x_{Si} and x_{Ge} - Raman) for two cases of the SiGe alloy layers composition.*

We note that whereas XRD explores a comparatively larger volume of the sample, yielding the mean Ge content of the layers (x), the Raman modes are highly sensitive to the local environment surrounding the vibrating atoms. Thus, the formation of Ge nanoclusters is only detected with Raman scattering (x_{Si} and x_{Ge}), but it is not observed in the XRD spectra (x_{xrd}). This effect has been already theoretically studied [34, 35], though no detailed experimental investigation is available to the best of our knowledge. In consequence, we have to modify equation 3.5 in order to include the clustering effect as follows:

$$\omega^{GeGe}(x,\varepsilon_{//}) = \omega_0^{GeGe}(x + m\cdot R) + b_s^i(x)\cdot\varepsilon_{//} \qquad 3.7$$

$$\omega^{SiGe}(x,\varepsilon_{//}) = \omega_0^{SiGe}(x - n\cdot R) + b_s^i(x)\cdot\varepsilon_{//} \qquad 3.8$$

where R is a correction factor to the average composition (x), which accounts for the degree of Ge clustering of the alloy layer. The factors m = 1-x and n = x, in addition, allow for the local composition unbalance for each mode (see figure 3.7). As clearly exemplified in the case of sample E, the Ge-Ge mode always probes a higher Ge content ($x_{GeGe} \geq x_{xrd}$) but the Si-Si mode a lower one ($x_{SiSi} \leq x_{xrd}$). Although m and n are expressed to the first order in x, more sophisticated models with higher order terms are possible. Nevertheless, several attempts using second order terms have brought no real benefits. We remark that no correction is applied to the strain term of equation 3.5, since for the present case $\varepsilon_{//}$ is defined by the lattice mismatch to the Si substrate, as proved by the q-plots in XRD. The process consists in solving equations 3.7 and 3.8 with two unknowns x

and *R*, for all the as-grown samples, for which certainly holds that $a_{//} = a_{Si}$. The obtained layer compositions are listed together with the values obtained from XRD measurements (x_{xrd}) in table 3.1 and labeled as x_{model}. The agreement between these two determinations is more than satisfactory, which demonstrates the validity of the developed method.

We get a step further and relax the condition of pseudomorphism previously imposed, which holds true for the as-grown samples but not for the general case. Now is $a_{//}$ =/= a_{Si} which applies to most of the annealed samples (see figure 3.4), since the effect of the successive annealing steps is not only to randomize the Ge distribution but also to relax (partially or totally) the built-in strain due to the lattice mismatch with the Si substrate. This relaxation condition can be easily expressed by introducing in the strain terms of equation (3.5) a strain factor *S* defined as:

$$\varepsilon_{//} = S \cdot \varepsilon_{iso}(x) = S \cdot \frac{a_{SiGe}(x) - a_{Si}}{a_{SiGe}(x)} \qquad 3.9$$

We note that by definition, *S*=0 represents the fully relaxed case, while *S*=1 corresponds to the fully strained case. With this modification the equations 3.7 and 3.8 read as:

$$\omega^{GeGe}(x, \varepsilon_{//}) = \omega_0^{GeGe}(x + m \cdot R) + b_s^i(x) \cdot S \cdot \varepsilon_{iso}(x) \qquad 3.10$$

$$\omega^{SiGe}(x, \varepsilon_{//}) = \omega_0^{SiGe}(x - n \cdot R) + b_s^i(x) \cdot S \cdot \varepsilon_{iso}(x) \qquad 3.11$$

We face now the problem of solving a system of two coupled equations with *x*, *R*, and *S* as unknowns. Although the present problem is not uniquely solvable for obvious reasons, it is still possible to guess its practical solutions by a graphical procedure. For this purpose, we return to the previously given example on sample E, where we aim to graphically solve equations 3.10 and 3.11. In figure 3.8a we show the three dimensional (3D) plots of the strain parameter *S* = *S*(*x*; *R*) constituting possible solutions of each of those equations. The left surface (orange) corresponds to the solutions for the Si-Si mode, while the right one (violet) relates to the Ge-Ge mode. The intersection between these surfaces gives the physically possible solutions of the problem, in which both strain factors (*S*) from equations 3.10 and 3.11 are equal, i.e. both phonon modes are sensing the same amount of strain relaxation, if any. This intersection curve corresponds to an in-plane strain ranging from 0 to $\varepsilon_{//}^{\max} = \frac{a_{SiGe}(0.44) - a_{Si}}{a_{SiGe}(0.44)}$. It becomes clear from figure 3.8a that the Ge content cannot be directly deduced without making any assumption on the

strain within the alloy layers. This is due to the high Ge content of x = 0.44, which introduces a large strain for pseudomorphic growth on Si, thus, leading to an extended intersection curve which spans an interval of x and R values. Here we make use of what we certainly know from XRD data that the as-grown alloy layers are almost fully strained (S ≅ 1). Closer inspection of similar 3D plots obtained for all other as-grown samples indicate that this condition is always fulfilled for solutions for which the Ge clustering factors R are minimal.

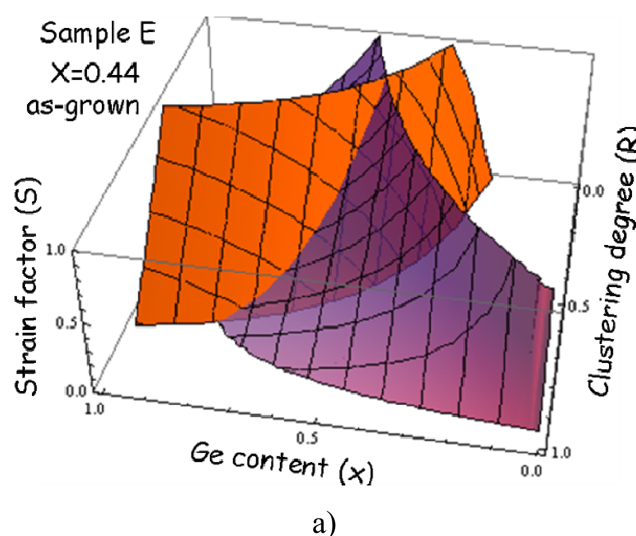

a)

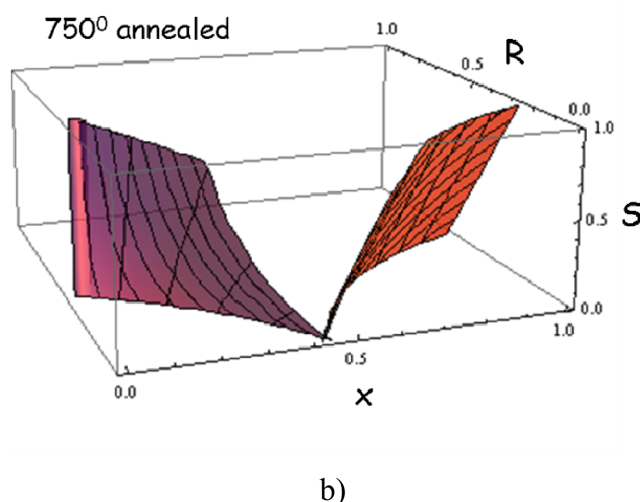

b)

Figure 3.8. *Three dimensional plots showing the solutions of equations (3.10) and (3.11) for the Ge-Ge (right:violet) and Si-Si (left:orange) modes, respectively. In panel (a) we show the two surfaces for the as-grown sample E. The same surfaces are shown in (b) for sample E after all the annealing sequence.*

Next, we consider the case of sample E after all the annealing steps (750ºC). In figure 3.8b we show again the strain factors $S = S(x; R)$ from equations 3.10 and 3.11 plotted together but computed independently. The only difference with the previous case is the measured values for ω^{GeGe} and ω^{SiSi}. The two surfaces exhibit a completely different behavior, being the solution only restricted to almost a single vector in the S - x - R space. In this particular case, it corresponds to the point (S, x, R) = (0.05, 0.43, -0.01), in good agreement with the previous composition determination by XRD x_{xrd} = 0.44 and strain value $\varepsilon \approx 0$ of this sample. The correction factor R results almost zero reflecting the fact that after repeated annealings the distribution of the Ge atoms in the alloy becomes random (see also figure 3.6, where the data points in this case fall on top of the reference curve of reference 1). The 3D plots given in figure 3.8 show that whereas strained layers exhibit a continuous set of solutions over a relatively large compositional range, partially (totally) relaxed layers show a set of solutions with a small compositional dispersion.

Another example of the composition determination for sample C (x_{xrd}=0.22), using the developed model is presented in figure 3.9. The differences between the two plots presented in figure 3.8a and 3.9a are coming from the values of measured phonon Raman frequencies, denoting a different Ge concentration and strain within alloy layers. The Raman frequencies for the as grown sample C were: ω^{GeGe} = 291.3 cm^{-1} and ω^{SiSi} = 511.3 cm^{-1}. Compared to the as grown sample E the intersection between the two planes is generating a smaller interval of x and R values. Following the same procedure than in the case of sample E, the Ge composition was determined using the model to be x_{model}=0.25, in good agreement with the one from XRD (x_{xrd}=0.22).

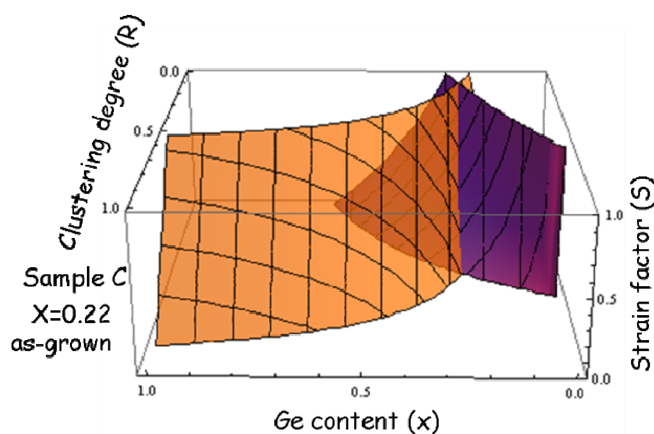

a)

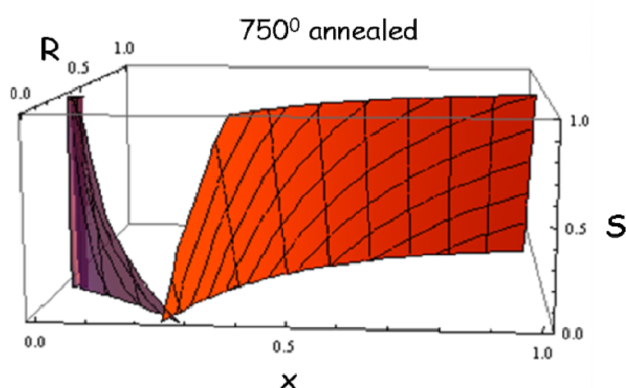

b)

Figure 3.9. *Three dimensional plots showing the solutions of equations (3.10) and (3.11) for the Ge-Ge (right:violet) and Si-Si (left:orange) modes, respectively. In panel (a) we show the two surfaces for the as-grown sample C. The same surfaces are shown in (b) for sample C after all the annealing sequence.*

We show in figure 3.10 the projection onto the *S*, *x* plane of the intersection curves obtained by the procedure demonstrated in figures 3.8 and 3.9 as solutions of the system given by equations 3.10 and 3.11 for all the as-grown (solid lines) samples and the fully annealed ones (lines inside circular marks). The dotted lines represent some kind of contour plots for different values of *R*, though, calculated only for the as-grown samples. While the solutions for strained samples exhibit an interval of compositions, the relaxed layers converge to almost a unique solution.

Figure 3.10. *Solutions of equations 3.10 and 3.11 for all the as-grown samples (solid lines) and annealed ones (circled lines) represented in the (S, x) plane. The dotted black lines connect points with constant values of the clustering parameter R, representing real solutions, whereas the grey dotted lines are a guide to the eye, representing estimated solutions.*

In the latter case, we estimate from figure 3.10 that the accuracy (relative error bars) in the determination of the Ge content is below 2%. For the strained samples, an extra criterion must be adopted due to extra variability introduced by the in-plane strain present in the alloy layers. Although all (S, x) points on the curves plotted in figure 3.10 are mathematical solutions of the problem, only those with a minimum clustering degree are physically realistic. From an exhaustive analysis of all the 48 investigated samples we have found that the upper limits for the relative error in the determination of the Ge content rises to 3% for $x < 0.3$ and 6% for $x > 0.3$. We note that larger values of R corresponding to very large clustering degrees are possible in highly inhomogeneous samples which, nevertheless, are not usually obtained with the conventional epitaxial

growth techniques. In practice, it is possible to estimate x and $\varepsilon_{//}$ using the following procedure:

1. Measure the Raman spectrum of a given sample and extract ω^{SiSi} and ω^{GeGe}.

2. Using equations 3.10 and 3.11 construct the curve given by the constrain $S^{GeGe}(x, R) = S^{SiSi}(x, R)$, obtaining a similar plot to that shown in figure 3.10.

3. Deduce the Ge content and residual strain by analyzing the extension of the plotted curve: if the intersection curve clasp a whole interval of strain factors containing $S \cong 1$, then the alloy is under large biaxial strain and the most likely solution is obtained by minimizing the Ge clustering parameter R. Otherwise, for almost strain relaxed samples the intersection curve restricts itself to a short segment around values of S close to zero and the solution is obtained with more or less accuracy directly from the graph.

3.6 Conclusions

The results reported above have provided deeper insight into the vibrational properties of semiconductor alloys, which turned out to be crucial for the quantitative understanding of their Raman spectra. In particular, we have found that the formation during epitaxial growth of Ge nanoclusters is the origin of the large scatter of the values reported for the unstrained frequency ω_0 of the vibrational modes in SiGe alloys measured by Raman scattering. We have shown that this effect is particularly important in samples grown using nonequilibrium, epitaxial methods like MBE, whereas it is almost absent for growth techniques such as LPE, where the alloy crystallizes onto the substrate following an equilibrium phase diagram. On this basis, we conclude that for fully random alloys ω_0 can be reliably obtained from the results published by Alonso and Winer [1].

Additionally, we have developed a simple model that explains the behavior of the alloy phonon modes, valid for samples exhibiting any degree of Ge clustering and strain status. Within this model we introduce a correction to the Ge content in the form $x \rightarrow (x + m \cdot R)$ for the Ge-Ge mode and $x \rightarrow (x - n \cdot R)$ for the Si-Si mode to simultaneously fulfill the equations for the phonon mode frequency $\omega^{GeGe} = \omega(x + m \cdot R, \varepsilon_{//})$ and $\omega^{SiSi} = \omega(x - n \cdot R, \varepsilon_{//})$, as given in reference 1. This system can be solved exactly if $\varepsilon_{//}$ is known a priori, but requires an approximate graphical solution for situations where $\varepsilon_{//}$ is unknown. In this way, we have successfully revisited the problem of the experimental determination of alloy composition and residual strain by performing a single Raman measurement. In practice, our analytical/graphical method should be extremely useful in situations where XRD measurements cannot be conducted, repositioning the Raman spectroscopy technique among the top characterization tools in semiconductor nano/micro-technology.

3.7 Bibliography

1. M. I. Alonso, K. Winer, *Phys. Rev. B* **1989**, *39*, 10056.
2. F. Schaffler, *Semi. Sci. Technol.* **1997**, *12*, 1515.
3. M. V. Fischetti, S. E. Laux, *J. Appl. Phys*. **1996**, *80*, 2234.
4. M. Kondo, K. Oda, E. Ohue, H. Shimamoto, M. Tanabe, T. Onai, K. Washio, *IEEE Trans. Electron. Devices* **1998**, *45*, 1287.
5. A. Gruhle, *IEEE Trans. Electron. Devices* **1994**, *41*, 198.
6. R. Krithivasan, G. Niu, J. D. Cressler, S. M. Currie, K. E. Fritz, R. A. Reed, P. W. Marshall, P. A. Riggs, B. A. Randall, B. Gilbert, *IEEE Trans. Nucl. Sci*. **2003**, *50*, 2126.
7. S. Takagi, T. Irisawa, T. Tezuka, T. Numata, S. Nakaharai, N. Hirashita, Y. Moriyama, K. Usuda, E. Toyoda, S. Dissanayake, M. Shichijo, R. Nakane, S. Sugahara, M. Takenaka, N. Sugiyama, *IEEE Trans. Electron. Devices* **2008**, *55*, 21.
8. J. D. Cressler, *IEEE Trans. Microwave Theory Tech*. **1998**, *46*, 572.
9. D. L. Harame, J. H. Comfort, J. D. Cressler, E. F. Crabbe, J. Y.-C. Sun, B. S. Meyerson, T. Tice, *IEEE Trans. Electron. Devices* **1995**, *42*, 455.
10. A. Gruhle, H. Kibbel, U. Konig, U. Erben, E. Kasper, *IEEE Electron Device Lett*. **1992**, *13*, 206.
11. R. Oberhuber, G. Zandler, P. Vogl, *Phys. Rev. B* **1998**, *58*, 9941.
12. S. Verdonckt-Vandebroek, E. F. Crabbe, B. S. Meyerson, D. L. Harame, P. J. Restle, J. M. C. Stork, J. B. Johnson, *IEEE Trans. Electron. Devices* **1994**, *41*, 90.
13. T. Mizuno, S. Takagi, N. Sugiyama, H. Satake, A. Kurobe, A. Toriumi, *IEEE Electron Device Lett*. **2000**, *21*, 230.
14. D. Marris, A. Cordat, D. Pascal, A. Koster, E. Cassan, L. Vivien, S. Laval, *IEEE J. Sel. Top. Quantum Electron*. **2003**, *9*, 747.
15. O. Qasaimeh, J. Singh, P. Bhattacharya, *IEEE J. Quantum Elec*. 1997, *33*, 1532.
16. D. J. Paul, *Semicond. Sci. Technol*. **2004**, *19*, R75.
17. B. Greenebaum, A. I. Sauter, P. A. Flinn, W. D. Nix, *Appl. Phys. Lett.* **1991**, *58*, 1845.
18. T. S. Perova, R. A. Moore, K. Lyutovich, M. Oehme, E. Kasper, *Thin Solid Films* **2008**, *517*, 265.

19. F. Pezzoli, E. Bonera, E. Grilli, M. Guzzi, S. Sanguinetti, D. Chrastina, G. Isella, H. von Kanel, E. Wintersberger, J. Stangl, G. Bauer, *Mat. Sci. Semicond. Process*. **2008**, *11*, 279.

20. P. Dobrosz, S. J. Bull, S. H. Olsen, A. G. O'Neill, *Surf. Coat. Technol*. **2005**, *200*, 1755.

21. J. Schmidt, G. Vogg, F. Bensch, S. Kreuzer, P. Ramm, S. Zollner, R. Liu, P. Wennekers, *Mat. Sci. Semicon. Process*. **2005**, *8*, 267.

22. J. S. Reparaz, A. Bernardi, A. R. Goni, P. D. Lacharmoise, M. I. Alonso, M. Garriga, J. Novak, I. Vavra, *Appl. Phys. Lett*. **2007**, *91*, 081914.

23. A. Bernardi, J. S. Reparaz, A. R. Goni, M. I. Alonso, M. Garriga, *Phys. Status Solidi B* **2007**, *244*, 76.

24. J. S. Reparaz, A. Bernardi, A. R. Goni, M. I. Alonso, M. Garriga, *Phys. Status Solidi B*. **2009**, *246*, 548.

25. J. S. Reparaz, A. Bernardi, A. R. Goni, M. I. Alonso, M. Garriga, *Appl. Phys. Lett*. **2008**, *92*, 081909.

26. F. Pezzoli, E. Bonera, E. Grilli, M. Guzzi, S. Sanguinetti, D. Chrastina, G. Isella, H. von Kanel, E. Wintersberger, J. Stangl, G. Bauer, *J. Appl. Phys*. **2008**, *103*, 093521.

27. V. A. Volodin, M. D. Efremov, A. S. Deryabin, L. V. Sokolov, *Semiconductors* **2006**, *40*, 1314.

28. J. F. Nye, "*Physical properties of crystals*", Clarendon, Oxford, **1985**.

29. J. P. Dismukes, L. Ekstrom, R. J. Paff, *J. Phys. Chem*. **1964**, *68*, 3021.

30. F. Schaffler, Eds. M. E. Levinshtein, S. L. Rumyantsev, M. S. Shur, John Wiley & Sons, Inc., New York, 149-188, **2001**.

31. For a general discussion of phonons modes in semiconductors alloys within the percolation scheme see O. Pages, J. Souhabi, A. V. Postnikov, A. Chafi, *Phys. Rev. B* **2009**, *80*, 035204.

32. Y. M. Chang, C. L. Dai, T. C. Cheng, C. W. Hsu, *Appl. Surf. Sci*. **2008**, *254*, 3105.

33. J. Tersoff, *Phys. Rev. Lett*. **1996**, *77*, 2017.

34. E. Ko, M. Jain, J. R. Chelikowsky, *J. Chem. Phys*. **2002**, *117*, 3476.

35. M. Z. Hossain, H. T. Johnson, *J. Appl. Phys*. **2010**, *107*, 073515.

Chapter 4

Growth of Ge nanostructures on *focused ion beam* patterned Si substrates

In this chapter we investigated the formation and evolution of different Ge nanostructures on focused ion beam (FIB) patterned Si substrates with different orientations. The developed experimental procedure consists mainly of three steps: i) focused ion beam (FIB) nano patterning, ii) ultra high vacuum (UHV) annealings and iii) solid source molecular beam epitaxy (SS-MBE) deposition. During the first step (i) a focused ion beam equipment with Au^{2+} ions was employed to pattern the Si substrates in order to achieve a good control on the order and exact location of the nanostructures. Two procedures were followed to pattern the Si substrates: first we performed a FIB ultra fast grabbing process (scans), and in the second approach the substrates were patterned with holes. The FIB parameters were modified in order to induce changes on Si substrates morphology and to tailor the Au amount inside patterned areas.

In the second step (ii) the evolution of the hole morphology with increasing annealing time and temperature was investigated for both (001) and (111) Si substrate crystallographic orientations. We show that FIB allows for the local implantation of the Au in the areas impacted by the ion beam. Additionally, the implanted Au from a large ion dose range ($44x10^{-4}$ C/cm^2 - $240x10^{-4}$ C/cm^2) evolves during annealing into AuSi clusters.

In the third step (iii) Ge was deposited by solid source molecular beam epitaxy (SS-MBE) on top of the Si patterned substrates. The influence of the Au on the Ge

nanostructures growth, morphology, dimensions, size uniformity and density was investigated for both approaches (scans and holes) of the used patterning technique. Moreover, we demonstrate that increasing the Au ion dose the resulting Ge islands (low ion dose) evolve to nanowires (NWs) (intermediate ion dose), and then to 2D Ge layers (high ion doses). Depending on the investigated position in the samples (patterned or non-patterned) a variety of Ge nanostructures were obtained: islands, nanowires and 2D layers. For low ion doses uniform and pattern ordered Ge islands are obtained inside patterned areas while outside random growth takes place. Dome shaped islands were grown between the holes (Au rich areas) while inside the holes pyramidal shaped islands are present. Increasing the Au amount, island dimensions decreased, while their density inside the holes increased. Using ion doses from the intermediate range AuSi clusters were formed during the annealing and served as nucleation seeds for the nucleation and growth of Ge NWs. We obtain Ge NWs of homogeneous dimensions and oriented in-plane along [110] directions, as a consequence of a strain-driven process. Wire kinking is governed by surface morphological features. Thus, we prove that FIB with Au^{2+} ions is a useful method to obtain gold-catalyzed self-assembled nanowires.

4.1 Introduction

Self-assembled Ge quantum dots received considerable attention due to their good compatibility with modern silicon technology, and especially for their potential applications in optoelectronics and photonics. For the development of devices based on this material system a precise knowledge of the optical and electrical properties of Ge quantum dots is mandatory. Furthermore, to tune island properties, the achievement of a good control of their parameters such as: size, shape, density, homogeneity, and strain is essential [1]. In addition, another important issue is the ability of controlling the island spatial position in the substrates, which can be achieved by the creation of preferential nucleation sites. Since Ge exhibits a spatial random growth on Si flat surfaces, substrate patterning can be used to control the position of the nanostructures. Many approaches were followed in the attempt to grow ordered and uniform self assembled dots, including: mesas [2], masks [3, 4], nanosphere lithography [5], or other techniques [6, 7]. The influence of Au masks on Ge islands morphology, dimensions, shape and location on the substrates was also studied [3, 8, 9].

In order to decrease the island dimensions, to increase their density and tailor their position, the use of patterning techniques is required. Focused ion beam (FIB) is a unique technique capable to directly pattern the Si substrates with a high spatial resolution. Using FIB it is possible to modify hole widths, depths and spacings in order to trap the deposited material in a controlled way. The inter-dot distance was reduced to ~20 nm when Si substrates were FIB patterned using Ga^+ ions [10, 11]. The FIB patterns performed either on Si substrates or oxide layers demonstrated their capability of controlling the nucleation of large arrays of Ge islands [12-14]. Besides patterning, the growth methods and growth conditions can be used to tune in broad ranges Ge island properties, such as size, density and even composition [15]. It was demonstrated that the growth temperature has a strong influence on island positions within the patterns: Ge islands grown either on defect sites, inside the holes (550ºC), or between the holes (750ºC) [10, 16]. The role of Ga^+ ions implanted with FIB on the formation of preferential nucleation sites for the nanostructures, and their influence on the island size and density was reported [12] and is better known compared to the Au one.

Additionally, the FIB equipment was used to pattern the substrates and to achieve the growth of the nanowires (NWs) at determined positions [17, 18]. The nanowires growth locations are determined by the spatial employment of the catalyst [19]. Focused ion beam with an AuSi liquid metal alloy ion source presents the great advantage of both substrate patterning capability and Au ions presence, offering a high control of their spatial location and amount.

Up to date various methods to fabricate semiconductor nanowires have been reported, such as vapor–liquid–solid (VLS) growth [20-22], solid–liquid–solid (SLS) growth [23], oxide-assisted growth [24], vapor–solid–solid (VSS) growth [25-27], electroless metal deposition (EMD) method [28, 29] and others [30-32]. Despite the large number of studies reporting the modifications of the NWs diameter by using different ambient gases [33, 34], ambient pressure [35, 36], and catalyst clusters of homogeneous size [37, 38], most of the processes often resulted in NWs with inhomogeneous diameters and lengths, randomly oriented and positioned. Even though elementary processes of NW growth using VLS mechanism have been investigated [39-41] a complete understanding of the driving force controlling the shape is still missing. The advantages offered by the usage of the FIB equipment with Au^{2+} ions (no need for the Au deposition, mask less patterning process, Au amount can be tailored easily, positioning of the Au ions and the holes at desired locations within the substrates, flexibility in tailoring hole dimensions, but in the same time their uniformity is assured, etc.) can be exploited in order to overcome these shortcomings. We patterned the Si substrates using a FIB equipment with Au^{2+} ions (ultra fast grabbing process and holes patterning) and investigated both pattern types and Au influence on the Ge nanostructures growth mode and morphology.

4.2 Sample preparation

The developed experimental procedure consists of three steps: (i) FIB nanopatterning; (ii) annealing of patterned Si substrates and AuSi clusters formation, and (iii) Ge nanostructure growth by solid source molecular beam epitaxy. Two types of Si substrates with (111) orientation and a resistivity of 6-8 Ωcm, and (001) doped with boron at $5x10^{17}$ cm^{-3} were used.

During step (i) both substrate orientations were FIB patterned following two approaches: 1) ultra fast grabbing process (scans) and 2) hole patterning. Although, both procedures allow for tailoring the Au amount, a much better control is achieved for the case of holes. Using the ultra fast grabbing process each substrate was imaged with nine squares (400x400 μm^2) performed for different conditions: pixel number (512, 768 and 1024 pixels) and different speed settings (see table 4.1). During the grabbing process the incident Au ions were locally implanted into the substrates. In order to increase the Au amount, multiple scans were performed in the same areas of the Si substrates.

Table 4.1. Correspondence of the scan times to different speed settings.

Speed setting	2	3	4	5	6	7	8
Scan time (μs/pxl)	0.6	1.8	5.4	16.2	48.6	145	437.4

In the second approach, hole patterning, several arrays of nano-holes were milled using FIB with Au^{2+} ions. During formation of the holes, Au is locally implanted in the hole walls (inner holes surface), and in a reduced amount even between the holes and nearby the patterned squares. The 2D periodic arrays of patterns were performed following two exposure procedures either parallel or serial, with no beam blanking between two consecutive impacts. Using the parallel procedure the holes will be performed one by one with a single pass of the FIB beam, while for the serial mode the holes will be the result of several passes. To tailor the hole lateral diameter and depth, we varied the ion beam current, dose, dwell time, overlap, probe current, probe aperture, and spot size. The ion beam current employed ranged from 1 to 100 pA, the dwell time was

between 0.8 and 500 μs, and an overlap of 1 was normally chosen. Different ion beam conditions were obtained by changing the probe aperture from 10 to 50 μm. The exposure doses were also varied by changing the writing time for one hole between 0.04 and 569 milliseconds (ms). Different Au ion doses ranging between $1x10^{-4}$ C/cm^2 and $265.5x10^{-4}$ C/cm^2 were used in order to control the dimensions of the holes and the Au amount. Usually, the size of the holes patterned areas were 25x25 or 50x50 μm^2, and the total patterning time was varied between 100 ms and 20 minutes. For different patterning conditions the distance between the holes was increased from 0.07 to 1.5 μm.

The FIB patterned Si substrates were systematically cleaned *ex-situ* using a modified Shiraki [42] recipe:

i) immersion for 5 minutes in HNO_3 (65 %) heated at 70 ºC;
ii) introduction for 30 seconds to 1 minute in deionized water;
iii) immersion for 30 seconds in HF (49 %) : H_2O (1:10).

The substrates were passivated, H terminated, by the usage of HF in the last step. No cleaning step for Au removal of the patterned substrates was performed. The same cleaning procedure was performed between each annealing step.

After the cleaning stage the patterned Si substrates were immediately introduced into the ultra high vacuum (UHV) growth chamber of the solid source molecular beam epitaxy (SS-MBE) equipment. The annealings were performed at temperatures ranging from 300ºC to 850ºC for 15 minutes to 2 hours. The evolution of the holes with increasing annealing time and temperature was investigated by performing AFM and SEM measurements in order to tailor their dimensions and to establish the influence of these two parameters on hole morphology. The formation of the AuSi clusters inside the patterned areas was investigated at various combinations of the annealing temperature and time.

Subsequent to the patterning and annealing steps, Ge was deposited on the Si substrates in both patterned and non-patterned areas. Based on our previous experiments and on reported data in the literature [16], we selected the growth temperatures between 400 and 550°C. The amount of Ge deposited was varied between 2 and 12 nm and different growth rates were employed ($3.5x10^{-2}$ - $9x10^{-2}$ nm/s). A uniform deposition rate along the Si substrates was ensured by its continuous rotation. After the deposition stage, the temperature was immediately lowered following a ramp of 20ºC/min until 250ºC. After each process step (FIB patterning, annealing and growth) the samples were ex-situ

systematically investigated by atomic force microscopy (AFM) in air and scanning electron microscopy (SEM).

4.3 Self assembled growth of Ge islands on Si substrates patterned by focused ion beam

4.3.1 Ultra fast grabbing process - *single scan*

The experiments were started using the FIB ultra fast grabbing process (single scan) in the attempt to obtain uniform and pattern ordered Ge islands. Employing this approach Si substrates with (001) and (111) crystallographic orientations were imaged using FIB with Au^{2+} ions. The control of the Au amount was achieved by modifying the pixels number and the scan time (see table 4.1).

After performing the ultra fast grabbing process using small scan times (0.6 – 16.2 µs/pxl) it was not possible to detect by means of AFM or SEM any difference between the Ge islands formed in the imaged and the non-imaged FIB areas, therefore, no images are shown. By "imaged" area we referred to the FIB scanned region, while the "non-imaged" named the rest of the sample, outside the FIB squares. The Au amount present inside the scanned areas was too low to produce visible changes on the growth mode or morphology of the Ge islands. The imaging time was increased (from 48.6 to 437.4 µs/pxl) by reducing the speed setting. As a consequence, ordered Ge islands were grown on the patterns for both Si substrate orientations and all pixels numbers. The differences between Ge island growth on FIB imaged and non-imaged areas were clearly seen for both Si substrates orientations (see figures 4.1 and 4.2). Outside imaged areas, Ge islands were formed (pyramid and dome shaped) with a random distribution, as revealed by figure 4.1a. The SEM image recorded on a FIB imaged area (see figure 4.1b) proved a different growth mode and a certain order of the Ge islands due to the pattern. Island dimensions inside the FIB imaged squares were reduced compared to the outside ones due to the presence of Au. Since both (001) and (111) orientations were grown at the same time (our equipment was furnished with a sample holder which permits depositing up to 6 samples with different sizes at the same time) the differences recorded between the nanostructures obtained on the two substrates cannot be caused by the growth conditions. Even when we used the same grabbing conditions for both orientations,

Si(111) substrate was proved to be more favorable for the ordering of the Ge islands (see figure 4.1b and 4.2b).

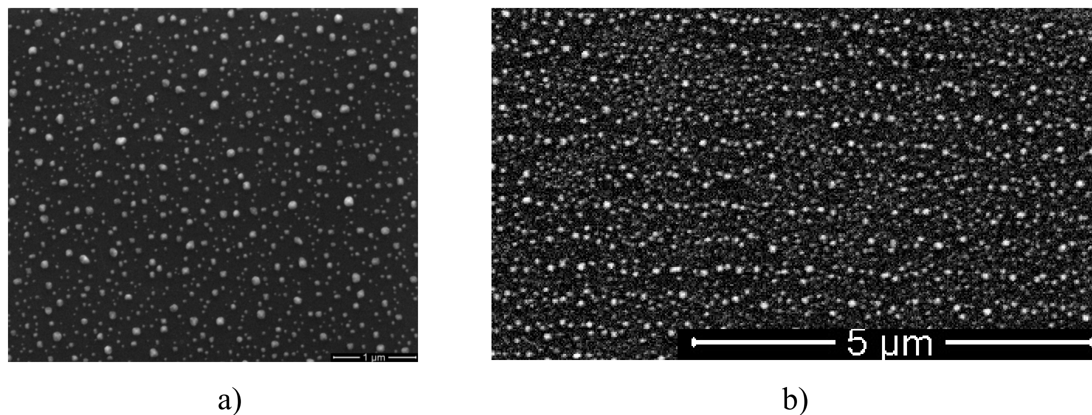

a) b)

Figure 4.1. *SEM images recorded for a Si(001) substrate on a non-imaged area (a) and a ultra fast grabbed area (b). The Si(001) substrate was FIB imaged by performing a single scan: 437.4 µs/pxl and 1024 pixels. The deposition temperature for the Ge (2 nm) was 550ºC.*

SEM images recorded after Ge deposition on Si(111) inside the FIB scans performed with 786 and 1024 pixels (437.4 µs/pxl) are shown in figure 4.2a and b. Surprisingly, the grabbing process is not uniform inside the FIB imaged areas (see figure 4.2). We make distinction between these areas by naming them as FIB "impacted" (some of them marked in figure 4.2 by yellow circles) and "non-impacted" areas – the rest of the FIB imaged squares. Inside these FIB imaged regions, the Au amount was different between the impacted and non-impacted areas, which had a direct influence on the Ge islands growth.

The distance between the FIB impacted areas is well correlated with the pixel number. Increasing pixel number (from 512 to 1024 pixels), the distance between impacted areas was reduced (from 1 µm to 0.5 µm). As a consequence of the increased pixel number, the distance between Au rich spots was reduced and a better order for the Ge islands was achieved (figure 4.2 from a to b). For 1024 pixels a single dome shaped Ge island tends to grow between four Au rich areas, as showed in the large scale SEM image (inset of figure 4.2b - Au rich areas are situated inside the yellow circles). Inside the Au rich areas island dimensions were considerably reduced and the order was lost. More than one island per hole was formed inside the FIB impacted areas. The increased

order of the islands is the result of the smaller distance between impacted areas (Au rich areas) and is in good agreement with the model developed by Li et al. [43]. The position of the Ge islands between four Au rich areas is also consistent with the previous results reported by Robinson et al. [9]. A change of the surface chemical potential is induced by the presence of Au and, thus the Ge islands grow between the Au rich areas. The best result regarding Ge islands position, order and size uniformity was obtained for the scan performed with the largest time (437.4 µs/pxl) and 1024 pixels (figure 4.2b).

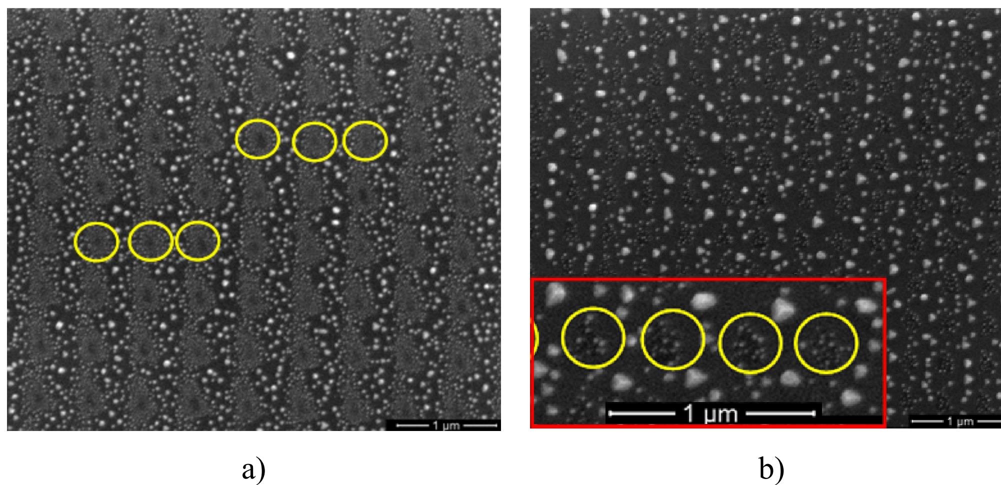

a) b)

Figure 4.2. *SEM images for a Si(111) substrate FIB imaged with a single scan (437.4 µs/pxl) using: a) 786 pixels and b) 1024 pixels, with 2 nm of Ge deposited at 550ºC. With yellow circles are marked some of the FIB impacted areas situated inside the FIB imaged regions.*

4.3.2 Ultra fast grabbing process - *multiple scans*

In order to increase the Au amount and follow its influence on the Ge islands growth mode, the largest scan time was kept fixed and the scan number was increased from 1 to 9 (imaging the same area). After the annealing and Ge deposition steps, both performed under the same conditions as for the previous samples, Ge islands grow in between the areas impacted by FIB (figure 4.3a), while inside these areas no islands were formed. In between the FIB impacted areas Ge island dimensions were increased in comparison with the ones from the Au rich spots surroundings. Increasing the scan number (from 1 to 6) causes the Ge islands to order and to decrease in size. Single Ge

island in between four FIB impacted areas was no longer formed (figure 4.3a) due to the Au amount and the increased surface roughness. Even so, we observed for all the scans a correlation between island positions and FIB impacted areas (see figure 4.3a). The increased Au amount (3 and 6 scans) reduced Ge diffusivity, and as consequence inside the FIB imaged areas, islands with smaller dimensions were formed.

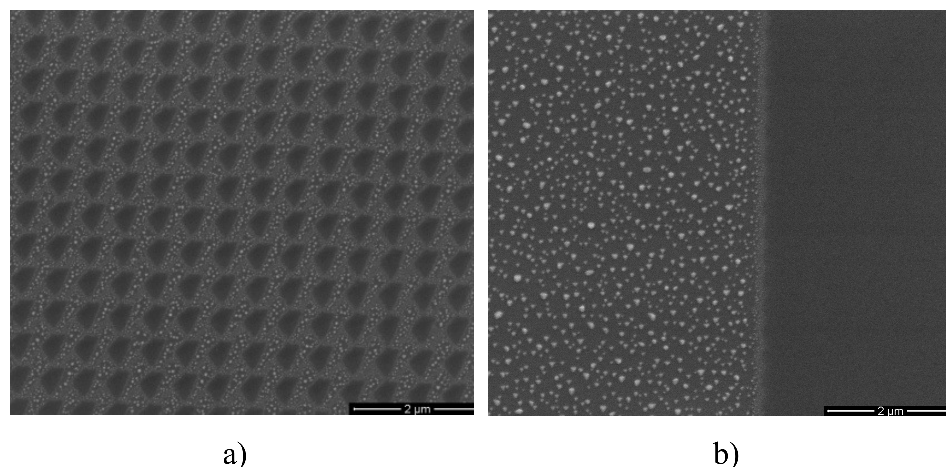

a) b)

Figure 4.3. *SEM images recorded for a Si(111) substrate FIB imaged using the ultra fast grabbing process (1024 pixels and 437.4 µs/pxl) with: a) 6 scans, b) 9 scans: left hand outside and right hand inside the FIB imaged area, after depositing 2 nm of Ge at 550ºC.*

Outside the imaged areas a standard 3D growth took place, Ge islands present both pyramidal and dome shapes (figure 4.3b – left hand). Comparing the Ge islands obtained on Au free areas with the ones formed inside the Au rich areas a reduction of their dimensions was observed with increasing scans number. For a number of scans equal to 9 (figure 4.3b – right hand) the nucleation of the Ge nanostructures was suppressed inside the FIB imaged area. The fact that no Ge islands grow anymore inside the FIB imaged areas was related to the Au amount and the changes in surface energy induced by its presence. The effect of the high Au amount (9 scans) was to increase the critical thickness, the transition from 2D to 3D was inhibited and no Ge islands nucleated.

Moreover, in order to prove the Au role on delaying island formation the deposited Ge amount was increased from 2 to 10 nm. A representative example for the Ge islands formation on top of 3 multiple scans (786 pixels) for 2 and 10 nm of deposited material is illustrated in figure 4.4. The 3D growth was confirmed by both techniques (AFM and SEM) used to image the samples surface. For high Ge amount (10 nm) the

islands were grown both in between and inside the FIB impacted areas. The effect of Au on delaying the 3D growth is proved by the formation of the Ge islands inside the FIB impacted regions. Comparing islands from the FIB impacted and in-between impacted areas a reduction of their dimensions and an increase in density were recorded due to the different Au amount in these two regions (see figure 4.4b). Due to the Au presence no islands coalescence was recorded for the Ge islands formed inside the FIB impacted areas. For some of the scans (e.g. figures 4.3 and 4.4) the FIB astigmatism directly influences the ion beam spot shape and as a consequence the impacted areas do not present a circular shape.

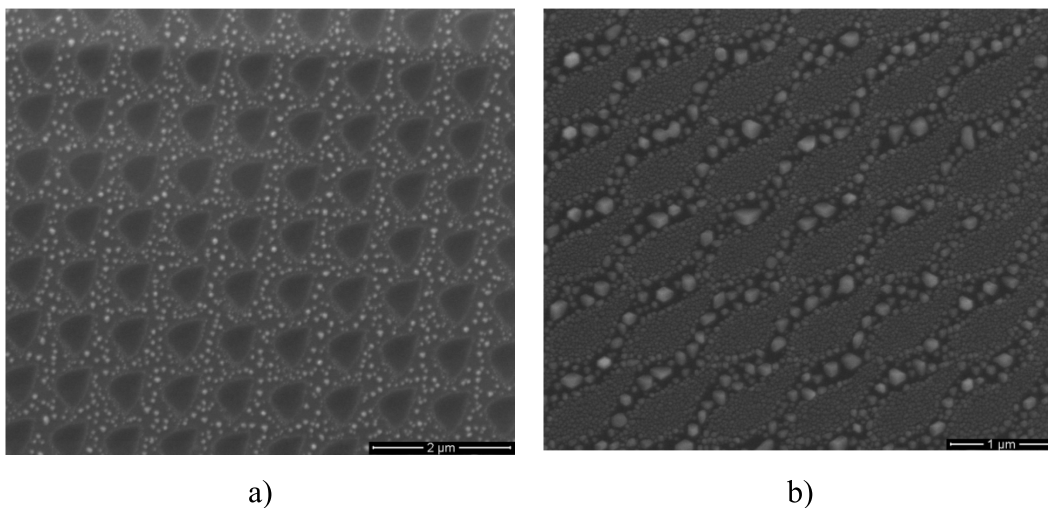

a) b)

Figure 4.4. *SEM images recorded for two patterns performed on a Si(111) substrate imaged with 3 multiple scans and 786 pixels: 2 nm (a) and 10 nm (b) of Ge were deposited at 550ºC.*

The influence of the annealing and growth temperature on the morphology of the Ge islands was also investigated. After performing two UHV annealing steps of the patterned substrates: i) 350ºC for 20 minutes and ii) 400ºC for 10 minutes, 10 nm of Ge were deposited by SS-MBE. For a low deposition temperature (400ºC) no Ge islands with standard shapes (huts, pyramids or domes) were obtained (figure 4.5a). The SEM images recorded for our sample revealed nanostructures with similar shapes as the ones reported for 3 nm Au layer [44] deposited on top of natural oxide. Since the same annealing temperature range was used for both samples (ours and the literature one), the annealing could be the responsible for the nanostructures shape. For the same patterning conditions

and a higher growth temperature (550ºC) Ge islands with standard shapes were formed inside the FIB imaged areas (figure 4.5b).

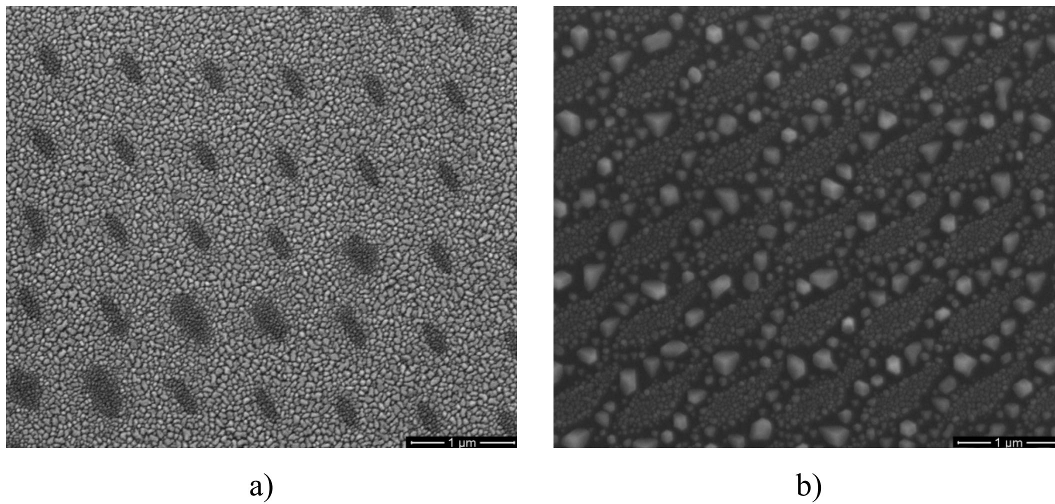

a) b)

Figure 4.5. *SEM views recorded for the two cases of annealing and growth conditions: (a) 10 nm of Ge deposited at 400ºC, after two annealings at 350ºC for 20 minutes, and at 400ºC for 10 minutes, and (b) 10 nm of Ge deposited at 550ºC after annealing at 550ºC for 15 minutes. Both Si(111) substrates were patterned in the same conditions: 512 pixels and 3 multiple scans. The same Ge growth rate was used for both samples.*

Moreover, for a growth temperature of 400ºC, the dimensions of the Ge nanostructures formed inside the FIB impacted areas were reduced in comparison with the rest of the FIB imaged area (for example see figure 4.5a - darker spots correspond to the FIB impacted areas). The same situation was recorded for all the FIB imaged squares using different numbers of pixels and multiple scans. When the number of scans was increased from 3 to 9 (higher Au amount) the same trend for the nanostructure dimensions was recorded. The Ge nanostructure size reduction was observed as a function of the Au presence and its amount, independently of the annealing and growth parameters. For 9 multiple scans and 1024 pixels it was impossible to distinguish the areas impacted by FIB inside the imaged square, but we grow Ge nanostructures with a base diameter between 10 and 60 nm as measured on the high resolution SEM image (see figure 4.6a). Figure 4.6b presents the AFM image performed far away from the FIB imaged areas, showing the formation of Ge nanostructures with bigger dimensions (between 65 and 120 nm) in absence of the Au ions and FIB imaging. At low growth

temperature (400ºC), nanostructures with similar shapes were obtained both inside and outside the FIB imaged regions. We can conclude that their shape has no correlation with the presence or the absence of the Au. On the other hand, Ge deposition on Au free Si substrates at this temperature induced the formation of Ge islands with standard shapes [45]. Responsible for the Ge nanostructures shapes at this growth temperature may be the annealing conditions, and the changes induced on the substrates morphology.

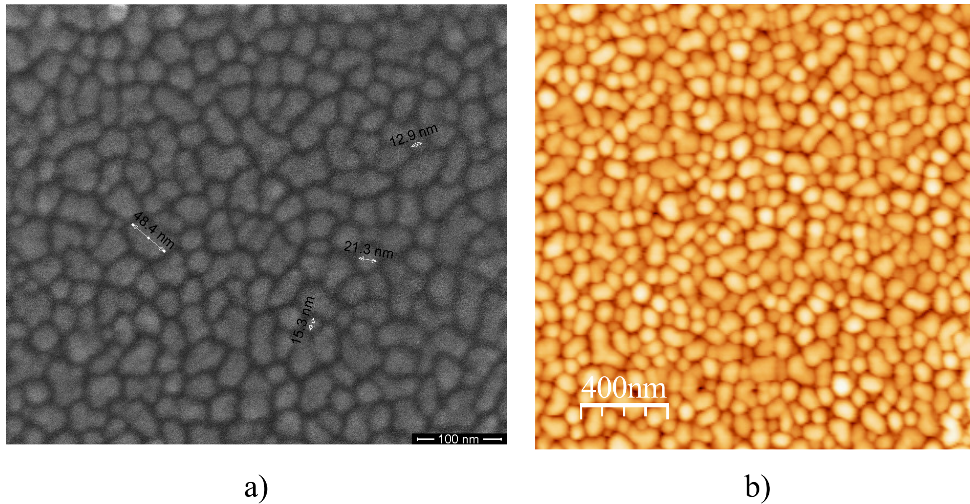

a) b)

Figure 4.6. *a) SEM view of a Si(111) substrate patterned with 1024 pixels and 9 scans (437.4 µs/pxl). b) AFM image recorded outside FIB imaged regions (Au free). The deposition temperature for the Ge amount (10 nm) was 400ºC.*

4.3.3 AuSi clusters formation inside the FIB imaged areas

The formation of the Au rich clusters inside the FIB imaged areas was investigated. Employed annealing temperature was increased in the 360-550ºC range, whereas the time was varied between 10 minutes and 2 hours. At the mentioned annealing temperatures, AuSi clusters formation was likely since they were above the Au-Si eutectic temperature (360ºC) [46]. The back scattering SEM explorations of the samples did not prove the presence of the Au ions or AuSi clusters formation inside the FIB imaged areas, not even for the largest scan time (437.4 µs/pxl) and 9 multiple scans. At

this point we believe that even inside the FIB impacted areas the existing Au amount was below the critical one (19%) for the formation of the AuSi clusters at eutectic point.

4.4 Ge nanostructures formation on hole-patterned Si substrates

In order to produce preferential nucleation sites and to increase the control of the nanostructures position within the surface, the Si substrates were FIB patterned with 2D hole arrays. By performing holes, an increased control of the exact positions at predetermined locations on the substrates was achieved, depending on the experimental needs. Hole`s aspect ratio was tailored by using different combinations of FIB parameters. Holes patterning approach offers a much better control of the Au amount and its location *only* inside the holes compared to the previous process (ultra fast grabbing). These benefits are assured by the increased number of FIB parameters that can be tailored within present process. Beside the holes aspect ratio, the Au amount induced significant changes in the growth mode of the Ge nanostructures, as will be seen later on. A detailed picture concerning substrates morphology evolution with various FIB parameters was achieved. The FIB patterned substrates were thermally treated employing different combinations of temperatures and times. Their evolution with the annealing conditions was examined. The AuSi clusters formation and distribution as a consequence of the ion doses and the thermal treatments performed was monitored. The influence of the different Au ion doses and surface morphology on the formation and the morphology of the Ge nanostructures was investigated.

4.4.1 Focused ion beam parameters influence on the Si substrates morphology

Si substrates were bombarded by Au^{2+} ions under various FIB exposure conditions to mill the hole arrays. To obtain the 2D periodic arrays of patterns two available scanning exposures: serial and parallel were employed. When the distance between the holes was reduced below 0.2 µm, much better results were obtained in the parallel mode (uniform hole dimensions and no hole coalescence).

We varied the ion fluxes in order to modify the balance between erosion and implantation. When reducing the ion flux from 4.09×10^{15} to 0.052×10^{15} ions/cm^2/s (source apertures are 50 and 20 µm, respectively) the morphology of the patterns

switched from holes to mounds. The AFM views of the patterned areas after FIB exposure under these conditions are presented in figure 4.7. We can clearly see the change of the patterns from holes to mounds from figure 4.7 a to b. A larger scale AFM image and a line profile (inset) of the border of the patterned area in the latter situation are presented in figure 4.7c. They both show that the surface level of the mounds is higher than those of the unpatterned substrate. This proves that mounds have been formed onto the surface due to a larger quantity of implanted ions as compared to the eroded matter under these experimental conditions. For a large range of FIB parameters using a source aperture of 20 µm only mounds were formed. However, holes could be formed for this aperture for a small probe current of 1pA.

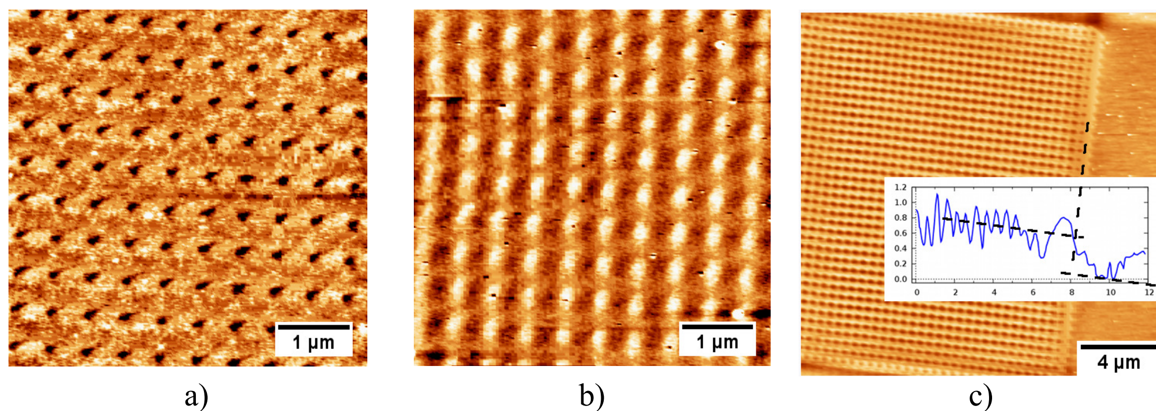

Figure 4.7. *AFM images of the patterns obtained under different FIB irradiation conditions. The source aperture was varied between: a) 50 µm and b) 20 µm. In (c) a larger scale image is presented, revealing the outgrowth over the patterned area.*

Moreover, even for a 50 µm aperture, using a fixed ion dose and increasing only the distance between the holes it was possible to pass from milling holes to form mounds. This transition from holes to mounds using the same FIB patterning conditions is illustrated in figure 4.8a and b. The presence of the mounds on the substrates surface was confirmed by performing AFM measurements on different configurations (the sample was rotated 45º and 90º toward initial position). The only parameter changed between the different patterned squares was the distance between the intended “holes”, which was increased from 0.2 µm with a 0.1 µm step to 1 µm. For a distance up to 0.5 µm we obtained holes with a depth of 2 nm (figure 4.8a), whereas above 0.6 µm only mounds (figure 4.8b) were formed. There was no correlation between the mounds aspect ratio and

the increased inter holes distance. All the mounds present the same characteristics: an average height around 1.3 nm and a base diameter around 500 nm. This is consistent with the fact that the same ion dose was used to perform the different patterns. Compared to the hole diameter which was around 350 nm, the mounds were broader, the implanted ions stayed closer to the surface and no material was removed. The distance between two mounds corresponds well to the intended distance between the patterned features as set on the FIB control software.

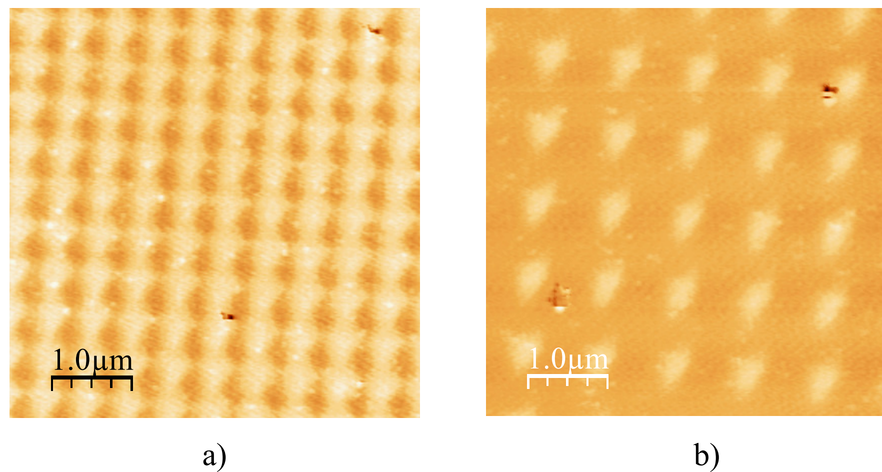

Figure 4.8. *AFM images corresponding to an ion dose of 18.2x10^{-4} C/cm^{2} for different distance between the features: a) 0.5 µm (holes) and b) 1 µm (mounds).*

In fact, for inter hole distances below 0.2 µm no patterns were obtained; only a square (5x5 µm^2) was milled. This is because of the Au ion large size combined with the ion beam size. Measured square depth was 110 nm for a distance of 0.1 µm between the holes, while for 0.07 µm it was significantly increased (225 nm). The AFM image recorded for one of the milled squares and its profile are shown in figure 4.9. Actually, after changing the AuSi source to a Ga^+ one for the same distance (0.07 µm), both hole diameter and distance between the holes were reduced to ~ 35 nm and 70 nm, respectively, without milling a square. From this point of view much better results concerning hole dimensions reduction were obtained using FIB with Ga^+ ions, but on the other hand the Ga presence was not wanted due to its influence on the nanostructures growth mode and because one of the objectives was to investigate Au ions influence on Ge nanostructure growth mode and morphology.

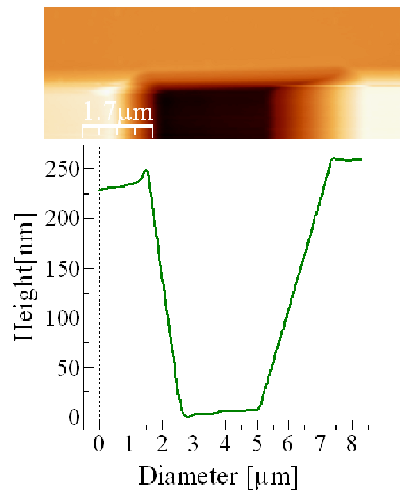

Figure 4.9. *AFM image recorded for a FIB milled square obtained as a result of reducing the intended distance between the holes to 0.07 µm. Square profile is presented in the bottom part of the figure.*

Afterwards, in these two regimes (mounds and holes) we investigated the morphological evolution of the patterns with two different source apertures.

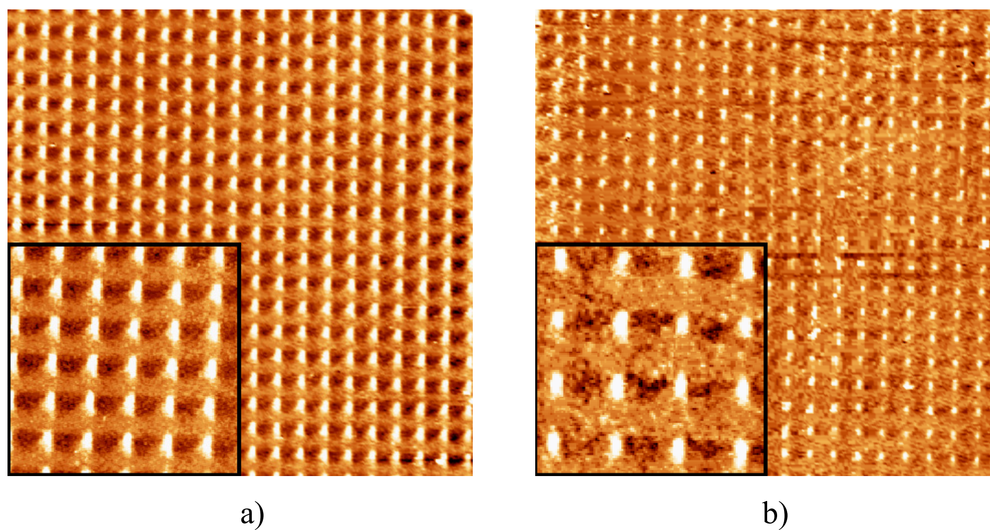

Figure 4.10. *AFM images of mounds formed during FIB experiments at 20 µm source aperture, using beam sizes corresponding to a focused spot size of (a) 40 and (b) 20 nm. Scan size for (a) and (b) images is 10 µm, and their insets are enlarged regions of 3 µm (a) and 2 µm (b), respectively.*

In the regime of mound formation (using 20 μm source aperture), we observed that the size of the mounds can be tuned by varying the ion beam intensity which depends on the focused spot size, as illustrated in figure 4.10. The AFM images show different mounds formed for the two values of the beam size corresponding to a spot size of Ø = 40 and 20 nm (figure 4.10a and 4.10b, respectively). The dependence of the mound dimensions with the beam profile follows directly from a geometrical effect, i.e. larger beam sizes result in larger dimensions of the mounds. Finally, no mound formation was observed for a beam size of 10 nm. In this regime, the exposure time is insufficient for milling.

The ion beam size is proportional to the spot size Ø and thus we observed a linear increase of the mean diameter of the mounds with ion spot size (figure 4.11a), which can be directly related to an increasing ratio between the eroded matter over the implanted ions. Using the 20 μm source aperture and a fixed spot size of 50 nm, the mound evolution with different ion doses was investigated (figure 4.11b). For a probe current of 66 pA, the time for 1 hole was varied between 0.13 ms and 2.53 ms (ion dose: 1.48 x $10^{15}/cm^2$). Employing the ion dose corresponding to the lowest time (0.13 ms) no holes were milled or mounds formed, in consequence, no point is drawn on the graph (figure 4.11b). No changes in mound base diameter (average value 300 nm) were recorded for the spot size of 50 nm, while the mound height was slightly enlarged with the ion doses (figure 4.11b).

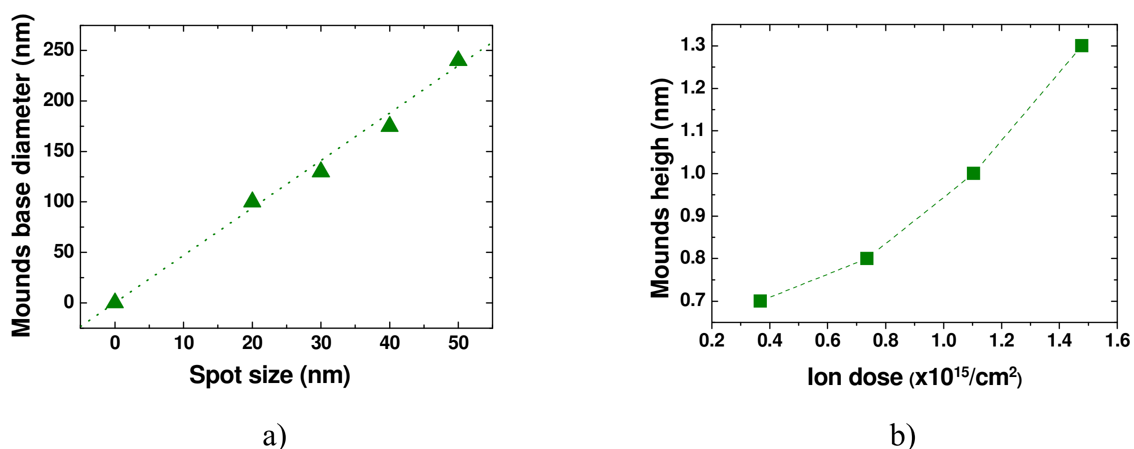

Figure 4.11. *Evolution of the mound dimensions with: the beam size (a), and the ion dose (b). The lines are guides to the eye.*

At higher ion beam intensities and at the conditions of hole formation (using 50 μm source aperture, see figure 4.12a), we also investigated the morphological evolution of the holes with the exposure. In order to calculate the ion dose, we needed the time used to perform one hole and the hole radius measured from the AFM images. In this particular case, the ion dose was increased by modifying the hole depth asked to the FIB control software to perform the patterns, while the spot size remained fixed at 50 nm and the probe current set at 55 pA. The combination of these FIB parameters increased the milling time for one hole from 15.3 ms to 194.6 ms. A linear increase of the hole aspect ratio with ion dose was observed, corresponding to a linear increase of the depth at a constant lateral diameter (see figure 4.12b).

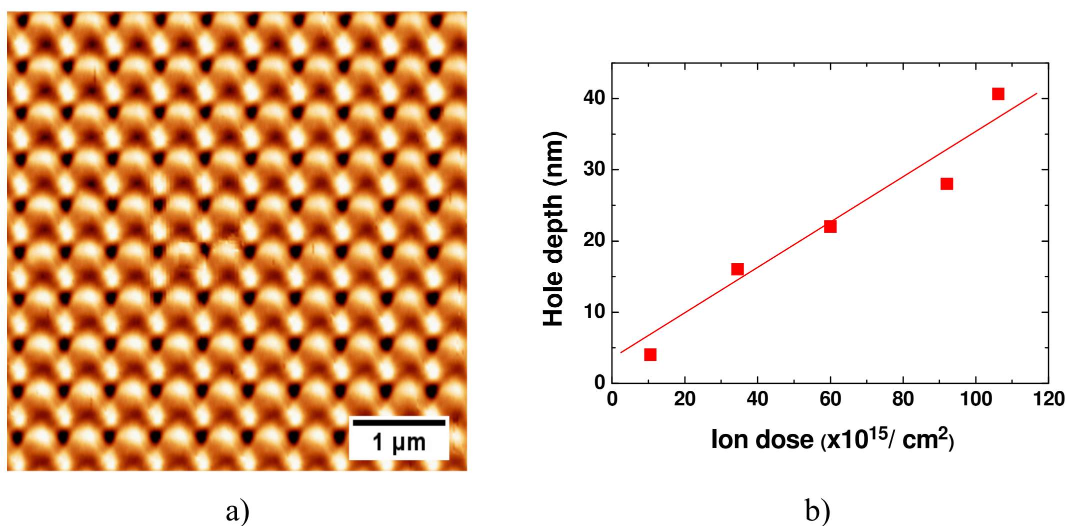

Figure 4.12. *a) AFM image of a hole pattern formed during FIB experiments. The graph (b) presents the hole depth as a function of the ion dose.*

Preserving the same FIB parameters, the evolution of the hole aspect ratio with the probe current was inspected. The probe current was varied between 66 pA and 1 pA and the time to mill one hole was increased from 1.26 ms to 83.33 ms. By decreasing the probe current from 26 pA to 1 pA it was possible to reduce the hole diameter from 330 nm to 200 nm, while the depth was increased from 1 nm to 45 nm (see figure 4.13). For larger values of the probe current (46 and 66 pA) combined with the rest of the FIB parameters no holes were milled, but the FIB patterned squares could be identified by the AFM measurements. In order to obtain holes with a reduced diameter, a small probe

current has to be used, of course combined with the other parameters that act in the same direction.

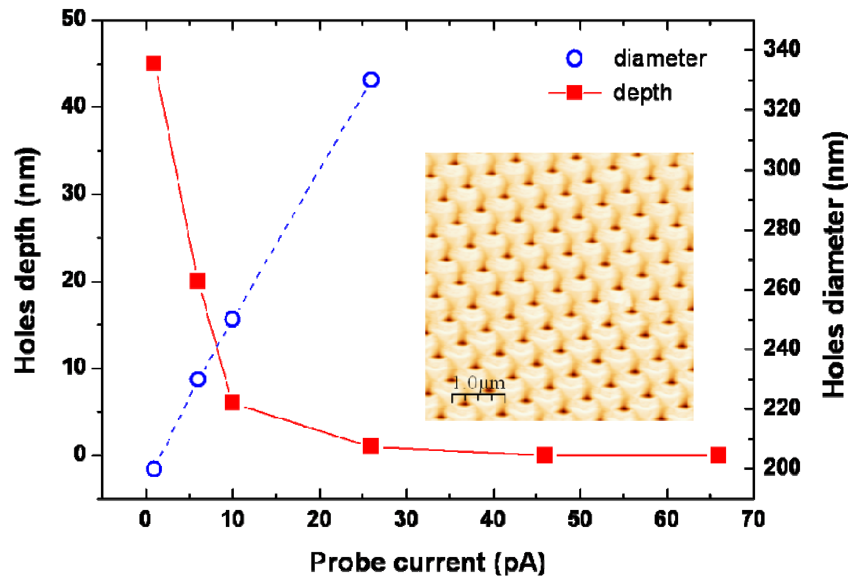

Figure 4.13. *Evolution of the hole dimensions with the employed probe current. The graph inset presents the AFM image recorded for a pattern performed with a probe current of 1 pA.*

The focus and the astigmatism proved to be very critical and as a consequence they influenced a lot the morphology of the resulting patterns in terms of shapes (circular to elongated ones) and hole dimensions (depth and lateral diameter). The AFM image recorded for a pattern performed using “the best” focus (judging by the FIB views) is showed in figure 4.14b (FIB objective voltage 16.53 kV). A defocus was introduced decreasing (16.43 kV) and increasing (16.63 kV) the FIB objective voltage (see figure 4.14 a and c, respectively). The hole profiles (figure 4.14 - insets of the AFM images) revealed the modifications on the hole dimensions with defocus. For “the best” focus the holes present a depth of 3.5 nm and a diameter of 180 nm in one direction and more than double (400 nm) in the other one. Focus adjustments induced a decrease in the hole depth to 2 (figure 4.14a) and 1.5 nm (figure 4.14c), while the diameter was almost constant (~ 380 nm) in both cases. Even if the FIB views revealed holes with circular shapes, after milling a different shape was obtained (figure 4.14b). The astigmatism was not changed between the three patterns, but as it can be seen in figure 4.14 the holes do not present a circular shape, but a more elliptical one. Handling both focus and astigmatism has to be

done carefully in order to obtain the finest results in terms of holes shape and dimensions. On the other hand, slightly defocusing is another useful tool to control the dimensions of the holes.

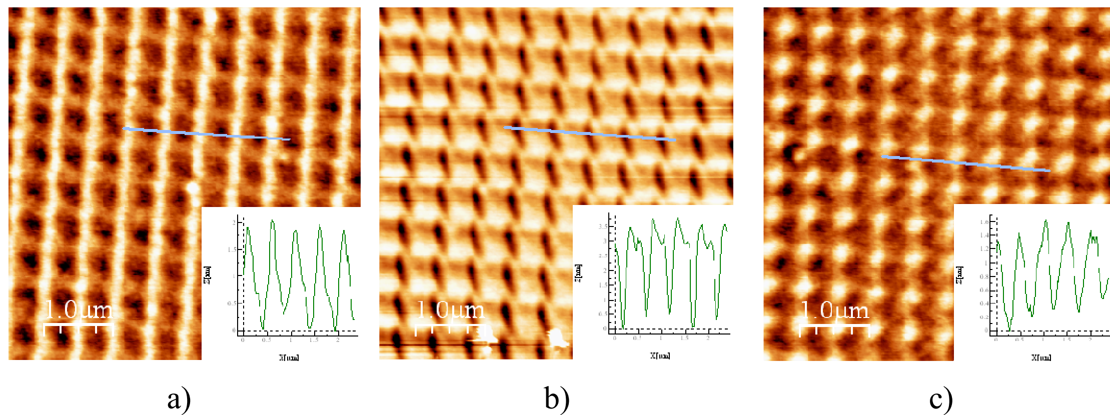

Figure 4.14. *Influence of the FIB objective voltage on the hole dimensions: a) 16.43 kV, b) 16.53 kV ("best focus"), and c) 16.63 kV.*

All the FIB parameters, as showed, played an important part on tailoring patterns aspect ratio. Both, mounds and holes formation and their evolution with the different FIB parameters were investigated. The patterned arrays were performed using combinations of the above mentioned FIB parameters, in order to reduce the hole diameters, while their depth was adjusted to the specific experimental needs. A much better control of the Au amount and its position within Si substrates was achieved using the FIB holes nanopatterning compared to the FIB grabbing process.

4.4.2 Influence of the annealing conditions on the evolution of Si patterned substrates morphology

In the last years, thermal treatments were performed on patterned Si substrates and their influence on hole shape transformation was widely studied. Although many mechanisms can make relevant contributions (e.g. bulk diffusion), at nanoscale the surface diffusion is the most important mass-transport process [47]. High temperature (~1000°C) hydrogen annealings were used on patterned Si substrates to improve their roughness [48], to round trench corners [49, 50], and to obtain the desired topologies [49, 51]. These results were interpreted using the continuous theory of the surface diffusion [47, 51]. The existence of a metal (Au) on top of the annealed surfaces modifies, beside the surface free energy of various types of planes, the step free energy and the step-step interaction. On the one hand, Au presence may additionally affect the diffusion and the mobility of the Si adatoms [52]. On the other hand, the Au layer evolution with annealing was investigated in order to form the AuSi clusters, which will serve as nucleation centers for the growth of the nanowires [44, 53].

The annealing temperatures and times were mapped out to investigate their influence on the FIB patterned Si substrates with both (111) and (001) crystallographic orientations. More details about the annealing time and temperature employed in this experiment can be found in section 4.1. Features evolution with annealing is extremely important since the Ge nanostructures growth turns to be highly dependent on the substrate detailed morphology. The annealing influence on the formation and morphology of the AuSi crystalline clusters was studied in the two cases reported above when patterns consist of mounds or holes. For the formation of the Au rich clusters this annealing step requires first a large quantity of Au locally implanted near the patterns and secondly the segregation/diffusion of Au into crystalline clusters. After performing the annealing step the samples were cooled down at room temperature and the surface topography evolution was observed by AFM and SEM.

4.4.2.1 Evolution of the Si patterned substrates morphology with the annealing conditions

Mounds annealing

For the samples patterned with mounds, irrespective of the annealing conditions, we systematically observed total flattening and mounds disappearance after performing annealings. In this situation it was not possible to detect any formation of AuSi clusters by none of the techniques used. We attributed this behavior to an extremely low concentration of gold in these "soft" sputtering conditions.

Holes annealing

In the case of the samples patterned with holes, we observed different evolutions depending on the annealing temperature (T_A). The temperature range was divided into three groups as follows: $T_A \leq 450ºC$ (case A), $450ºC < T_A < 650ºC$ (case B), and $T_A \geq 650ºC$ (case C). Independently of the applied annealing times (15-40 minutes) at low temperatures (case A) the patterns suffer no changes for both Si substrate orientations. The AFM images recorded before and after the annealing steps for 35 minutes at 450ºC, and the corresponding hole profiles are shown in figure 4.15. For the Si(111) case the ion dose used to pattern was 2.3×10^{-4} C/cm^2, and the measured hole depth results less than 1 nm (~ 0.8 nm). After performing the annealings, the hole depth and diameter remained basically unchanged (see profiles - figure 4.15 c and d). The same behavior was observed independently of the annealing times and for all the investigated temperatures in case A.

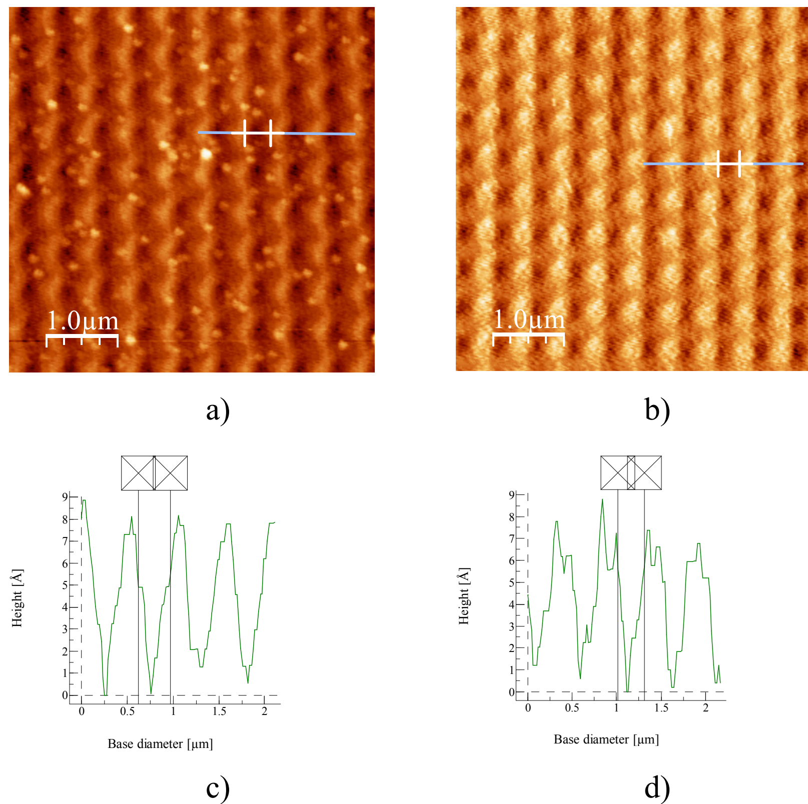

Figure 4.15. ***Case A.*** *Annealing performed on a Si(111) substrate patterned with holes. The AFM images recorded: before annealing (a) and after annealing at 450ºC for 35 minutes (b). The AFM profiles of the holes before (c) and after annealing step (d) are shown.*

In the *450-650ºC* (case B) intermediate temperature interval, the evolution of the surface morphology was followed as a function of annealing time and hole depth. We divided the depth intervals in three collections in this manner: below 4 nm (case B I), between 4 and 8 nm (case B II), and above 8 nm (case B III), according to their evolution with the thermal treatments performed. The holes presenting a depth situated in the case B I, when performed on Si(111) or Si(001) substrates, are reducing both the depth and the diameter with annealing, as demonstrated in figure 4.16. Stronger influence on hole dimensions were recorded in the first annealing step, while after the second step they change less. For a starting depth of 1 nm after performing the second annealing step (35 minutes) no holes were found, only a flattened surface. The reduction of the hole diameter (or even hole disappearance) may suggest that the recrystallization takes place from the edge to the center. This evolution is consistent with previously published results [47, 49, 54] regarding hole behavior with annealing.

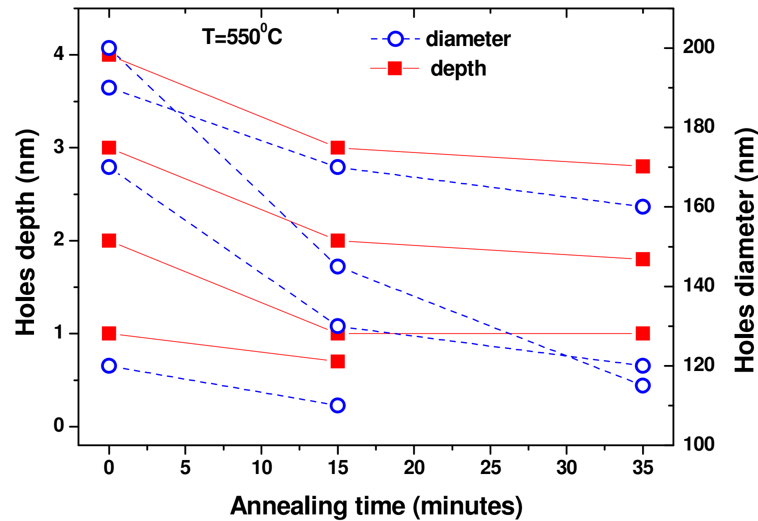

Figure 4.16. ***Case B I.*** *Hole depth and diameter evolution with annealing time. On the patterned Si(111) oriented substrates we performed two consecutive annealings at 550ºC for 15 and 20 minutes, respectively. The lines are guides to the eye. Blue circles symbolize lateral diameter, while red squares stand for hole depth.*

Employing a fixed ion dose of $6.8x10^{-4}$ C/cm^2, the distance between the holes was varied between 0.2 and 1 µm. The two cumulative annealing steps for 15 and 20 minutes were performed at 550ºC. All the patterns were thermally treated in identical way. The AFM images of the selected patterns with distances between the holes of 0.5 and 0.7 µm and their evolution with annealing time are shown in figure 4.17. At the starting point, before any treatment, both patterns present holes with a depth of ~ 4 nm and a diameter of ~ 200 nm. After performing the second annealing step both arrays of holes have the same depth (~ 3 nm) and diameter (~ 140 nm) (see figure 4.17). Irrespective of the distances between the holes the same behavior was observed for the hole dimensions with each annealing step. For the studied depth interval (B I), no changes that could be correlated with the distance between the holes were evidenced.

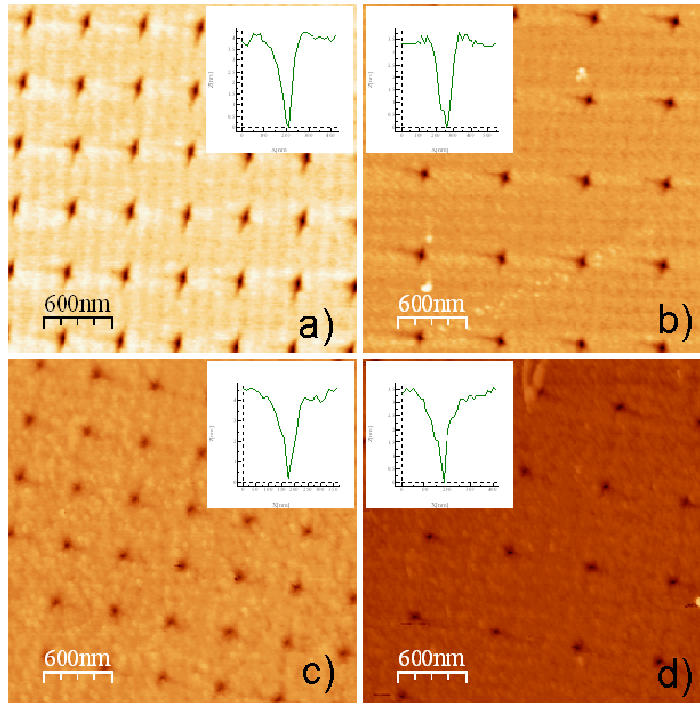

Figure 4.17. *AFM images and hole profiles (insets) recorded before any treatments for two patterns with the distance between the holes of 0.5 μm (a) and 0.7 μm (b). The AFM images (c and d) and corresponding hole profiles (insets) presents the same patterns after two consecutive thermal treatments at 550°C for a total time of 35 minutes.*

For the case of holes with larger depths, situated in the second interval - B II (depth between 4 and 8 nm) depending on the Si substrate orientation a different behavior was observed. For Si(001) the hole depth and diameter increased with annealing (see figure 4.18). The hole depth is increased with the thermal treatments in one case 3 times (from 5 to 15 nm - figure 4.18 from a to c), while in the second case 5 times (from 6 to 30 nm - figure 4.18 from b to d). The different behavior of the hole dimensions may be caused by the differences in the hole initial depths and the ion doses used to mill the holes.

In addition, our observations proved that hole evolution is independent of the neighboring holes. This information was confirmed by analyzing and comparing the holes located at three different positions within the patterns: pattern center, border and corner. Investigated holes present eight, five and three neighbors, respectively, and the same behavior was found for all, independent of their location. The increase of the hole

diameter is in agreement with the reported data for hydrogen annealing performed on holes patterned Si substrates [51].

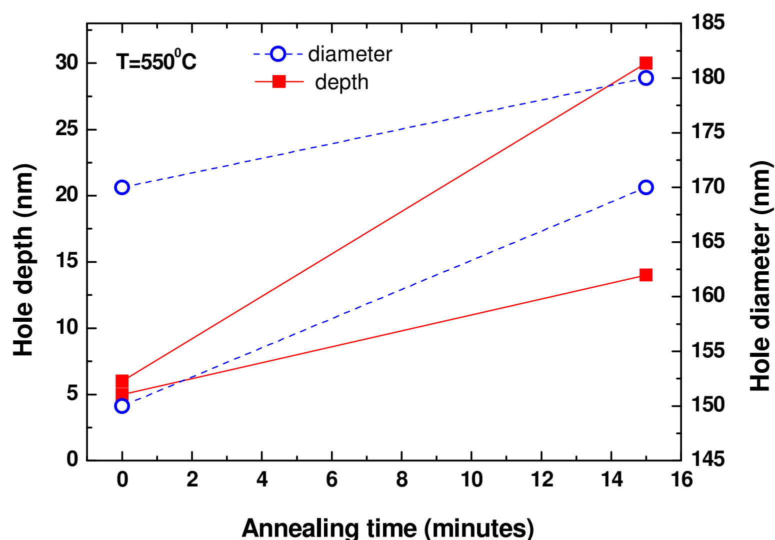

Figure 4.18. ***Case B II.*** *Hole depth (4-8 nm) and diameter evolution with the annealing time. The holes performed on a Si(001) substrate were annealed at 550ºC for 15 minutes. The lines are guides to the eye.*

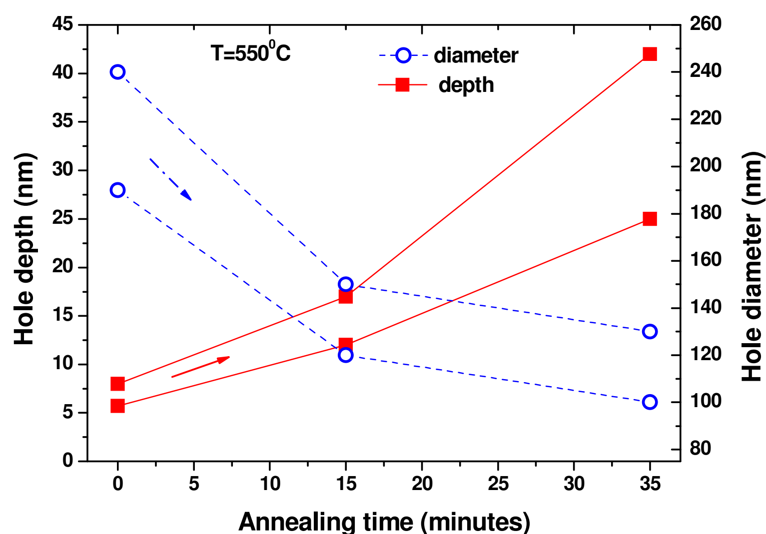

Figure 4.19. ***Case B II.*** *Hole depth (4-8 nm) and diameter evolution with annealing time. Two consecutive annealings at 550ºC for 15 and 20 minutes were performed on the Si(111) patterned substrate. The lines are guides to the eye.*

Compared to the (001) orientation an opposite behavior was observed for the hole diameter when they were performed on the Si(111) substrates and thermally treated. The holes that present a different diameter behavior, decreasing their values, were performed with a distance of 0.6 and 1 μm between them. The hole depth is shifted to larger values, similar to the behavior of the holes performed on the Si(001) substrates (see figure 4.19). For the case of the Si(111) crystallographic orientation the behavior of the hole diameter can be assigned to the different ion doses.

The AFM images recorded before and after carrying out the two thermal treatments on the hole array performed on a Si(111) substrate with a distance between the holes of 1 μm are presented in figure 4.20 a, b and c. The corresponding hole profiles measured on the AFM images for initial, after the first annealing step (15 minutes) and the second one (35 minutes), are shown in figure 4.20 d, e, and f, respectively.

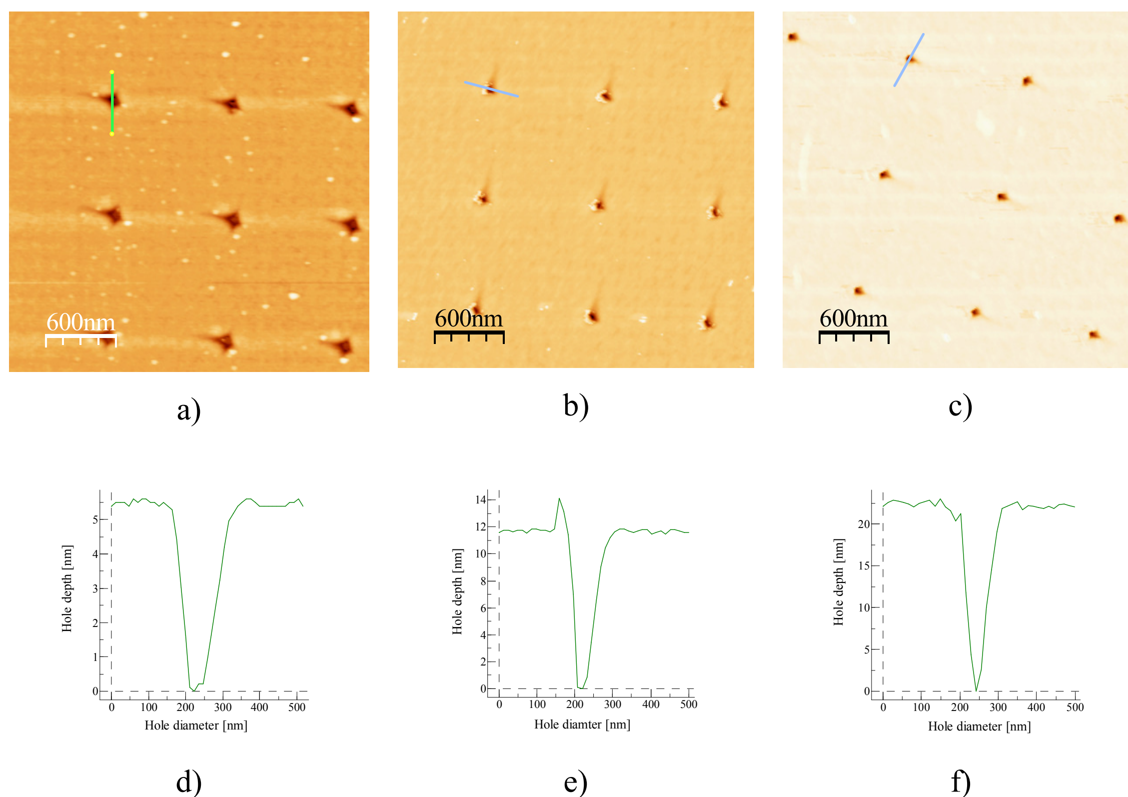

Figure 4.20. ***Case B II.*** *AFM images for holes with an initial depth 5.5 nm and base diameter 190 nm performed on a Si(111) substrate: as performed (a), and its evolution with annealing time: 15 minutes (b) and 35 minutes (c). Corresponding hole profiles are revealed in d, e, and f, respectively. The annealing treatments were performed at 550ºC.*

After the first annealing at 550ºC for 15 minutes the hole depth was more than double, while their diameter was reduced with an average values of 70 nm (see figure 4.20e). The second cumulative annealing (550ºC) for another 20 minutes led to an increase of the hole depth of almost 4 times and a decrease of 90 nm in the hole diameter (see figure 4.20f), as compared to their initial dimensions. The aspect ratio (AR) (the hole depth divided by the base diameter) was increased from 0.03 to 0.1 after the first annealing step. The holes performed on the Si(111) substrate after the second cumulative annealing present an aspect ratio of more than double (0.25) than after the first step. For the holes performed on Si(001) the same tendency with the annealing was observed, an increase of the aspect ratio from 0.03 to 0.07 was recorded. The gradual increase of the holes AR with the annealing time is opposite to what was reported for the holes annealed in hydrogen atmosphere, where a reduction took place [51].

Furthermore, employing the same annealing conditions for the initial hole depths ranged from 9 to 50 nm (B III) and the average lateral diameters between 150 and 250 nm, both depth and diameter are increased, but not in the same proportion for all the patterns. Hole depth was doubled in some cases, and increased up to 10 times compared to the initial values (from 10 nm before to 110 nm after the annealing steps) in other cases (see figure 4.21). With annealing treatments the lateral diameters suffer less change compared to the depth, increasing with values between 20 and 80 nm.

On the contrary, to the report data for hydrogen atmosphere annealing [50, 51], in UHV the holes are not closed with consecutives annealings. The so called "bottle" effect (holes profiles after performing the thermal treatment follow the shape of a bottle and tend to close) was reported for holes annealed in H atmosphere [51]. This effect was not observed for any of the patterns obtained independently of the employed FIB parameters for Si substrates patterning and UHV annealing conditions.

For the high annealing temperatures range (*650-850ºC*: case C), the patterns with small hole depths (below 3 nm) disappeared and a flat surface was obtained. The AFM measurements showed no topography that could be associated with the initially existing holes. The recovered flattened surface and the hole disappearance for this temperature interval are in good agreement with the reported results [11]. As expected, the rate at which the recrystallization takes place is a function of the annealing temperature. The holes that presented larger depths (> 3nm) were not annealed in the *650-850ºC* range, so no data are available.

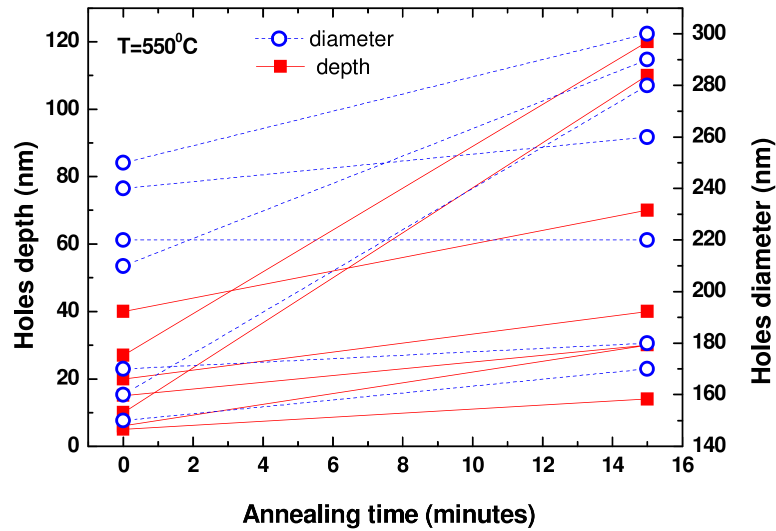

Figure 4.21. ***Case B III.*** *Large (9-50 nm) hole depth and diameter evolution with annealing time. The holes were performed on a Si(001) substrate and annealed for 15 minutes at 550ºC. The lines are guides to the eye.*

In figure 4.22 the evolution of the hole dimensions (depth and diameter) with the annealing temperatures is presented. The examination of the substrate topographies for fixed annealing temperature and time revealed its dependence on the ion dose used for patterning of the Si substrates with different crystallographic orientations (figure 4.22 - case B).

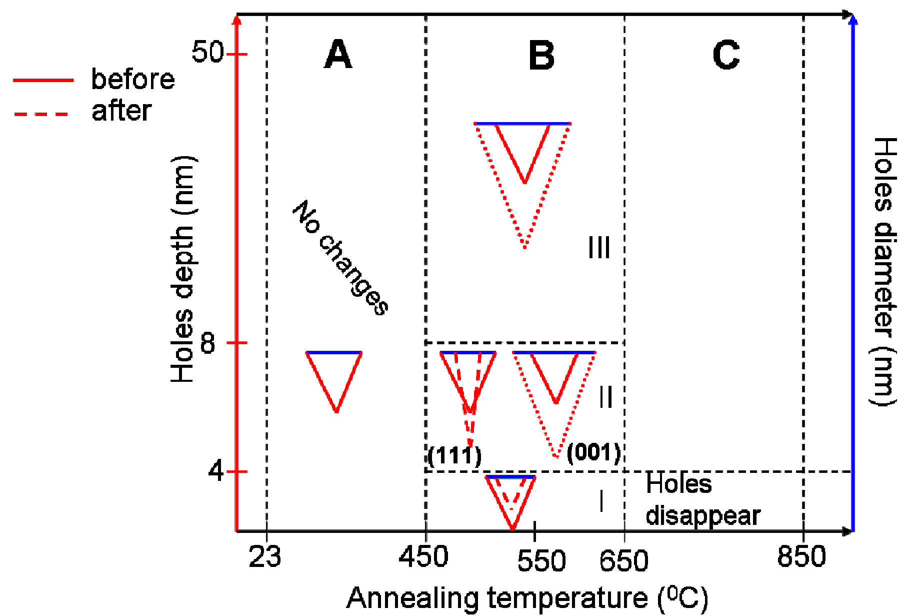

Figure 4.22. *Summary of the evolution of the hole dimensions (depth and diameter) with the annealing temperatures. The straight line represents hole dimensions before the annealing steps and the dashed and dotted ones the changes induced by the annealings. The three analyzed temperature ranges are symbolized by A, B and C. The colors code is associated with the hole depth (red) and diameter (blue).*

4.4.2.2 AuSi clusters formation inside patterned Si substrates

The Au rich clusters formed as a consequence of the thermal treatments will serve to promote the Ge nanowires growth. For this reason the conditions (time and temperature) employed during the annealing steps are crucial. Besides the annealing and the growth conditions, the dimensions of the Au rich clusters are playing an important part in the nanowire growth. As demonstrated in the literature [55], not all the AuSi clusters formed serve as nucleation centers. Hence, ion doses from a large spectrum ($1x10^{-4}$ - $240x10^{-4}$ C/cm^2) were used to tailor the size and density of the AuSi clusters. All the obtained patterns were thermally treated in a large temperature interval (300-850°C), as extensively detailed in the previous subsection. As a consequence of the annealing treatments, we expected to form AuSi clusters inside patterned areas, at least in the range of temperatures above the AuSi eutectic point (360°C) [46].

For $T_A \leq 450°C$, since the patterns remained unchanged and independent of the Au ion doses, no visible formation of clusters was detected. Based on the hole evolution with the annealing temperatures the most promising range is the intermediate one: *450°C - 650°C*. The formation of the Au rich clusters was followed as a function of the thermal treatments and the ion doses used to pattern the Si substrates. However, it was difficult and sometimes even impossible to detect the formation of the AuSi clusters, especially because their presence depends on the implanted ion doses. Even so, the Au existence and its influence on the nanostructure growth cannot be neglected, as will be seen later on. For the small ion doses (below 44 x 10^{-4} C/cm^2) the HR-SEM images did not evidence the Au presence or the AuSi clusters formation with the annealings – images not showed. For an ion dose (50 x 10^{-4} C/cm^2) situated in the lowest part of the intermediate ion dose (ranged between 44 x 10^{-4} and 108 x 10^{-4} C/cm^2) the HR-SEM image recorded in back scattering conditions showed the formation of the AuSi clusters inside the holes (see figure 4.23). Imaging the sample with AFM it was not possible to detect the presence of these AuSi clusters inside the holes.

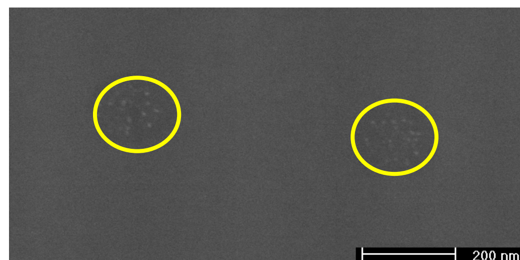

Figure 4.23. *High resolution BS-SEM image show AuSi cluster presence inside the holes. The ion dose employed to perform the pattern was 50 x 10^{-4} C/cm^2. The patterned substrate was annealed at 550ºC for 35 minutes. By yellow circles are marked the holes.*

By increasing more the ion dose, the formation of the Au rich clusters was evidenced for the 450-650ºC annealing range. A large scale image of pattern morphology after two successive annealings is presented in figure 4.24a. The AFM images of the patterns reveal the formation of a large number of small clusters in the FIB holes and their surroundings (figure 4.24b). Recorded back-scattering scanning electron images (BS-SEM) confirm the presence and the formation of the Au rich clusters (figure 4.24c) inside patterned areas. We observe an increase of the lateral distribution and density of the

clusters with the ion beam intensity (I_{Au}): the larger is I_{Au}, the broader is the lateral cluster distribution and the larger is the density (an example of this evolution is presented in figures 4.24 b and c, where I_{Au} was varied between 0.0352 and 0.1747 A/cm^2). Cluster formation in between the holes is probably due to the Au large diffusivity on Si substrates (Au is highly mobile at annealing temperature) [56, 57].

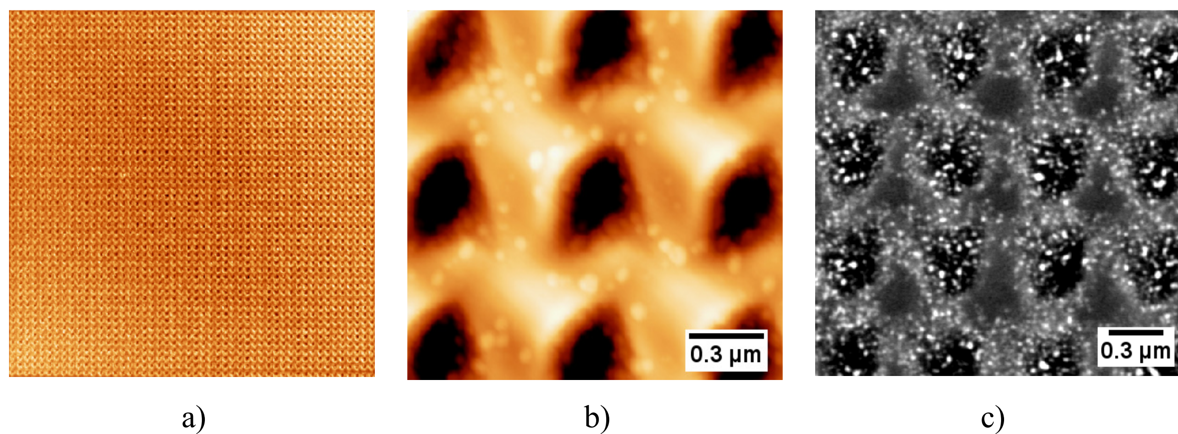

Figure 4.24. *a) Large scale AFM image of a patterned area after two successive annealings at 550°C (20 μm scan); b) AFM image of the clusters formed around the patterns at I_{Au} = 0.0352 A/cm^2; c) BS-SEM image evidences the presence of Au in the clusters. Here light areas correspond to Au rich clusters formed at I_{Au} = 0.1747 A/cm^2.*

Recorded AFM images allowed measuring the dimensions of the AuSi clusters formed during the annealing steps. AuSi droplets with heights between 4 and 18 nm and base diameters ranging from 50 to 130 nm were formed inside the patterned areas after performing two consecutive annealing steps. There is no correlation between the Au rich clusters height and their base diameter.

Using higher ion doses to pattern the Si substrates the formation of the Au rich clusters was also evidenced. Their dimensions could be increased by reducing the distance between the holes.

4.4.3 Growth of Ge nanostructures on hole patterned Si substrates as a function of the ion dose

The Si substrates were patterned with holes to achieve the nucleation of the pattern ordered Ge nanostructures with a high density ($10^{11}/cm^2$). The ion dose (ID) interval employed was divided in three main ranges namely: low ion dose (ID < $44x10^{-4}$ C/cm^2), intermediate ion dose ($44x10^{-4}$ C/cm^2 < ID < $108x10^{-4}$ C/cm^2), and high ion dose ($108x10^{-4}$ C/cm^2 < ID < $240x10^{-4}$ C/cm^2). The influence of the different ion doses on the obtained Ge nanostructures morphology and growth mode was investigated.

4.4.3.1 Low ion dose

Growth of self assembled Ge islands on Si(111) patterned substrates

On Si substrates with (111) crystallographic orientation were performed 2D arrays of holes under various FIB exposure conditions. After Ge deposition (5 nm with a growth rate of ~$9x10^{-2}$ nm/s), the patterned areas can be easily distinguished from the nonpatterned ones. The boundary and the differences between the patterned and nonpatterned regions can be clearly seen in both SEM and AFM images illustrated in figures 4.25 a and b. The array extent is defined by the FIB pattern. The morphology of the islands formed in both regions was carefully analyzed by performing AFM measurements.

The nonpatterned areas present a random distribution of the Ge islands, easily comparable to the large amount of works reported for the Ge growth on Si(111) substrates [58, 59]. These 3D nanostructures present pyramid and dome shapes [60]. The Ge island height from nonpatterned areas ranges between 10 and 70 nm, with large base diameters between 200 and 430 nm.

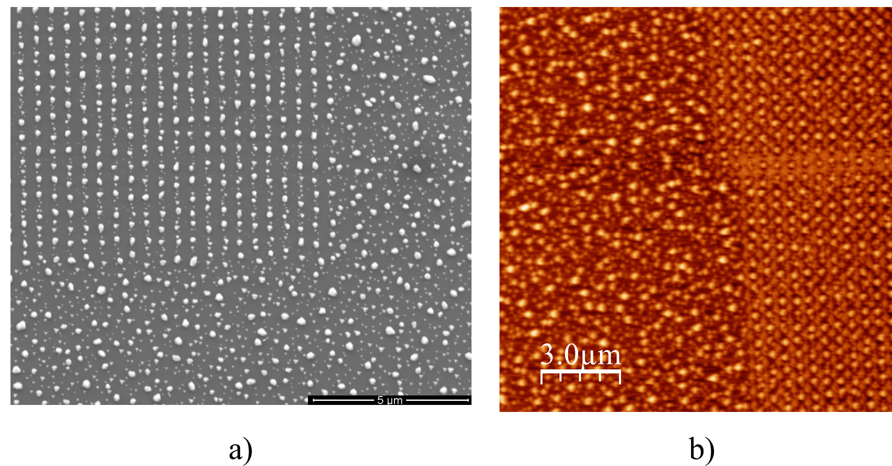

Figure 4.25. *a) SEM image of nonpatterned and patterned with holes areas – upper left corner. The Ge islands appear as white dots. b) AFM image for the nonpatterned (left) and patterned areas (right). Both views (SEM and AFM) exemplify a pattern with hole depth of 1 nm and 0.5 µm pitch. In the particular case presented in figure 4.25 – hole depth was 1 nm.*

Inside the patterned area, dome shaped islands were obtained. These uniform islands present an average height of 60 nm and a base diameter around 380 nm. In addition, pyramidal shaped islands with smaller dimensions were also found in the patterned areas. These islands have an average height of 35 nm and a mean base diameter of 250 nm. More details about the island dimensions formed both inside and outside patterned regions can be found in figure 4.26. Whereas outside patterned areas the aspect ratio (AR) varies for pyramids from 0.03 to 0.11 and for domes between 0.15 and 0.18, inside the pattern the small islands present an AR of 0.1-0.12 (pyramids) and the big islands of 0.15 (domes).

Compared to the literature data reported on FIB patterned Si substrates [10, 16], where the Ga ions were removed using a specific cleaning method, in our case the Au ions are present inside the holes and in a smaller amount even in between them. So, beside pattern morphology influence, the Au presence has to be taken into account when the Ge nanostructures are analyzed.

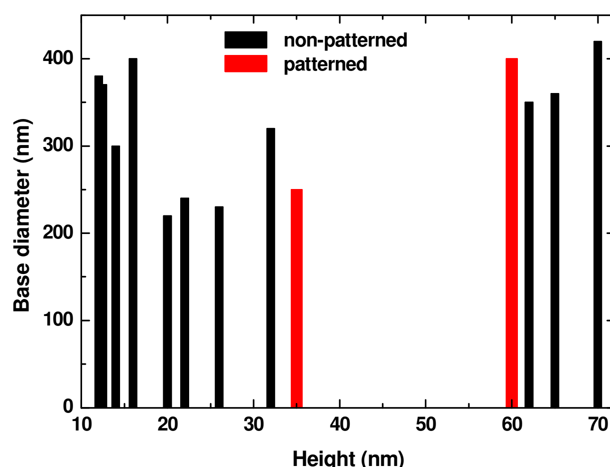

Figure 4.26. *Ge islans base diameter and height for patterned (red) and non-patterned (black) areas. Both pyramidal and dome shaped islands were found inside and outside the patterned squares. More uniform Ge islands were formed inside the area patterned with holes of 1 nm depth.*

A tendency of the Ge islands to grow on the flat surfaces between the FIB holes was demonstrated for higher growth temperatures (700-750ºC) [16], under enhanced diffusivity conditions, but in our case at 550ºC this process is limited. The holes performed with FIB are probably stepped and were expected to act as initial nucleation sites. For a growth temperature of 550ºC (like in our experiments) without the Au or the Ga presence, the formation of the Ge islands takes place on the FIB patterned Si substrates inside the holes [16]. In our experiment, we suspected that a different behavior regarding the island location was obtained. Based on our previous results obtained using the FIB ultra fast grabbing process (detailed in section 4.2), we assumed that following the FIB pattern array a big Ge island is formed in between four holes. The distance measured between the big Ge islands inside the FIB patterned areas is equal to 0.5 µm ± 0.02 µm, value consistent with the distance between the holes. Since the hole depth was so small (1 nm), from the AFM images was impossible to conclude if the big Ge islands grow inside or outside the holes.

In order to confirm our supposition and following the same procedure described above, a new series of experiments was done. To find the answer to this problem (the position of the big Ge island within the pattern) we decided to use a fixed ion dose and the only parameter changed between the different patterned squares was the distance

between the holes, which was increased from 0.5 µm to 1 µm with 0.1 µm steps. The used ion dose of 18.2x10^{-4} C/cm^{2} results in the formation of holes with a depth of 2 nm. In these patterning conditions it was possible to pass from digging holes to form mounds with increasing distance between the features (see figure 4.27 – AFM images). The dimensions of the mounds were detailed in figure 4.11.

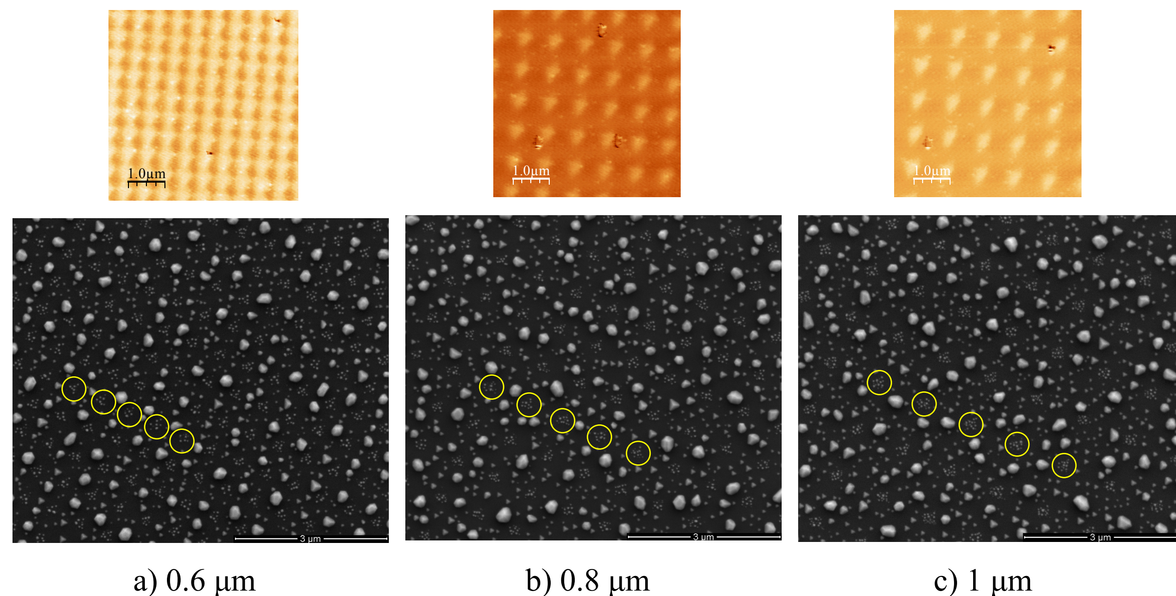

Figure 4.27. *AFM images recorded after the FIB patterning and before the MBE steps, showing the transition from holes to mounds with increasing distance between the holes. SEM images for the patterns with different distances between the holes: 0.6 µm (a), 0.8 µm (b), and 1 µm (c) were recorded after Ge growth. Deposited Ge amount was 5 nm and the growth temperature was 550ºC.*

Selected SEM images recorded after Ge deposition are presented in figure 4.27. We can clearly see that the obtained agglomeration of the small islands (some of them marked by yellow circles on the SEM images) correlates well with the increased distance between the holes/mounds. The fact that their order is not lost with the increasing distance between the holes show that the agglomerations of the small Ge islands are formed inside the holes. The small islands present facets and shapes characteristic for the Si substrate orientation and their density is barely influenced by the changes in the distance between the holes. This is consistent with the identical hole morphology independently of the distance between them, and with the fact that the Au amount was preserved. The big Ge islands grow ordered for 0.5 and 0.6 µm distances between the

holes, above these values they are losing the order, randomizing their positions (see figure 4.27c). This means that the big Ge islands grow between four holes/mounds, far from the Au rich areas, confirming our supposition concerning the island position inside the patterned areas. The holes are not anymore the favorable positions for single island per hole formation due to the Au presence.

The position of the islands between four Au rich areas was calculated by Li et al. [43] based on chemical potential theory to be more favorable from both thermodynamic and kinetic point of views. In this model, the contribution coming from curvature of the surface was neglected. In our experiments, the recorded evolution of the Ge islands with the distance between the holes is consistent with the theoretical model [43] and with the experimental results obtained by Robinson et. al. [3]. The probability for nucleation to take place at the center sites (between four holes) is increasing with the decrease of the distance between the holes. The relative distance L/R, calculated as the ratio of the distance between the two islands (L) and the Ge island radius (R) was 4.2 for the distances between the holes lower than 0.6 μm. Below the 4.2 value of R the Ge islands grow ordered at center sites (between four holes and/or four Au rich areas), while above the mentioned value the order is decreasing. For larger distances between the holes (between 0.7 and 1 μm) the nucleation site is nearly random (see figure 4.27 b and c). By increasing the distance between the holes, the flat surface is more favorable for the growth of the Ge islands from both energetic and strain point of view. The nucleation probability of the Ge islands at center sites is also directly correlated with the Ge diffusion length on Si(111) surface which is influenced by the Au presence and its amount. Therefore, the present results show that it is possible to control the nucleation sites by shifting the distance between the holes (Au rich areas).

Next, the ion dose influence on the Ge island growth mode and order was studied. By varying the ion doses it was possible to tune the Au amount per hole and to get the desired holes dimensions. The hole depth was varied by increasing the ion dose from $7x10^{-4}$ C/cm^2 (1 nm) to $44x10^{-4}$ C/cm^2 (4 nm), while the time needed to mill one hole was increased from 0.13 ms to 0.51 ms. The hole depth and the lateral diameter evolution with the employed ion doses is detailed in figure 4.28. The hole diameter was decreased from 380 nm to 300 nm with the increasing ion dose, while the hole depth was shifted from 1 nm to 4 nm, as measured from the AFM images displayed in figure 4.29

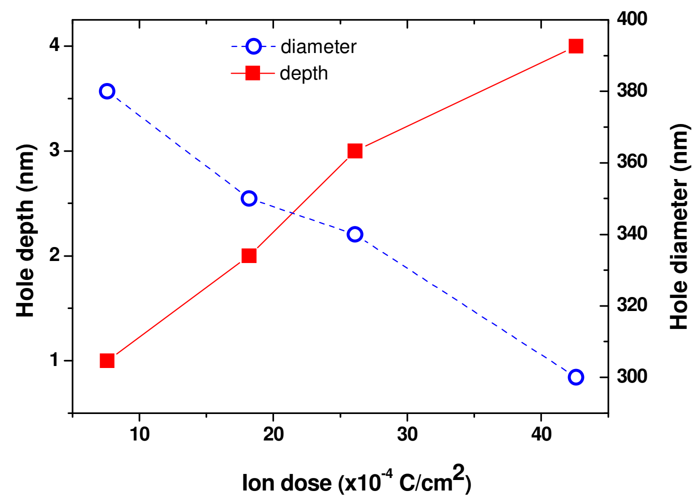

Figure 4.28. *Hole depth and diameter as a function of the ion dose used to pattern the Si(111) substrate. The lines are just guides to the eye.*

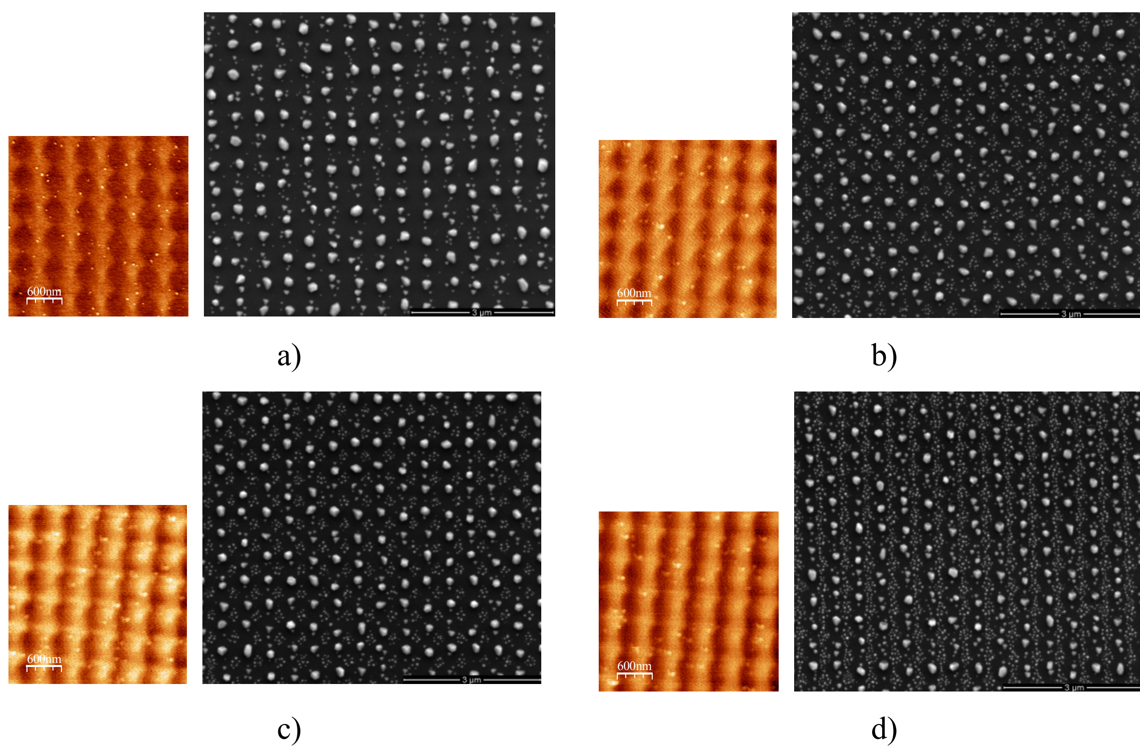

Figure 4.29. *AFM images of the patterns presenting holes with depths of 1, 2, 3, and 4 nm, corresponding to presented cases (a), (b), (c) and (d), respectively. These views were recorded after performing the patterns and before any treatment. SEM images were recorded after depositing 5 nm of Ge at 550ºC on top of the Si(111) patterned substrate.*

Furthermore, the evolution of the Ge island height and base diameter with the ion dose is shown in figure 4.30a. Due to the presence of the Au ions the dimensions of all the Ge islands formed inside the FIB patterned areas are reduced compared to the ones obtained for the islands that grow outside the patterned areas. With the increase of the ion dose (hole depth), the same tendency of size reduction was observed for both island shapes (pyramids and domes). As a consequence of the increase in the Au amount (ion dose from $7x10^{-4}$ C/cm^2 to $44x10^{-4}$ C/cm^2) a decrease with the same mean value in the height (~ 11 nm) and base diameter (~ 90 nm) (figure 4.30a) of both island types (small and big) was recorded.

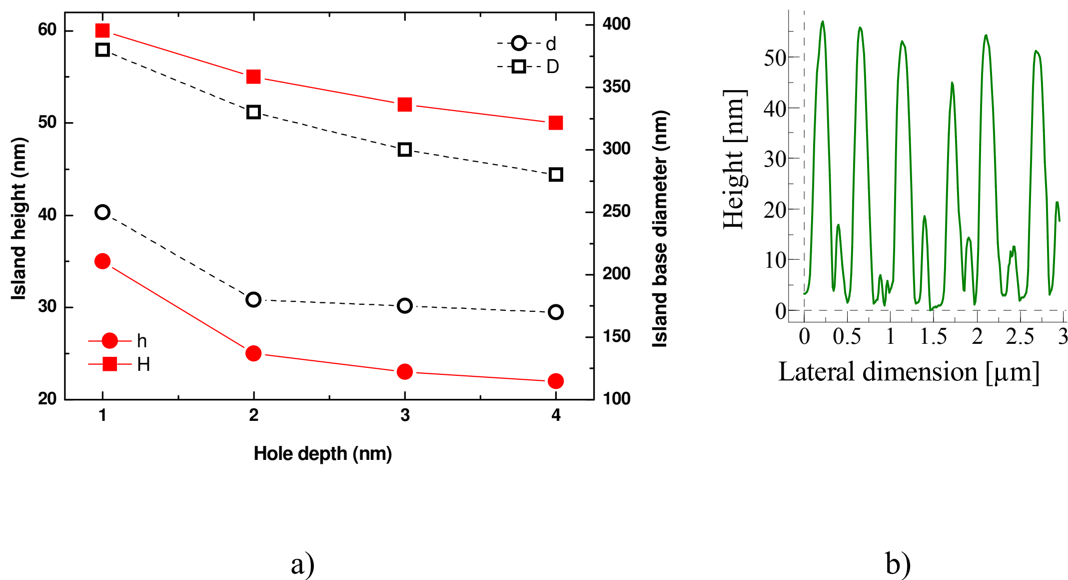

Figure 4.30. *a) Evolution of the average island heights and base diameters with hole depth (ion doses). The full red symbols correspond to the islands heights and the empty black ones to their base diameter. The letters d (diameter) and h (height) correspond to the small Ge islands grown inside the holes, while D (diameter) and H (height) are for the big islands formed between the holes. The lines are only guides to the eye. b) Height profile of the pattern with hole depths of 2 nm performed on the AFM image.*

For both categories of islands formed inside the patterned areas (inside the holes and between them) the aspect ratio is increased as a function of the ion dose. For an ion dose of $7.6x10^{-4}$ C/cm^2 small islands have an aspect ratio equal to 0.1-0.13, the big ones 0.15, while for an increased ion dose ($44x10^{-4}$ C/cm^2) the corresponding values are 0.12-0.17 and 0.2, respectively. These high values for the aspect ratio suggest that inside

patterned areas the islands tend to exhibit dome shapes, due to the Au ions presence. The Au acts as a surfactant and affects the surface facet energy, and hence increases island aspect ratio. Characteristic facets for dome shapes such as {113}, {15 3 23} and {20 4 23} were established [61].

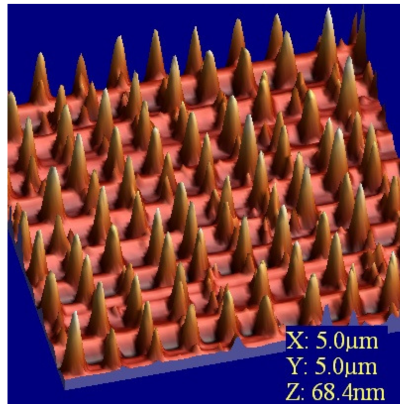

Figure 4.31. *3D AFM image of the Ge islands grown on a FIB patterned substrate. The image was recorded for the pattern with hole depth of 2 nm (ion dose: $18.2x10^{-4}$ C/cm^2). Uniform and pattern ordered Ge island ensembles were formed after depositing 5 nm of the grown material.*

In addition, it should be pointed out that the size of these ordered Ge islands is quite uniform (figure 4.30b and 4.31). The order of the big Ge islands formed between the holes was slightly diminished with the increase of the ion doses. The best order and uniformity for the dome shaped Ge islands was obtained when the substrate was patterned with an ion dose of $18.2x10^{-4}$ C/cm^2 (hole depth of 2 nm). The 3D AFM image recorded for the pattern with hole depth of 2 nm confirmed once more Ge islands order and good uniformity (see figure 4.31). In fact, the Au presence induced changes in the surface free energy and influenced the islands uniform distribution inside the patterned areas. The Au played the same role as carbon and boron [62-65] on increasing the Ge island homogeneity (figures 4.30b and 4.31).

We now turn to the small islands formed inside the holes. For a hole depth of 1 nm the big Ge islands (by big we refer to the dome shaped islands formed in between four holes) grow ordered with the pattern, whereas other islands with smaller dimensions are located in the nearest proximity of these domes. A deeper analysis of the SEM images recorded for this pattern show the formation of a small Ge island inside each hole, in

between four dome islands, as it can be seen in figure 4.32a. The evolution of the small Ge islands, formed inside the holes, with the ion doses and the differences in islands density can be clearly seen in figure 4.32 from a to c. The filling factor (islands per hole) increased from 1 small island per hole to an average number of 12-16 small islands per hole when increasing the ion dose from $7x10^{-4}$ C/cm^2 to $44x10^{-4}$ C/cm^2. This means that the total Ge volume within the holes is also increased with increasing ion dose. The increased number of small islands with the ion dose can be correlated with the holes morphology and with the increased Au amount present inside the holes. It is interesting to note that due to the Au existence the small islands do not coalesce easily, even if they are in an increased number and in a close proximity.

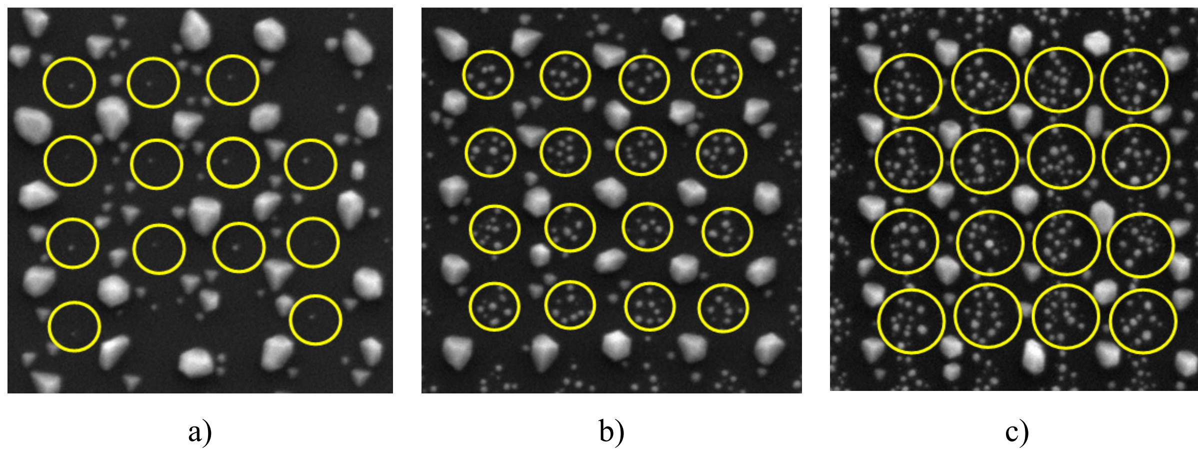

Figure 4.32. *Large scale SEM images recorded for hole depths of 1 nm (a), 3 nm (b), and 4 nm (c), respectively. The evolution of the small Ge islands formed inside the holes (marked by the yellow circles), in between four big islands, with the increasing ion dose is evident. The yellow circles mark the Ge islands formed inside the Au rich areas (holes). The SEM images size is 2.5x2.5* μm^2.

Theoretical models [66, 67] predicted that the preferential position for island nucleation within the patterned regions can be either on the apex or on the valley (e.g. inside the holes). Hu et al. [68] demonstrated that the islands can relax the strain better inside the holes. Usually, if the strain relaxation is dominant the islands will be formed inside the holes, and if the surface energy is dominant, then islands nucleate inside the holes and/or on the apex. In our experiments, islands with different sizes were formed both inside and in between the holes, this implying that the effect of the surface energy is

dominant. With the increase of the hole depth the reduced adatoms mobility promotes the formation of small islands. The closer to the holes bottom are the adatoms, the lower is their surface migration length. The evolution of the Ge islands within the hole patterned areas is strikingly different from the previous reported data [16, 69] due to the Au presence inside the patterns.

Ge islands growth on a Si(001) FIB patterned substrate

The effect of the FIB patterning with Au^{2+} ions was investigated for the Si(001) crystallographic orientation also. The differences between the patterned (low ion doses) and nonpatterned areas for this substrate orientation can be clearly seen (figure 4.33a). Outside patterned areas the Ge islands are formed randomly, while inside this area the growth is influenced by the pattern. The Au effect on reducing island dimensions inside patterned areas compared to outside ones was observed for this substrate orientation also. The height and base diameter of the islands from both regions (patterned and nonpatterned) are shown in figure 4.33b. Good island size uniformity inside patterned areas is also achieved for the (001) substrate orientation. The Ge islands order is not the same for the two substrate orientations, behavior that can be caused by the Si(001) pattern nonuniformity. This could also explain the growth of the small islands in the Au presence, following the pattern, and forming almost a line. The missing of a single Ge island in between four holes was caused by the pattern morphology and the changes induced by it. The coalescence of the Ge islands is also absent in this case.

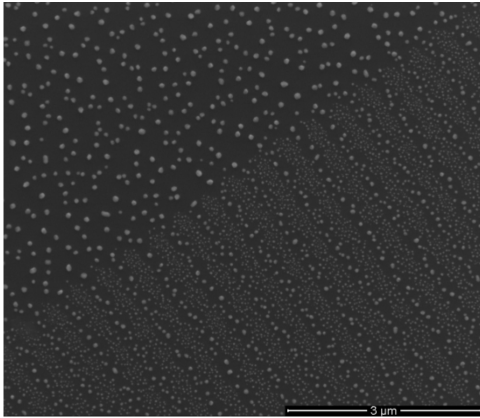

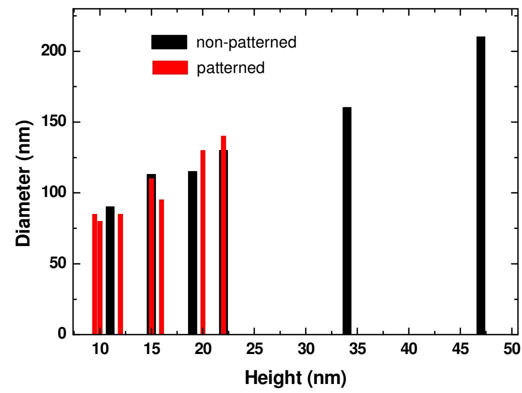

a) b)

Figure 4.33. *a) SEM image presenting the formation of the Ge islands on a Si(001) substrate patterned using an ion dose of 1.18x10^{-4} C/cm^{2}. After performing an annealing for 15 minutes at growth temperature (550ºC), 5 nm of Ge were deposited. Left upper corner represents a nonpatterned area. b) The height and diameter of the Ge islands (pyramids and domes) formed inside and outside the patterned areas.*

4.4.3.2 Intermediate ion dose

We meant to investigate the formation of the Ge nanowires (NWs) on Si substrates, particularly on (001), and to follow the influence of the clusters density on the morphological evolution of the NWs. In order to achieve this objective, the formation of the AuSi clusters inside the patterned areas is a must. The presence of the Au-rich droplet formation inside the patterns performed with the low ion doses was not demonstrated. Compared to the literature data [53, 70, 71] it is clear that the Au amount inside patterned areas was too low to promote the growth of the nanowires. In consequence, the main requirement in the following was to increase the Au amount per hole. For this purpose, the hole depth was kept below some nanometers (< 10 nm) and the time that FIB stayed in one point was increased, hence increasing the employed ion doses between 44 $x10^{-4}$ and 110 $x10^{-4}$ C/cm^2. The total time to perform the patterned squares (25x25 μm^2) was increased in this ion dose regime from 8 seconds to 4 minutes. The evolution of the hole dimensions as a function of the employed ion doses is presented in figure 4.34a. The hole depth was increased between 1 and 8 nm, whereas their diameter gradually changed from 80 to 220 nm. A roughly linear increase of the hole aspect ratio was recorded, corresponding to the almost linear increase of both depth and diameter. The periodicity of the holes (the distance between the holes was kept constant at 0.5 μm) is shown in figure 4.34b. The inset of the AFM image presents the hole profiles, showing the uniformity of their dimensions.

Before performing the thermal treatments the Au ion presence inside the holes was not detected by SEM or AFM measurements. We followed the strategy developed in the literature using the experimental conditions described earlier (section 4.1), similar to those reported for the solid-source MBE growth of Si/Ge NWs on Si(111) using AuSi clusters as catalyst seeds [38, 72]. In order to form the AuSi clusters, the patterned substrates were cleaned and immediately introduced inside the MBE chamber (~ 10^{-11} torr) where the thermal treatments were performed (UHV - 15 minutes and 550ºC). Subsequently to the annealing step, different Ge amounts between 2 and 12 nm were deposited by solid source MBE.

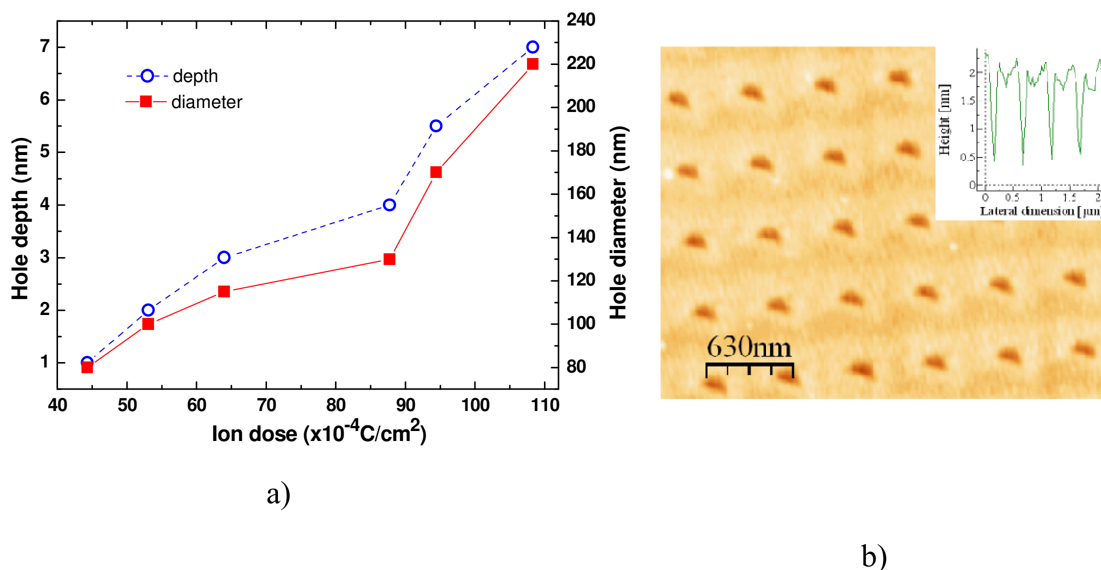

a)

b)

Figure 4.34. *a) Hole depth and diameter as a function of the ion doses used to pattern the Si(001) substrate. The hole depth is represented with the open blue circles and the hole diameter with the red squares. The lines (straight and dashed) are just guides to the eye. b) AFM observation of the patterned area using an ion dose of 53x10^{-4} C/cm^{2} and the hole profiles (inset) shows their uniformity and periodicity.*

A closer look to the sample surface after Ge deposition clearly states the difference between the two areas; patterned regions are easily distinguished from the unpatterned ones, and the boundary between the two areas is clearly seen (figures 4.35 a, b). Ge follows a 3D growth outside patterned areas, even if was deposited under the same conditions. We checked that these 3D islands present the shapes commonly observed in the literature with a bimodal distribution of “huts” and “domes”, as can be seen in figure 4.35b [55]. As expected, no order or size uniformity for the Ge islands formed outside patterned areas was recorded.

The SEM observations of the surface show the formation of NWs lying on the Si(001) surface on the patterned areas (figure 4.35c). The back scattering SEM (BS-SEM) images reveal the presence of the Au rich particles at the tip of the NWs. These nanoparticles more or less fit the transversal size of the NWs. One can also note that the NWs are all oriented along the [110] directions, even if the NWs present kinks and rotations from one direction to another. The obtained NWs have approximately trapezoidal sections and a mean aspect ratio about 0.05 with a section square root of about

50-60 nm and a length of around 1 μm (figure 4.35). This shape was previously reported for the SiGe NWs [73] synthesized via Au catalyzed VLS growth and the formation of this shape was suggested to be a result of the axial VLS growth and conformal deposition.

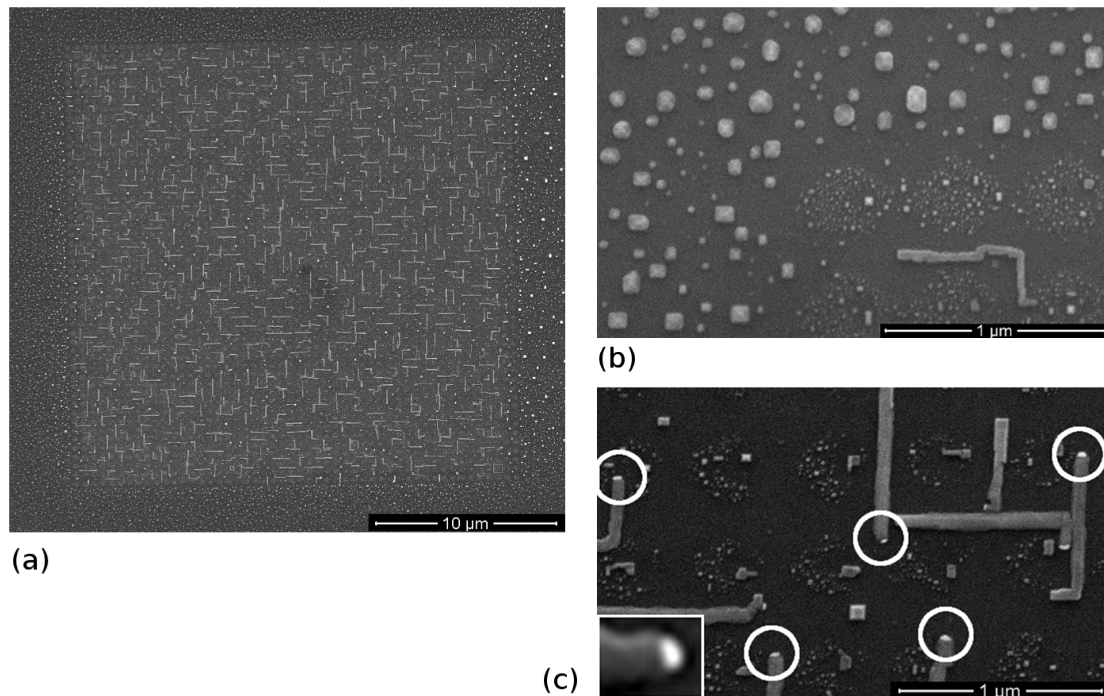

Figure 4.35. *a) Large scale SEM image of the patterned and unpatterned areas. b) SEM image showing the bimodal distribution of "hut" and "dome" islands on the unpatterned area and a Ge NW on a patterned area (low right corner). c) BS-SEM image of Au rich clusters at the tip of NWs; the inset shows a higher magnification image of the cluster.*

Additionally, a closer analysis of a single nanowire was also done. The AFM image of a straight NW with the corresponding profiles taken on its different parts is shown in figure 4.36. A decrease of around 10 nm in height is recorded between the two ends on the nanowire, as can be seen in figure 4.36 (left side, upper corner). The lowest end is attributed to droplet existence. The lateral profiles performed along the nanowire show also a decrease in lateral diameter from 160 (right upper corner) to 125 nm (left lower corner) as it can be seen in figure 4.36.

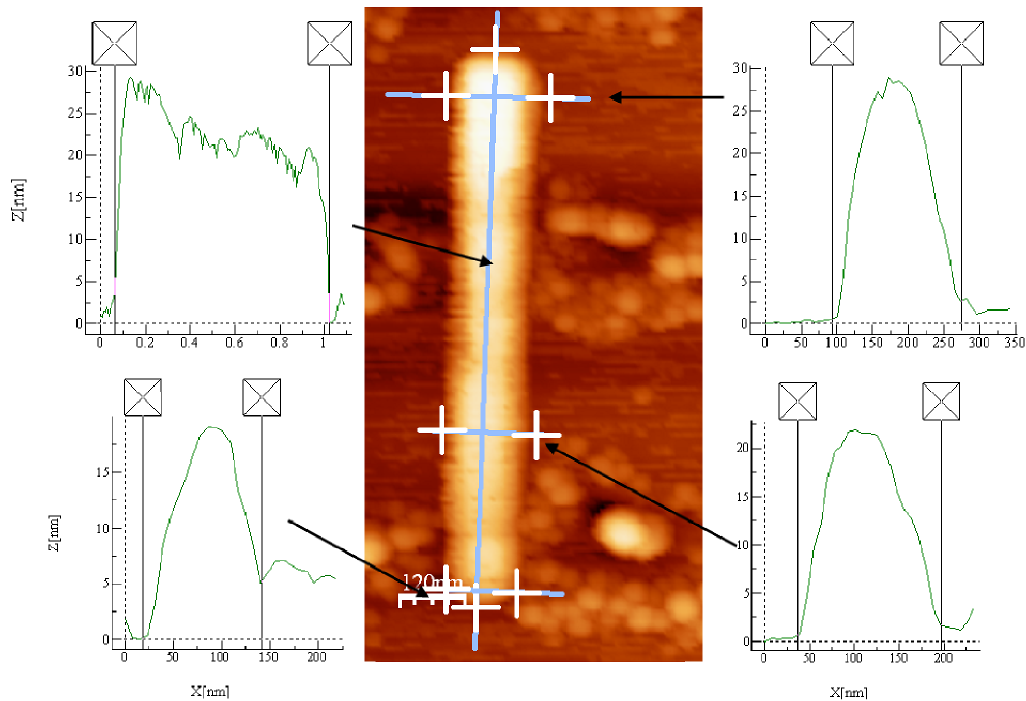

Figure 4.36. *AFM image of a single Ge nanowire with the transversal and the longitudinal profiles. The profiles correspond to the different parts of the nanowire as indicated.*

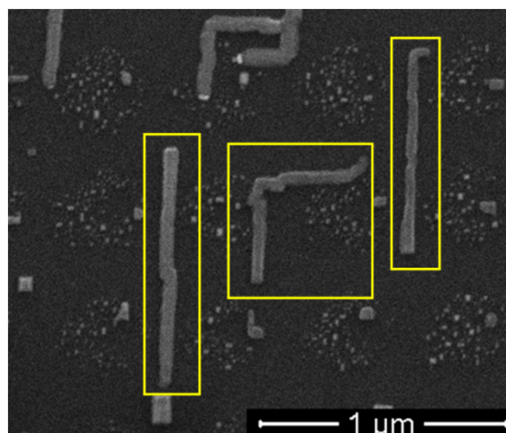

Figure 4.37. *High resolution SEM images of Ge nanowires with and without (NWs inside the yellow squares) Au rich droplets at their tips.*

Some of the nanowires do not present anymore the AuSi droplet (figure 4.37) at their ends. They were probably consumed during the growth process. The nanowires found in this situation are marked in figure 4.37 with yellow squares. This situation was

more common for the two lowest ion doses from the investigated range and is consistent with a reduced Au amount.

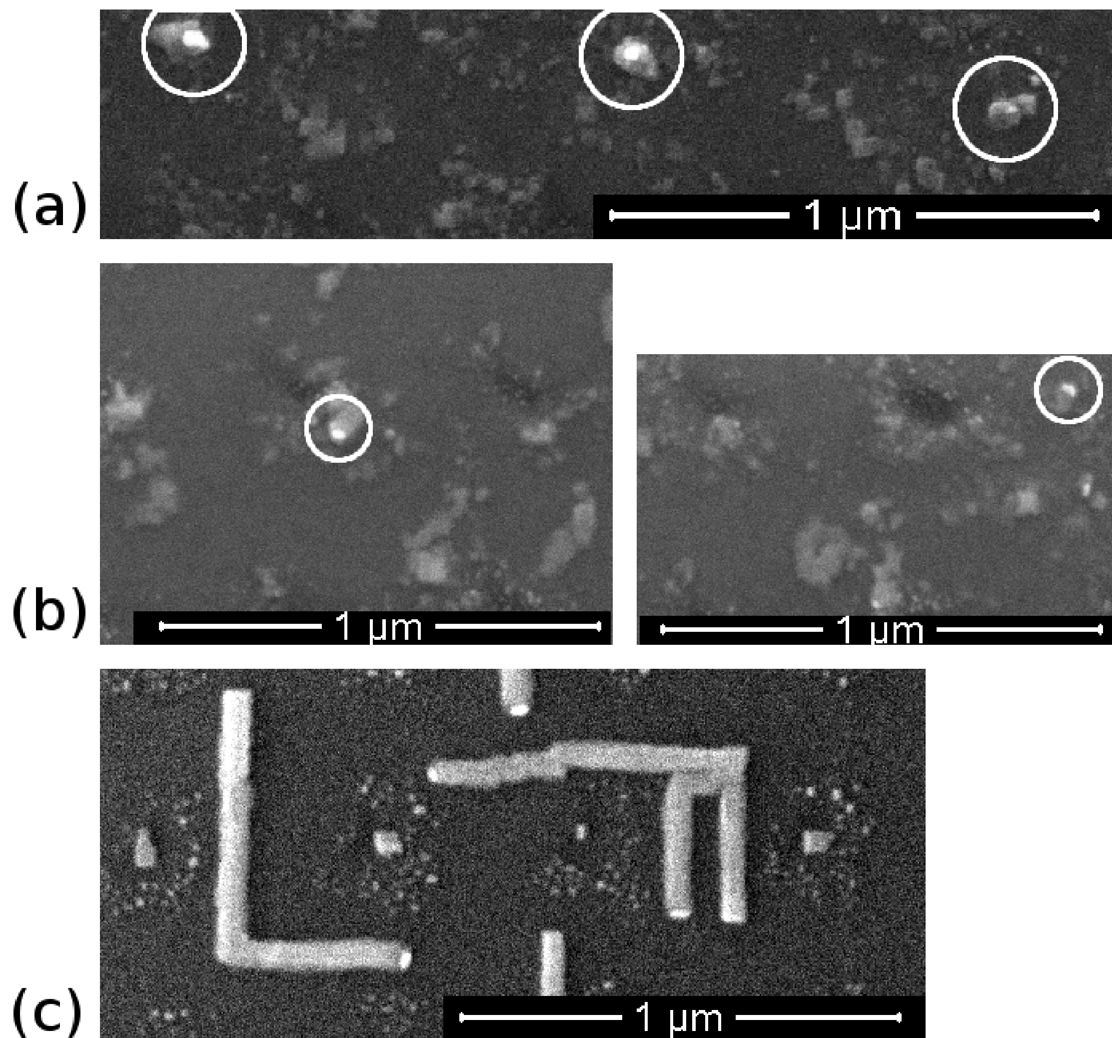

Figure 4.38. *a) BS-SEM image of the first nucleation stage on the Au rich clusters with NW growth along [001]. b) SEM images of the second growth stage misoriented from [001]. c) SEM image of the NWs at the end of the growth process along the [110] directions parallel to the substrate.*

A deeper investigation of the NW formation at different growth stages evidenced first the nucleation of Ge nanostructures at AuSi clusters accompanied with the initial NW growth almost perpendicular to the surface up to a critical length (figure 4.38a), second the kinking of NWs (figure 4.38b) and third, their crawling on the substrate (figure 4.35c). Under different experimental conditions, it was shown that a continuous

tapering of the nanowire pedestal could be produced, with a pedestal becoming so narrow, that the catalyst rolls off, producing the crawling of the nanowire along the substrate [74, 75].

To address the growth mechanism of Ge NWs along the substrate, we have to consider the dynamical evolution of NW growth. It was reported that the wire growth is controlled by the dynamical evolution of the trijunction between solid (Ge in our case), vapor and liquid (AuSi) [76, 77]. The liquid-solid kinetics was expressed by Schwarz et al. [76] as:

$$v_s = \alpha_{ls}(\mu_l - \mu_s) \qquad 4.1$$

where v_s is the local growth velocity of the solid, α_{ls} is a kinetic rate coefficient taken as nonzero only at the L-S interface, μ_s and μ_l are the chemical potentials of the solid and liquid, respectively, and μ_s was expressed as:

$$\mu_s = \Omega_s\left[\kappa\gamma + \kappa\frac{\partial^2\gamma}{\partial\hat{n}^2} + p + C(\kappa)\right] \qquad 4.2$$

where $\kappa\gamma$ is the Gibbs term, generalized with the second term $\left(\kappa\frac{\partial^2\gamma}{\partial\hat{n}^2}\right)$ to an orientation-dependent interface energy with γ changing over the interface following a step function: $\gamma = \gamma_{ls}\Theta_l + \gamma_{vs}(1-\Theta_l)$, where γ_{ls} and γ_{vs} are the orientation-dependent interfacial energies between the liquid and the solid, and the vapor and the solid, respectively, and Θ_l is a step function representing the pressure. The effect of anisotropy in γ is introduced using the simple relationship:

$$\gamma(\hat{n}) \approx \gamma(1-\varepsilon_n \cos n\theta) \qquad 4.3$$

Thus, γ_{vs} and γ_{ls} are multiplied by $(1-\varepsilon_n \cos n\theta)$, where θ gives the local surface orientation, n is the number of facets and ε_n an arbitrary coefficient depending on the surface symmetry. The orientation of the surface is given by its normal vector $\hat{n}$, $\kappa = -\nabla_s\hat{n}$ is the curvature tensor, p is the force normal to the surface, and $C(\kappa)$ is a regularization term limiting the sharpness of edges on faceted surfaces.

The term μ_l was described using a simplified expression:

$$\mu_l = \beta(c_l - c_0) + \Omega_l\gamma_{vl}\kappa_l \qquad 4.4$$

where the first term represents the supersaturation with respect to the equilibrium liquidus concentration and the second term is the Gibbs-Thomson effect of surface tension.

As a consequence, the NW growth described in equation 4.1 is based first on the kinetic factor (α_{ls}) that mainly depends on the surface diffusion of atoms and second on $\Delta\mu$, the formation of new facets at the trijunction, which needs the availability of monoatomic kinks and steps at the L-S interface. The additional energy requested to form a new facet depends both on the surface energy of the existing flat facet and on the edge energy of this facet (according to equation 4.2). These two terms are orientation dependent and described for instance, following equation 4.3. Therefore, the NW sidewalls should follow the orientations that minimize μ_s since μ_l is expected to remain almost constant (from equation 4.4). In our experimental conditions, we consider that both the kinetic rate of growth (α_{ls}) and μ_l remain constant, during epitaxial growth of Ge on Si(001) substrate, whereas there is a strong strain-dependent evolution of μ_s due to the change of γ_{vs} and $\left(\kappa \frac{\partial^2 \gamma_{vs}}{\partial \hat{n}^2}\right)$ in equation 4.2. In the case of (001) surface, γ_{vs} increases and $\left(\kappa \frac{\partial^2 \gamma_{vs}}{\partial \hat{n}^2}\right)$ decreases under compressive epitaxial strain of Ge on Si [78]. During the first stage of growth, the NWs are under compressive strain and the energy of [001] step formation becomes low due to a reduction of the step edge energy with strain [78]. At the same time, the (001) surface energy (γ_{001}) increases while the surface energy of somewhat misoriented stepped surfaces decreases. In particular, it was demonstrated that 11° off misoriented (105) facets have lower surface energy (γ_{105}) than γ_{001} [78]. This means that (105) facets are apt to nucleate at the expense of biaxially strained (001) facets [79, 80]. Consequently, below a critical deposited thickness (under compressive strain), the nucleation of new facets is favored by the decrease of the step formation with strain, but because of the destabilization of (001), the interface orientation will rotate during growth to follow for instance (105) facets. This results in a small tapering of the NWs pedestal and a slight misorientation of the NW sidewalls (figure 4.38b). A schematization of the growth process is drawn in figure 4.39 starting from the initial state (figure 4.39a). The first stage of the NW growth is depicted in figure 4.39b. In order to keep the equilibrium value of the contact angle corresponding to the trijunction equilibrium and also for matter conservation, the droplet slightly rolls off the surface and covers the sidewall of the incipient NW.

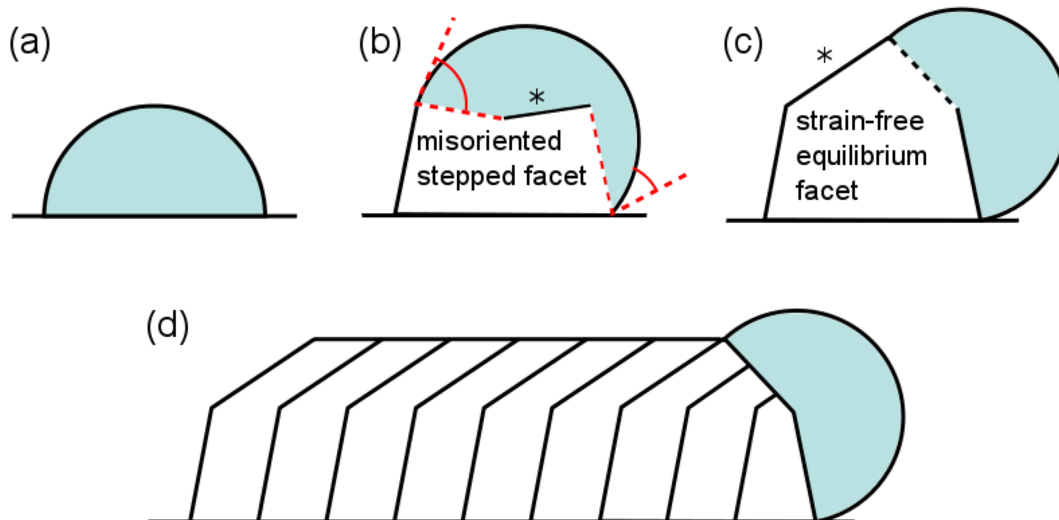

Figure 4.39. *Schematic representation of the three growth stages of the NW starting from a) the initial state with the AuSi cluster lying at the Si(001) surface; b) represents the first stage of the NW growth. This stage is characterized by a small pedestal tapering due to the formation of slightly misoriented stepped facets (*), for instance (105), and the rolling out of the catalyst liquid droplet along the sidewall of the NW; c) shows the strong kinking of the NW and its morphological change with the onset of strain-free equilibrium facets, for instance (113) and (111); d) shows the last stage crawling of the NW along the substrate surface and its elongation on the substrate.*

The second growth stage starts after a critical grown thickness (or NW height) when the strain is relaxed by dislocation nucleation (after ~5 nm NW height, which is larger than in 2D layers). At this point, a strong kinking of the Ge NWs is observed experimentally (figure 4.38b), the strain-free equilibrium facets nucleate on the sidewalls of the NWs producing a strong change of their growth axis direction (figure 4.39c). This morphological change is similar to the "hut" to "dome" islands transformation observed in 2D dimensions, which was explained by an abrupt increase of γ_{105} and of $\left(\kappa \frac{\partial^2 \gamma_{vs}}{\partial \hat{n}^2}\right)$ due to strain relaxation. The NW develop similar (113) and (111) sidewalls like the equilibrium facets of relaxed Ge "domes", while elastically strained "hut" pyramidal islands have (105) side facets that represent the minimum of the Ge surface energy under strain [78, 79]. During further growth (NW length, about 100 nm in our

experiments), the liquid cluster drops in contact with the Si(001) substrate. It rolls on the Si(001) surface producing the crawling of the NW along the substrate and further growth with its axis parallel to the substrate (figure 4.39d), along [110] directions providing the extension of the (113) and (111) side facets. These different growth stages, in particular crawling of NWs, were not observed on Si(111) [81, 82] due to the very different anisotropy of the surface energy $\left(\kappa \frac{\partial^2 \gamma_{vs}}{\partial \hat{n}^2}\right)$, around [111] compared to [001] [83]. This is also consistent with the different growth modes of Ge islands on Si(001) and Si(111) observed in absence of AuSi clusters seeds [58, 84].

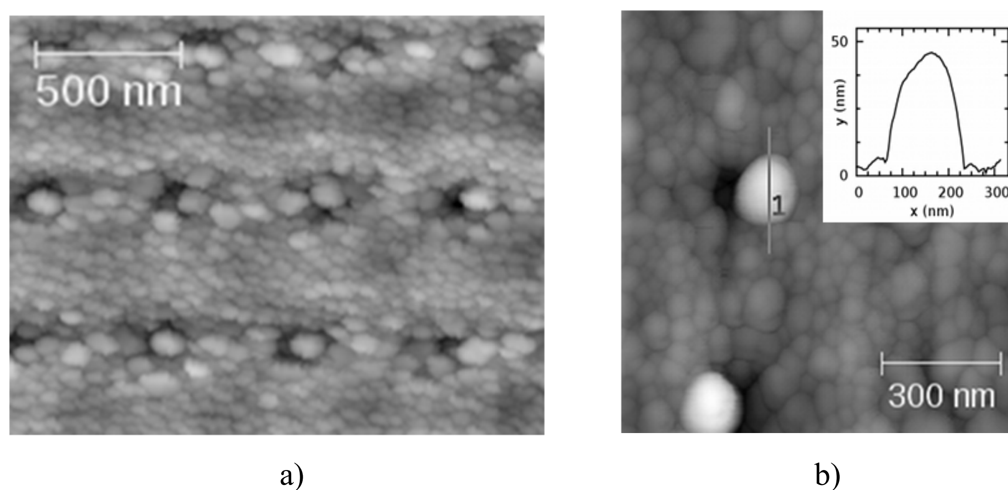

a) b)

Figure 4.40. *a) AFM image of a patterned region after depositing 12 nm of Ge. Ordering effects given by the 500 nm pitch patterned holes are much stronger in this orientation; b) Detail and profile of one of the observed NWs.*

We also performed growth on Si(111) patterned substrates to confirm that the crawling of NWs that we observed on Si(001) is an intrinsic effect. Indeed, on Si(111) we observe similar growth as in the literature [81, 82], even for very high Ge coverage up to 12 nm. This is seen in figures 4.40 and figure 4.41 in the initial stage of growth the Ge NWs grow perpendicular to the surface following a [111] direction but then, eventually, other orientations [81] are also found.

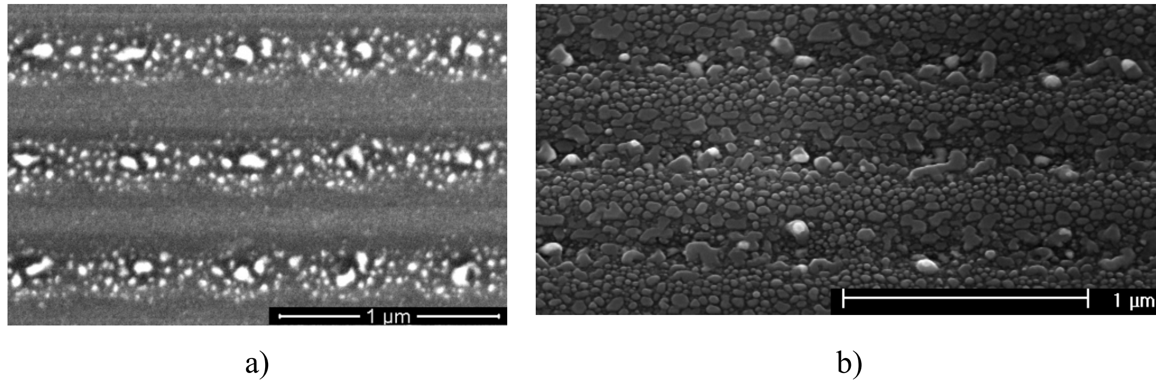

a) b)

Figure 4.41. *Growth stages of the Ge NWs on patterned Si(111) substrates. SEM images recorded after depositing 2 nm (a) and 12 nm (b) of Ge. Ordering effects are stronger in this case. Light areas indicate the Au presence.*

The growth mode by MBE of Ge seems similar to that of Si(111) NWs [38, 84], probably because the (111) surface is readily dislocated almost in the initial stages of growth and the subsequent Ge(111) growth is almost strain-free. In these first attempts, the Ge NWs are not very long (figure 4.40b) because roughness induced by the FIB patterning limits the diffusion of material in this case, increasing nucleation sites between NWs. However, Ge nanostructures at the patterned sites are clearly seen in figure 4.40a. The corresponding SEM image (figure 4.41 a and b) after depositing 2 and 12 nm of Ge, indicates presence of Au only at the top of formed nanostructures. Notice also that in absence of crawling effects ordering by the patterns is quite effective.

Despite the lack of large scale ordering that was expected when patterning the substrates, it is nevertheless clear from figure 4.38 that all the NWs nucleate close to the patterns in the areas where AuSi clusters are observed. However, a much better order for the Ge nanowires was obtained for another sample, where Si(001) substrate was patterned using slightly different FIB conditions. Probe current was increased from 60 to 80 pA, and probably not the identical adjustments for FIB correction of focus and astigmatism were done. The increased probe current implied a reduction of time per hole with only 4 ms. The AFM investigations (figure 4.42a) of the patterned substrate revealed a hole depth of 1.5 nm (inset figure 4.42a) and their fine periodicity. Calculated ion dose for this pattern is in the same range like the one showed in figure 4.34, for the holes with a ~2 nm depth. As clearly revealed by the BS-SEM images recorded for this pattern (figure 4.42b), nanowires tend to be 1 per hole, every 0.5 µm. Such a region of 1 NW per hole is marked

in the SEM image by yellow circles, and the order is present in all the directions, as pointed out by the light blue dashed lines. The formation of 1 NW per hole was obtained with a good reproducibility even at large scale (25x25 μm^2). Additionally, in plane NWs were formed in between the holes, presenting kinks and a larger mean length compared to the ones inside the holes. The present in plane NWs are shorter (below 700 nm) compared to the ones obtained in the case of the ~2 nm hole depth (around 1 μm) even if the same amount of material was deposited. For several holes even a second nanowire was formed, but with reduced dimensions compared to their closest neighbor. These holes with 2 NWs per hole are pointed out in figure 4.42b, and marked with purple squares. The NWs formed inside the holes are in one of the two growth stages presented in figures 4.38 a and b.

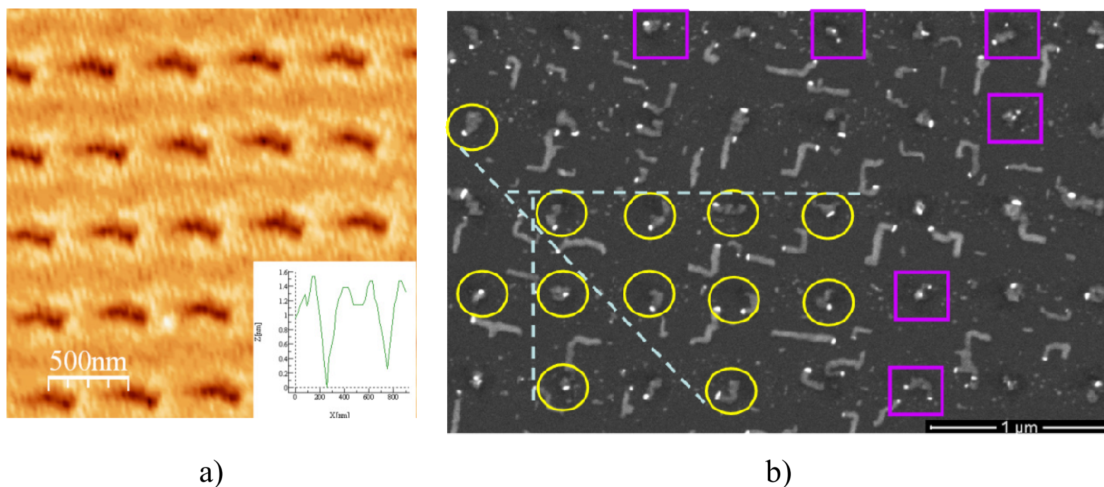

Figure 4.42. *a) AFM image recorded for the holes before any treatment, and the inset shows the profiles of the holes. b) BS-SEM image of the Si(001) FIB patterned substrate after Ge deposition. Lighter spots represent the Au rich clusters. Pattern ordered Ge nanowires: 1 NW per hole - marked by yellow circles. The dashed light blue lines are only guide to the eye to better see the order and 1NW per hole formation on different direction. Purple squares indicate the presence of 2 NWs per hole.*

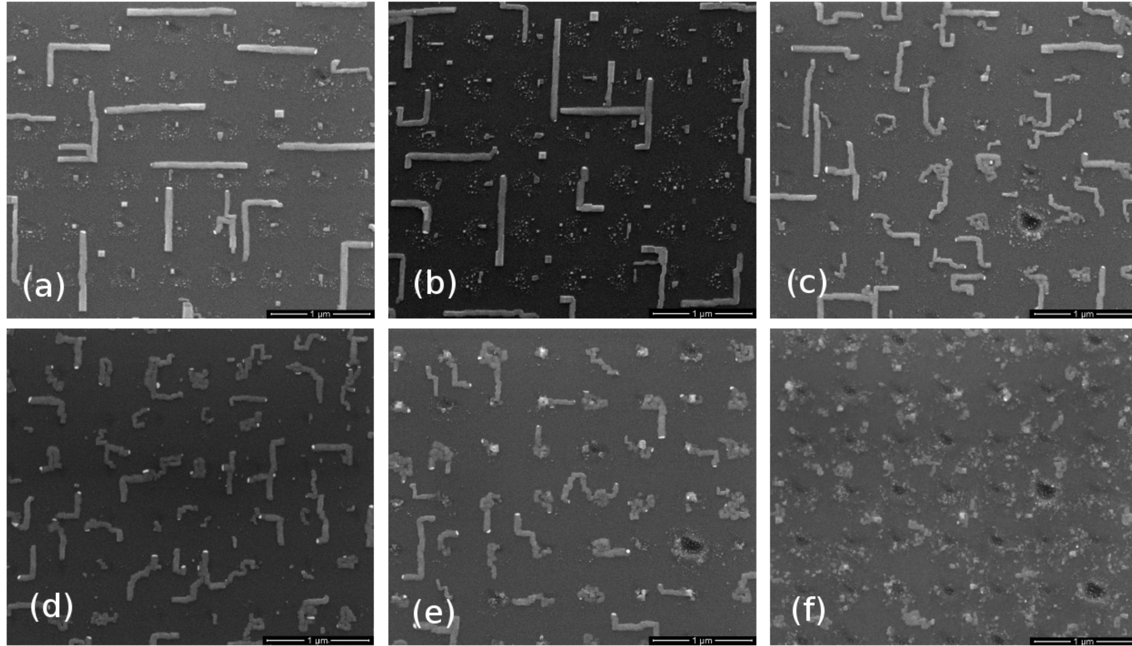

Figure 4.43. *FIB ion dose (intermediate range) influence on the NW morphological evolution. Wires grow predominantly along <110> directions but the surface roughness acts as a diffusion barrier, producing an increasing waviness until growth is almost hindered.*

In the Si(001) case, we investigated the effect of the FIB ion dose on the morphological evolution of NWs crawling. We note that the higher the ion dose, the wavier are the NWs (figure 4.43). At low doses (values from intermediate ion dose range – figure 4.43 a and b), the NWs are almost straight with few kinks at 90°, whereas at high doses they are almost rolled up with a large density of kinks in the two [110] directions (see figure 4.43 d and e). This morphological evolution is not associated to any other relevant change, since both the NW total length and diameter remain rather constant (see table 4.3) and the observed AuSi cluster size remains also constant. We attribute the waviness to kinking processes produced by interactions between NWs and substrate steps and kinks. Indeed, we observed that for a higher ion dose the density of steps and kinks on the surface increases (associated to a higher RMS roughness of the surface). According to the accepted models of epitaxial growth [86], it can be argued that these sites will act as diffusion barriers, hindering the NWs from crossing those steps and kinks and producing the waviness. This is related to the Ehrlich-Schwoebel effect [87] found in other situations of epitaxial growth.

Table 4.3. Evolution of the mean length and diameter with the ion dose.

Ion dose [x10^{-4}C/cm^2]	Mean length [nm]	Mean diameter [nm]
44	1200±100	52±5
53	1100±100	53±5
64	1050±100	53±5
88	980±100	47±5
94	700±100	44±5

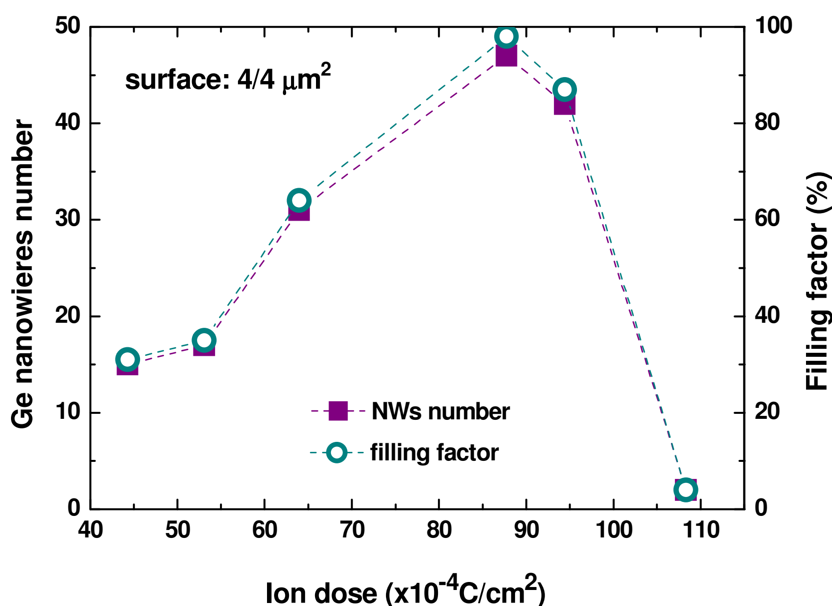

Figure 4.44. *Evolution of the number of the Ge nanowires (purple squares) and calculated filling factor (dark cyan empty circles) with the employed ion doses. The lines are guide to the eye.*

Furthermore, the evolution of the Ge nanowires in terms of their number and filling factor was followed as a function of the ion dose (figure 4.44). For this determination 4x4 μm^2 areas were selected on the SEM images recorded for each ion dose (samples presented in figure 4.43). In each image with mentioned size 48 FIB holes were counted. The filling factor was calculated considering the 48 holes and the number of the NWs obtained for each pattern. As shown in figure 4.44, for the two lowest ion doses (44.5x10^{-4} C/cm^2 and 53.1x10^{-4} C/cm^2) the number of the Ge nanowires formed is

reduced (15, 17 NWs) compared to the one recorded for the Ge NWs formed on the patterns obtained using the $88x10^{-4}$ C/cm^2 and $94x10^{-4}$ C/cm^2 ion doses (47, 42 NWs). For these two high ion doses the filling factor is quite high 98% and 87% respectively, which means that we obtained ~ 1NW per hole, while for the two low ion doses is decreasing considerably (31-35%). For the highest ion dose ($108x10^{-4}$ C/cm^2) a dramatic decrease of the number of the nanowires (only 2 NWs) and filling factor takes place.

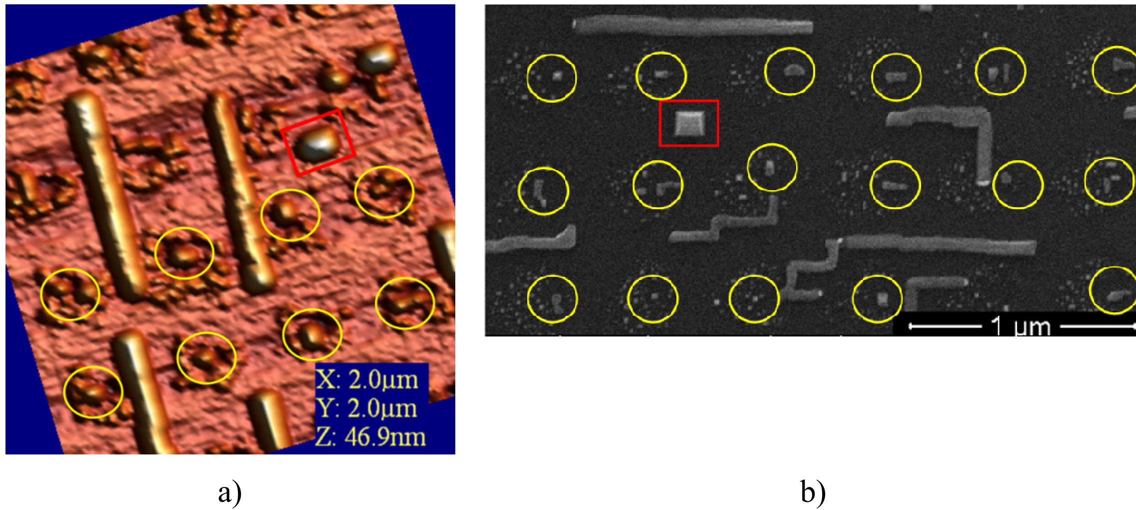

a) b)

Figure 4.45. *3D AFM (a) and SEM (b) images of the in plane Ge nanowires and islands. With yellow circles are marked Ge islands inside the holes, and with the red square the island formed in between four holes. Good order of the Ge islands with the patterns was achieved.*

Moreover, the causes of the reduced values (30-35%) of the filling factor were investigated. For the low ion doses ($44.5x10^{-4}$ C/cm^2 and $53.1x10^{-4}$ C/cm^2) the tendency is to form a big Ge island per hole, beside the small islands and the nanowires formed inside and/or in between the holes. These islands have smaller size than the ones from the unpatterned zones (figure 4.35 b and c). The AFM 3D and the high resolution SEM images show the presence of the two types of nanostructures (islands and nanowires) at different positions as indicated in figure 4.45. Due to the substrates increased roughness and growth material reduced diffusivity inside the patterned areas, not all the deposited material is trapped by the Au rich droplets and incorporated in the nanowires. The formation of the Ge islands with a perfect square base was obtained in between four holes (figure 4.45 – marked by red square). Their position is consistent with the results obtained

for islands when the substrates were patterned using the low ion doses. Based on these observations, these two ion doses can be considered as a transition between only islands and only nanowire formation. The distance between holes was always 0.5 μm, but for these two ion doses the flat space between the holes is bigger compared to the following larger ion doses. This hypothesis is sustained by the hole diameter linear evolution with the ion doses, previously revealed in figure 4.34, and is in agreement with the formation of straight in plane nanowires. High resolution BS-SEM images of the patterns did not reveal the presence of the Au ions, or formation of the Au rich droplets inside the holes where the Ge islands were formed, only at nanowires tips. As it can be seen in figure 4.45 the big Ge islands are not located at holes center sites, but more in holes "walls", position consistent with the reported data [16].

Raman characterization of the in-plane Ge nanowires formed on Si substrates patterned by a Focused Ion Beam

The Ge nanostructures formed both inside and outside patterned areas were investigated by Raman spectroscopy. The micro Raman signal was collected from areas of 1x1 μm^2, which means that approximately one to three nanowires were simultaneously illuminated. The collection of the Raman spectra recorded on different areas of the sample is shown in figure 4.46. The black spectrum (named as outside in figure 4.46), was recorded from a region where only Ge islands were formed, in the absence of the FIB patterning. The rest of the spectra were obtained from the squares FIB patterned using different ion doses as indicated in the figure 4.46. Peak intensities were normalized to that of the Si-substrate. To determine the maximum peak positions, the measured spectra were fitted with Gaussian line shapes for Ge-Ge and Si-Ge bands, while for the Si-substrate peak we used a Lorentzian.

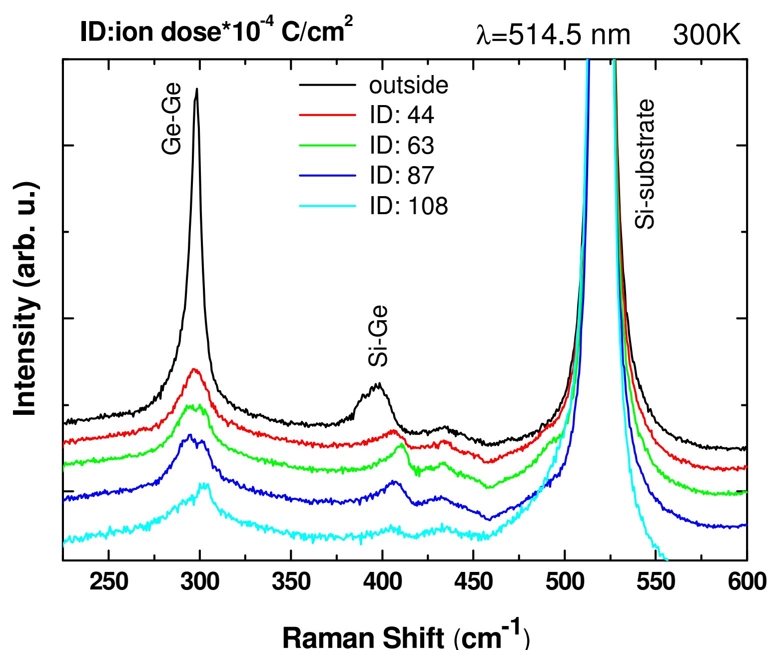

Figure 4.46. *Raman spectra recorded outside (Ge islands) and inside (Ge nanowires) the patterned areas after depositing 2 nm of Ge at 550ºC. Peak assignments are indicated.*

Contributions coming from Ge-Ge, Si-Ge modes and Si-substrate are found in the Raman spectra recorded on both patterned and nonpatterned areas. The peak at ~520.7

cm^{-1} originates from the Si substrate, while those around 410 and 300 cm^{-1} arise from the SiGe and GeGe alloy vibrational modes, respectively. In addition, around 300 cm^{-1} a second order (2TA) arising from the substrate is observed. The presence of a relatively strong SiGe band shows that during the growth stage a strong intermixing between the in-plane nanowires and the Si substrate took place. No contributions from Au-Ge or Au-Si were observed in the micro-Raman spectra. In the case of the Ge nanowires that followed the [111] direction of the Si(111) substrate, no band for the Si-Ge vibrations was detected [88], which indicates a higher Ge content in these nanowires as compared to the (001) case.

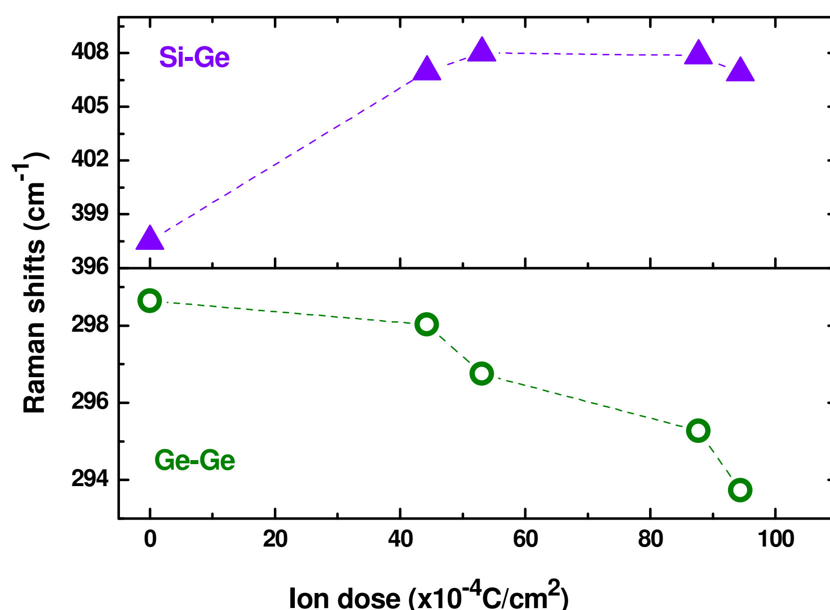

Figure 4.47. *Phonon frequencies (Ge-Ge and Si-Ge) evolution from Ge islands to nanowires (from straight to rolled up and kinked ones) as a function of the ion doses used to pattern the Si substrates. The dashed lines are guides to the eye.*

The evolution of the phonon frequencies (Ge-Ge and Si-Ge) with the ion dose is shown in figure 4.47. The ion dose value equal to zero corresponds to the unpatterned areas, where only Ge islands were formed. With increasing ion dose a shift to lower wavenumbers for the Ge-Ge phonon was observed, while an opposite behavior was evidenced for the Si-Ge mode. The shifts recorded for the Ge-Ge phonon frequency from 298.5 cm^{-1} to 293 cm^{-1} and for the Si-Ge band from 397 cm^{-1} to 407 cm^{-1} are correlated with the transition from islands, through straight nanowires to kinked and rolled ones. We

estimated the strain and the Ge content of the islands and nanowires following the procedure described in chapter 3. With this approximation, we only need a precise determination of the Raman frequencies of the Ge-Ge and Si-Ge modes. The resulting Ge content and strain are shown in figure 4.48 as a function of the ion dose used to pattern the Si substrates. The Ge content within the islands (86%) is much higher than the one obtained for the nanowires (68-75%). Even if we deposited inside and outside the patterned areas the same Ge amount at the same time, a difference in composition of more than 10% was obtained between the two nanostructures investigated. This demonstrates that intermixing between the Ge and the Si substrate increases in the presence of holes and Au clusters.

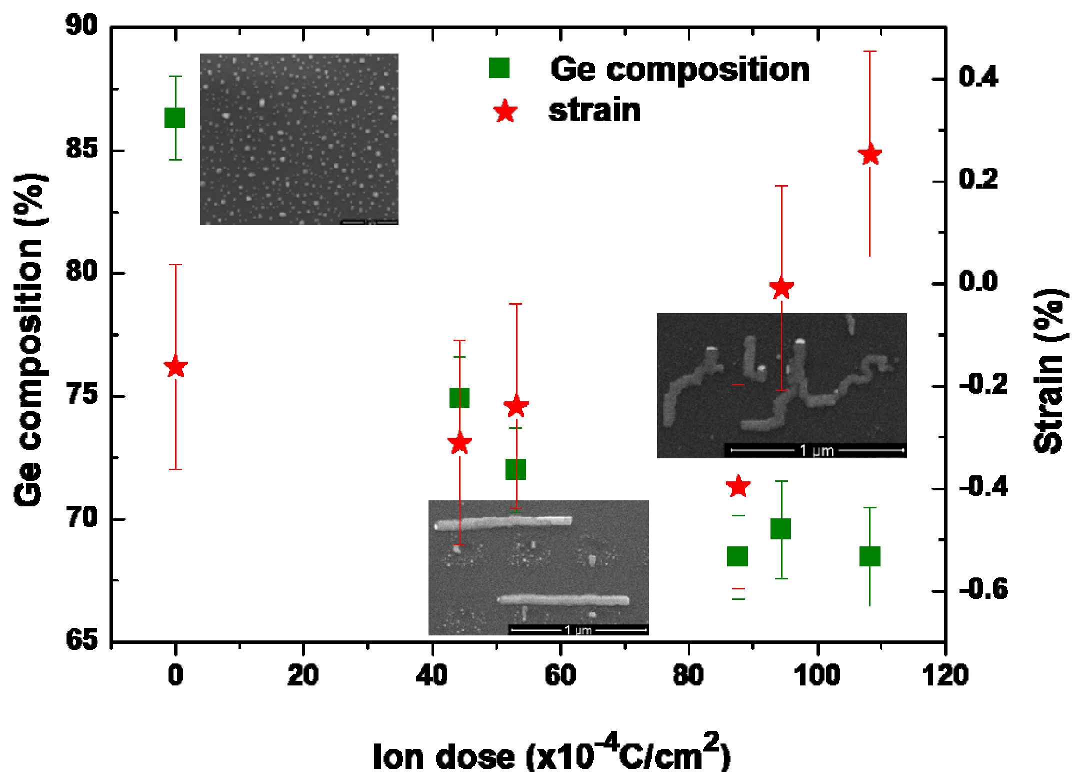

Figure 4.48. *Evolution of the nanostructure composition and strain as a function of ion dose employed to pattern the Si substrates. The value of the ion dose equal to zero corresponds to the unpatterned areas (Ge islands). The SEM images display the Ge nanostructures which were investigated by Raman spectroscopy.*

Differences in the Ge content between the nanowires formed inside the areas patterned with different ion doses were also investigated. As showed before, the patterns

and the Au ions play an important role on the formation of the Ge nanowires. Increasing the ion dose from $44x10^{-4}$ to $108x10^{-4}$ C/cm^2 the Ge composition was reduced in approximately ~7% (from 75% to 68%). The almost straight nanowires present higher Ge content (75%) compared to rolled up and kinked ones (68%). Regarding the strain profile it suffers less change from islands to nanowires.

4.4.3.3 High ion dose

The influence of high ion doses on the formation of the Ge nanostructures was also investigated. The increase of the ion doses implied, on the one hand, the formation of holes with larger depths and on the other hand an increased Au amount per hole. The ion doses used to pattern the different Si substrates orientations are in the range between $108x10^{-4}$ C/cm^2 and $240x10^{-4}$ C/cm^2. For these high ion doses the time needed to mill one hole was increased from 66 ms to 125 ms. Hole diameter evolution with the ion doses situated in this range is presented in figure 4.49a. Their diameter is increased approximately linearly from 200 to 260 nm, whereas the depth ranges between 8 and 40 nm. The AFM image recorded for a pattern with the hole average depth of 20 nm and a diameter around 240 nm is showed in figure 4.49b. The inset to figure 4.49b shows representative profiles of the holes demonstrating their uniformity and order. As a consequence of the employed annealing conditions (15 minutes at 550°C) the hole depth was increased five times, while the diameter was increased with 20 nm (from 225 to 245 nm).

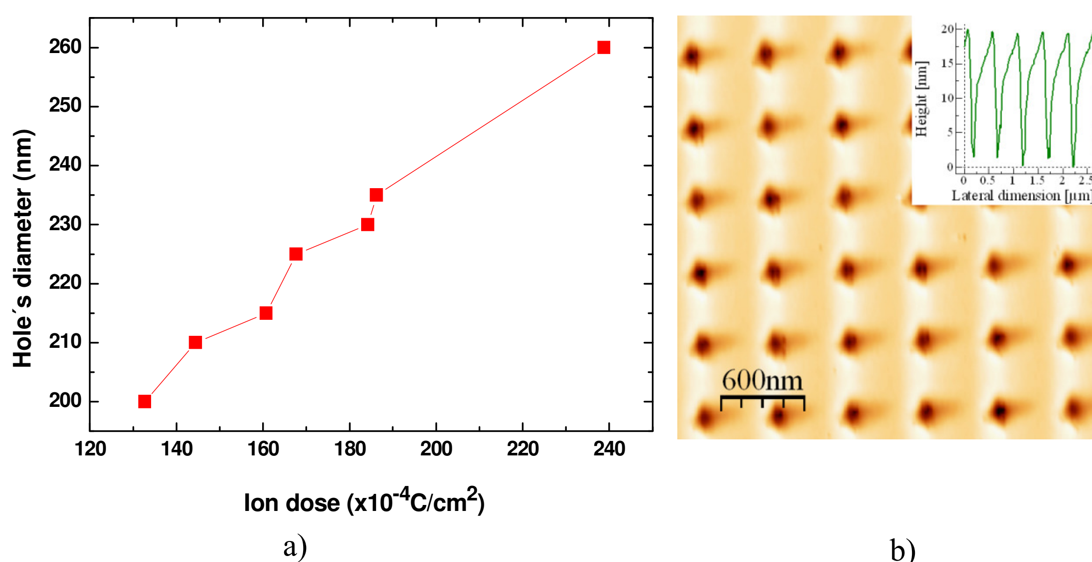

Figure 4.49. *a) Hole lateral diameter evolution with increasing ion dose. The holes were performed on a Si(001) oriented substrate. b) AFM image of a pattern performed using an ion dose of* $167.7x10^{-4}$ *C/cm*^{2}*. The image inset shows the profiles of the holes.*

The SEM and AFM images recorded after depositing 2 nm of Ge on a Si substrate area patterned using an ion dose of 167.7x10^{-4} C/cm^2 (20 nm holes initial depth) are presented in figure 4.50 a and b. The Au rich clusters presence inside the holes and in a reduced amount even in between the holes was confirmed by the backscattering SEM image (figure 4.50a). Their dimensions are reduced compared to the ones obtained inside the squares patterned using ion doses from the intermediate range.

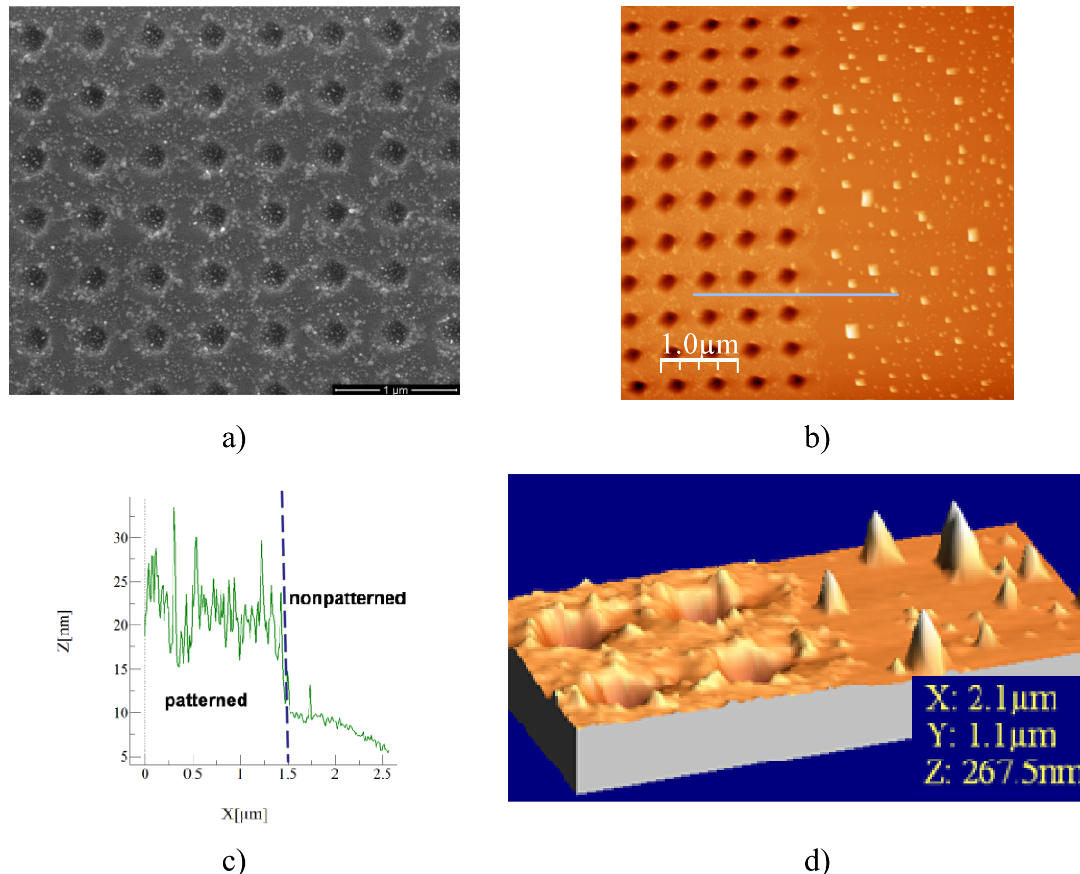

Figure 4.50. *a) SEM image recorded for a pattern obtained using a high ion dose (167.7x10^{-4} C/cm^2). The bright spots correspond to the AuSi clusters. b) AFM image recorded inside the pattern (left hand) and outside (right hand). Both SEM and AFM images were recorded after Ge depositions at 550℃. c) The profile recorded for both areas: patterned (left hand) and nonpatterned (right hand). d) 3D AFM image presenting both patterned (left hand) and unpatterned area (right hand).*

Outside the FIB patterned areas (figure 4.50 b – right hand) the formation of the Ge islands took place in the standard Stranski-Krastanow growth mode, the islands

present both pyramidal and dome shapes [60]. If we focus on the transition region, the islands formed near the patterned area present a pyramidal shape with square and rectangular bases. Inside the patterns the formation of islands or nanowires was not achieved. Compared to the low and intermediate ion doses, both hole depth and Au amount were increased. The evolution of the hole dimensions during the annealing stage, beside the increased Au amount, is partially responsible for the absence of the nanowires or ordered islands. The roughness induced by the FIB patterning limited the diffusion of material and increased the nucleation sites between the holes. The presence of Ge inside the patterned areas was confirmed by performing Raman measurements. However, the Ge content was reduced up to 60% compared to the composition of 87% of the islands formed on flat surfaces, outside the patterned areas. In between the holes, there is no flat surface (figure 4.50d), Ge nanostructures with heights up to 30 nm were formed. The same situation was found for all the patterns obtained using ion doses from this interval, pointing to the effect of the Au ions on nanostructures size reduction. Moreover, as can be seen in the profile obtained from the AFM image (figure 4.50c) inside the patterned area the region between the holes is much higher than outside the pattern one. A 3D AFM image of the same region of the sample where the profile was taken is shown in figure 4.54d. Inside the areas patterned with high ion doses, Ge grows layer by layer until a much larger thickness (7-8 nm) as compared to lower ion doses or unpatterned regions. This confirms the role played by the Au on increasing the critical thickness for islands formation. For intermediate ion doses, where the in plane Ge nanowires were found, the transition from patterned areas to unpatterned ones is not abrupt, both regions had the same height.

Furthermore, increasing the ion dose to 238.78×10^{-4} C/cm^2, two arrays of holes were performed with distance between the holes of 0.5 and 0.3 μm in order to investigate the AuSi clusters formation and density with the hole proximity. Consecutively, their influence on the formation of the Ge nanostructures was investigated. The combination of the FIB parameters used had as result an initial hole depth of 9 nm. The same annealing conditions were employed like in the previous cases, and hole depth was increased more than 10 times in this case. After Ge deposition, the differences recorded between the two patterns with different holes distances can be clearly seen in figure 4.51 from a to b.

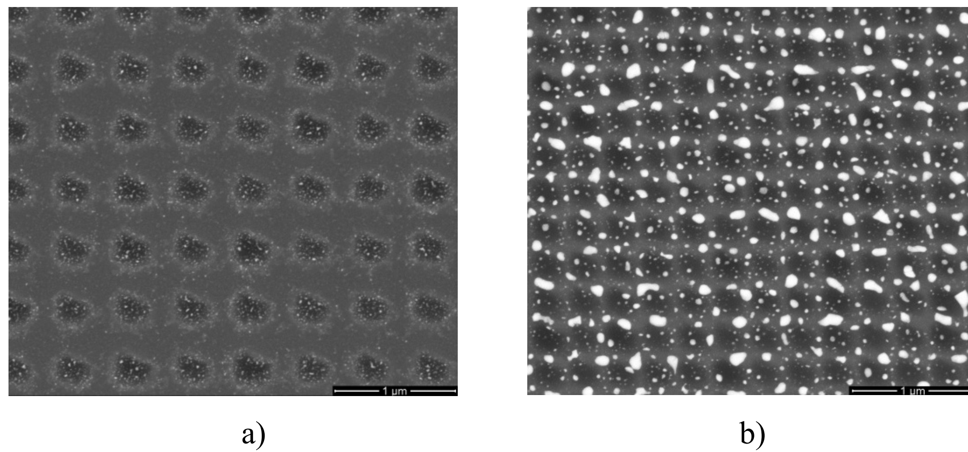

a) b)

Figure 4.51. *BS-SEM images for the patterns performed using a high ion dose (238.78x10^{-4} C/cm^{2}), and the distance between the holes was 0.5 µm (a) and 0.3 µm (b). Formation of Au rich clusters with different sizes was evidenced in both cases.*

The presence of the Au rich clusters was proved for both distances between the holes. Increasing this distance from 0.3 to 0.5 µm (figure 4.51 from b to a), the dimensions of the Au rich clusters were considerably reduced. Recorded backscattering SEM image shows only the formation of the AuSi clusters with large diameter (between 50 and 300 nm) when the distance between the holes was 0.3 µm. The droplets with larger sizes tend to form in between the holes as it can be seen in figure 4.51b, while inside the holes their diameter is significantly reduced. For these clusters sizes the growth of the Si or Ge nanowires was reported [55]. Using the same annealing (15 minutes at 550ºC) and deposition conditions (550ºC) like the ones used to obtain the Ge islands and the Ge nanowires, for these high ion doses the presence inside patterned regions of these two nanostructures was not proved. Independently of the distance between the holes and of the AuSi cluster dimensions, neither island nor nanowire growth took place inside the patterned areas.

4.5 Conclusions

We have developed a three-step process based on: i) high-resolution mass-filtered focused ion beam nanopatterning with Au^{2+} ions, ii) formation during annealing of the AuSi cluster catalysts and iii) nucleation and growth of the Ge nanostructures. First we investigated the FIB patterning conditions and the influence of some of the FIB parameters on the aspect ratio of the resulting pattern features. For this purpose we followed two different approaches: ultra fast grabbing process and holes patterning, based on mass filtered focused ion beam with Au^{2+} ions. We showed that the ion dose implanted within the patterns can be varied by changing the FIB sputtering conditions.

In the second step (ii), the influence of the annealing conditions (temperatures and times) on the FIB patterned substrates was investigated for both approaches: ultra fast grabbing and holes patterning. For single or multiple scans and holes milled with low ion doses no AuSi cluster formation was evidenced, independently of the employed annealing conditions. By increasing the ion doses in the intermediate and high ranges, the presence of the Au rich clusters inside the patterned areas was confirmed. It was proved that the patterning conditions influence the density of AuSi clusters and their lateral distribution.

In the next step (iii), after the MBE deposition, the differences between Ge nanostructures grown on the FIB patterned and nonpatterned regions were evidenced. The influence of the pixel numbers and speed setting at different growth temperatures on the formation and morphology of the Ge nanostructures was investigated. The formation of uniform and ordered Ge islands took place inside the FIB patterned areas. The Si(111) substrate orientation proved to be better for the order of the islands within the patterns. We proved that the Au presence inside the patterned areas plays an important part, beside other parameters, inducing a different Ge islands growth mode and morphology. Inside the hole patterned areas the dome shaped islands grow ordered between four holes and the pyramidal shaped ones are formed mainly inside the holes. Outside these areas, islands grown in the same conditions present both pyramidal and dome shapes and are randomly distributed. The effect of the Au was to reduce the island dimensions (both pyramids and domes) and to increase their aspect ratio. By using a constant ion dose and varying only the distance between the holes, we show that the big Ge islands grow between four Au rich areas (holes), and increasing the distance between the holes their order was decreased

and almost lost. Moreover, we demonstrated that as a consequence of the increasing ion dose, the order of the big Ge islands is slightly decreased, whereas the number of small Ge islands that were obtained inside the holes (Au rich areas) increased.

For the intermediate ion doses, Ge nanpwires (NWs) nucleate from the AuSi clusters, they first grow almost perpendicular to the surface and rapidly kink and crawl along the [110] directions of the substrate. Following existing models, we explain the NW growth mechanism by the strain-driven evolution of the energy requested to create new facets at the trijunction between solid, liquid and vapor. This energy includes surface energy and step edge energy, that both considerably evolve with strain. The strained NWs grow preferentially along stepped surface at low misorientations from [001]. After strain relaxation, the step edge energy becomes large enough to impede further growth of the NW pedestal and produce the kinking of the NW and subsequently their crawling and the growth along [110] directions with equilibrium facets on their sides. The influence of the nanopatterns on the NW morphology is also exhibited: the larger the surface roughness, the wavier the NWs. The waviness is attributed to a larger density of kinks coming from interactions with surface steps and kinks produced during FIB patterning. Raman measurements performed both inside and outside patterned areas show a decrease in the Ge amount within the nanowires as compared to the islands. The hole presence, their morphology and the Au amount increased the Si-Ge intermixing within the nanostructures formed inside the patterned areas.

For the higher ion doses, the formation of the AuSi clusters was evidenced, but no Ge nanostructures (ordered islands or nanowires) growth was demonstrated inside the patterned areas. The effect of the hole morphology beside the Au amount on increasing the Si-Ge intermixing was evidenced.

The three-step process developed provides for both approaches a promising way to investigate the processes of nucleation and growth of ordered arrays of nanostructures (islands or nanowires) in various experimental situations. This procedure can be applied for many systems with different deposited materials and substrates, being a path to follow in further investigations.

4.6 Bibliography

1. A. I. Yakimov, A. I. Nikiforov, A. V. Dvurechenskii, V. V. Ulyanov, V. A. Volodin, R. Groetzschel, *Nanotechnology* **2006**, *17*, 4743.
2. L. Vescan and T. Stoica, *J. App. Phys*. **2002**, *91*, 10119.
3. J. T. Robinson, J. A. Liddle, A. Minor, V. Radmilovic, D. O. Yi, P. A. Greaney, K. N. Long, D. C. Chrzan, O. D. Dubon, *Nano Letters* **2005**, *5(10)*, 2070.
4. M. Grydlik, M. Brehm, F. Hack, H. Groiss, T. Fromherz, F. Schäffler, G. Bauer, *New Journal of Physics* **2010**, *12*, 063002.
5. P. Chen, Y. Fan, Z. Zhong, *Nanotechnology* **2009**, *20*, 095303.
6. M. Bollani, E. Bonera, D. Chrastina, A. Fedorov, V. Montuori, A. Picco, A. Tagliaferri, G. Vanacore, R. Sordan, *Nanoscale Res. Lett*. **2010**, *5*, 1917.
7. J. Zhang, A. Rastelli, O. G. Schmidt, G. Bauer, *App. Phys. Lett*. **2010**, *97*, 203103.
8. H. Minoda, K.Yagi, *J. Crystal Growth* **1996**, *163*, 48.
9. J. T. Robinson, J. A. Liddle, A. Minor, V. Radmilovic, O. D. Dubon, *J. Cryst. Growth* **2006**, *287*, 518.
10. A. Karmous, A. Cuenat, A. Ronda, I. Berbezier, S. Atha, R. Hull, *J. Appl. Phys*. **2004**, *85*, 6401.
11. C. D. Poweleit, C.-W. Hu, I. S. T. Tsong, J. Tolle, J. Kouvetakis, *J. Appl. Phys*. **2007**, *101*, 114312.
12. A. Portavoce, M. Kammler, R. Hull, M. C. Reuter, M. Copel, F. M. Ross, *Phys. Rev. B* **2004**, *70*, 195306.
13. A. Karmous, I. Berbezier, A. Ronda, R. Hull, J. Graham, *Surface Science* **2007**, *601*, 2769.
14. A. Karmous, I. Berbezier, A. Ronda, *Phys. Rev. B* **2006**, *77*, 075323.
15. K. Brunner, *Rep. Prog. Phys*. **2002**, *65*, 27.
16. A. Pascale, I. Berbezier, A. Ronda, P. C. Kelires, *Phys. Rev. B* **2008**, *77*, 075311.
17. A. Kramer, M. Albrecht, T. Boeck, T. Remmele, P. Schramm, R. Fornari, *Superlattices and Microstructures* **2009**, *46*, 277.
18. T. Burchhart, C. Zeiner, A. Lugstein, C. Henkel, E. Bertagnolli, *Nanotechnology* **2011**, *22,* 035201.

19. B. Yu, X. H. Sun, G. A. Calebotta, G. R. Dholakia, M. Meyyappan, *J. Cluster Science* **2006**, *17(4)*, 579.

20. N. S. Lewis, *Science* **2007**, *315*, 798.

21. Y. Y. Wu, P. D. Yang, *J. Am. Chem. Soc.* **2001**, *123*, 3165.

22. S. P. Ge, K. L. Jiang, X. X. Lu, Y. F. Chen, R. M. Wang, S. S. Fan, *Adv. Mater*. **2005**, *17*, 56.

23. E. Dailey, J. Drucker, *J. Appl. Phys.* **2009**, *105*, 064317.

24. H. F. Yan, Y. J. Xing, Q. L. Hang, D. P. Yu, Y. P. Wang, J. Xu, Z. H. Xi, S. Q. Feng, *Chem. Phys. Lett*. **2000**, *323*, 224.

25. R. Q. Zhang, Y. Lifshitz, S. T. Lee, *Adv. Mater*. **2003**, *15*, 635.

26. I. Berbezier, J. P. Ayoub, L. Favre, A. Ronda, L. Morresi, N. Pinto, *Surface Sci.* **2011**, *605*, 7.

27. Y. Wang, V. Schmidt, S. Senz, U. Gösele, *Nat. Nanotechnol*. **2006**, *1*, 186.

28. S. Y. Chen, L. J. Chen, *Thin Solid Films* **2006**, *508*, 222.

29. C.-Y. Chen, C.-S. Wu, C.-J. Chou, T.-J. Yen, *Adv. Mat*. **2008**, *20*, 3811.

30. K. Q. Peng, J. J. Hu, Y. J. Yan, Y. Wu, H. Fang, Y. Xu, S. T. Lee, J. Zhu, *Adv. Funct. Mater.* **2006**, *16*, 387.

31. J. D. Holmes, K. P. Johnston, R. C. Doty, B. A. Korgel, *Science* **2000**, *287*, 1471.

32. D. P. Yu, C. S. Lee, I. Bello, X. S. Sun, Y. H. Tang, G. W. Zhou, Z. G. Bai, Z. Zhang, S. Q. Feng, *Solid State Commun*. **1998**, *105*, 403.

33. N. J. Quitoriano, T. I. Kamins, *Nanotechnology* **2011**, *22*, 065201.

34. B. V. Kamenev, V. Sharma, L. Tsybeskov, T. I. Kamins, *Phys. Stat. Sol. (a)* **2005**, *202(14)*, 2753.

35. Y. F. Zhang, Y. H. Tang, H. Y. Peng, N. Wang, C. S. Lee, I. Bello, S. T. Lee, *Appl. Phys. Lett.* **1999**, *75(13)*, 1842.

36. S. Kodambaka, J. B. Hannon, R. M. Tromp, F. M. Ross, *Nano Letters* **2006**, *6(6)*, 1292.

37. E. Dailey, P. Madras, J. Drucker, *Appl. Phys. Lett.* **2010**, 97, 143106.

38. P. C. McIntyre, H. Adhikari, I. A. Goldthorpe, S. Hu, P. W. Leu, A. F. Marshall, C. E. D. Chidsey, *Semicond. Sci. Technol*. **2010**, *25*, 024016.

39. P. Nguyen, H. T. Ng, M. Meyyappan, *Adv. Matter* **2005**, *17(5)*, 549.

40. F. M. Ross, J. Tersoff, M. C. Reuter, *Phys. Rev. Lett.* **2005**, *95*, 146104.

41. V. Schmidt, S. Senz, U. Gösele, *Appl. Phys*. A **2005**, *80*, 445.

42. A. Ishizaka, Y. Shiraki, *J. Electrochem. Soc*. **1986**, *133*, 666.

43. X. L. Li, G. Ouyang, G. W. Yang, *Eur. Phys. J. B* **2008**, *62*, 295.

44. A. Klimovskaya, A. Sarikov, Y. Pedchenko, A. Voroshchenko, O. Lytvyn, A. Stadnik, *Nanoscale Research Letters* **2011**, 6:151.

45. M. Tomitori, K. Watanabe, M. Kobayashi, O. Nlshlkawa, *App. Surf. Sci.* **1994**, *76/77*, 322.

46. H. Okamoto, T. B. Massalski, in *Binary Alloy Phase Diagrams* Vol. 1 (Materials Park, OH, ASM International) **1990**.

47. M. F. Castez, *J. Phys.: Condens. Matter.* **2010**, *22*, 345007.

48. R. Hiruta, H. Kuribayashi, S. Shimizu, K. Sudoh, H. Iwasaki, *Applied Surface Science* **2004**, *237*, 63.

49. M. Kitayama, T. Narushima, A. M. Glaeser, *J. Am. Ceram. Soc.* **2000**, *83,* 2572.

50. H. Kuribayashi, R. Hiruta, R. Shimizu, K. Sudoh, H. Iwasaki, *J. Vac. Sci. Technol. A* **2003**, *21(4)*, 1279.

51. K. Sudoh, H. Iwasaki, R. Hiruta, H. Kuribayashi, R. Shimizu, *J. Appl. Phys*. **2009**, *105*, 083536.

52. H. Minoda, K. Yagi, *Phys. Rev. B*. **1999**, *59(3)*, 2363.

53. P. Werner, N. D. Zakharov, G. Gerth, L. Schubert, U. Gösele, *Int. J. Mat. Res.* **2006**, *97*, 1008.

54. T. Ogino, H. Hibino, Y. Homma, *App. Surf. Sci*. **1996**, *107*, 1.

55. N. D. Zakharov, P. Werner, G. Gerth, L. Schubert, L. Sokolov, U. Gösele, *J. Cryst. Growth* **2006**, *290*, 6.

56. B. Ressel, K. C. Prince, S. Heun, Y. Homma, *J. Appl. Phys*. **2003**, *97(3)*, 3886.

57. J. B. Hannon, S. Kodambaka, F. M. Ross, R. M. Tromp, *Nature* **2006**, *440*, 69.

58. L. Vescan, *J. Phys.: Condens. Matter*. **2002**, *14*, 8235.

59. C. Teichert, *Physics Reports* **2002**, *365*, 335.

60. R. S. Williams, G. Medeiros-Ribeiro, T. I. Kamins, D. A. A. Ohlberg, *J. Phys. Chem. B* **1998**, *102(48)*, 9605.

61. J. Stangl, V. Holý, G. Bauer, *Reviews of Modern Physics* **2004**, *76*, 725.

62. O. G. Schmidt, C. Lange, K. Eberl, O. Kienzle, F. Ernst, *Appl. Phys. Lett*. **1997**, *71(16)*, 2340.

63. A. Bernardi, J. O. Osso, M. I. Alonso, A. R. Goni, M. Garriga, *Nanotechnology* **2006**, *17*, 2602.

64. X. Zhoua, B. Shia, Z. Jianga, W. Jianga, D. Hua, D. Gonga, Y. Fana, X. Zhanga, X. Wanga, Y. Li, *Thin Solid Films* **2000**, *369*, 92.

65. P. S. Chen, Z. Pei, Y. H. Peng, S. W. Lee, M.-J. Tsai, *Materials Science and Engineering B* **2004**, *108*, 213.

66. R. Bergamaschini, F. Montalenti, L. Miglio, *Nanoscale Res. Lett*. **2010**, 5:1873.

67. L. Nurminen, A. Kuronen, K. Kaski, *Phys. Rev. B* **2001**, *63*, 035407.

68. H. Hu, H. J. Gao, F. Liu, *Phys. Rev. Lett*. **2008**, *101*, 216102.

69. Z. Zhong, P. Chen, Z. Jiang, G. Bauer, *Appl. Phys. Lett*. **2008**, *93*, 04310.

70. C. B. Li, K. Usami, H. Mizuta, S. Oda, *J. Appl. Phys*. **2009**, *106*, 046102.

71. J. W. Dailey, J. Taraci, T. Clement, D. J. Smith, J. Drucker, S. T. Picraux, *J. Appl. Phys*. **2004**, *96(12)*, 7556.

72. V. G. Dubrovskii, N. V. Sibirev, G. E. Cirlin, J. C. Harmand, V. M. Ustinov, *Physical Review* E **2006**, *73*, 021603-1.

73. C. Nishimura, G. Imamura, M. Fujii, T. Kawashima, T. Saitoh, S. Hayashi, *App. Phys. Lett*. **2008**, *93*, 203101.

74. H. J. Fan, M. Zacharias, *J. Mater. Sci. Technol*. **2008**, *24(4)*, 589.

75. M. Koto, A. F. Marshall, I. A. Goldthorpe, P. C. McIntyre, *Small* **2010**, *6(9)*, 1032.

76. K. W. Schwarz, J. Tersoff, ***Phys. Rev. Lett.*** 2009**, *102(20)*,** 206101-1.

77. K. W. Schwarz, J. Tersoff, ***Nano Lett.*** 2011**, *11*,** 316.

78. V. B. Shenoy, L. B. Freund, *Journal of the Mechanics and Physics of Solids* **2002**, ***50(9)*, 1817.**

79. F. Tuinstra, P. M. L. O. Scholte, W. I. Rijnders, A. J. van den Berg, *Surf. Sci*. **1994**, *317*, 58.

80. G.-H. Lu, M. Cuma, F. Liu, *Phys. Rev. B* **2005**, *72*, 125415.

81. E. F. Pecora, A. Irrera, P. Artoni, S. Boninelli, C. Bongiorno, C. Spinella, F. Priolo, *Electrochem. Solid State Lett*. **2010**, *13*, K53.

82. J. H. Woodruff, J. B. Ratchford, I. A. Goldthorpe, P. C. McIntyre, C. E. D. Chidsey, *Nanoletters* **2007**, *7*, 1637.

83. J.-N. Aqua, T. Frisch, *Phys. Rev. B* **2010**, *82*, 085322.

84. N. Motta, F. Rosei, A. Sgarlata, G. Capellini, S. Mobilio, F. Boscherini, *Mater. Sci. Engineering* **2002**, *B88*, 264.

85. A. Wolfsteller, N. Geyer, T.-K. Nguyen-Duc, P. Das Kanungo, N. D. Zakharov, M. Reiche, W. Erfurth, H. Blumtritt, S. Kalem, P. Werner, U. Gösele, *Thin Solid Films* **2010**, *518*, 2555.

86. J. A. Venables, *Physica A* **1997**, *239*, 35.

87. Z. Zhang, M. G. Lagally, *Science* **1997**, *276*, 377.

88. B. V. Kamenev, V. Sharma, L. Tsybeskov, T. I. Kamins, *Phys. Stat. Sol. (a)* **2005**, *202(14)*, 2753.

Acknowledgments

I would like to take this opportunity to express my sincere gratitude to my supervisors Dr. Isabel Alonso and Dr. Alejandro Goñi, for offering me the opportunity to pursue my Ph.D in the group of Nanostructured Optoelectronic Materials. The tremendous guidance and support in many aspects from them have been invaluable for the project work. They always had their door open whenever I need help and advice. It has been always fruitful to discuss with them. I thank them kindly for sharing their scientific experience starting from the planning of experiments to the proper presentation of the results.

I would like to thank to Dr. Miquel Garriga for his guidance and support throughout my thesis project, for his fruitful and interesting discussions and authentic scientific interest.

My gratitude goes to Dr. Sebastian Reparaz for his time, patience, useful discussions (scientific ones, but not only) especially in the last year of my thesis. He probably does not know how much his support and encouragement mean to me. Thank you Sebas for everything.

Many thanks to Dr. Eniko Gyorgy and Dr. Angel Perez del Pino for their collaboration, fruitful scientific discussions and their support and friendship during my thesis.

I also would like to thank my colleagues of the group of Nanostructured Optoelectronic Materials for creating such a great working environment. It was truly a pleasure working with them: Dr. Mariano Campoy-Quiles, Dr. Christian Müller, Dr. Pablo O. Vaccaro, Malte Schmidt, Lucas Muniz, Ignasi Burgués, Ferran Barroso and Jose Luis Moreno. I would like to thank to the former colleagues from the group: Alessandro Bernardi, Dr. Paul Lacharmoise, Dr. Ovidio Peña Rodriguez, and Mahdieh Aghamohammadi.

I would like to thank all the people who worked in the Institut de Ciencia de Materials de Barcelona (ICMAB - CSIC) who supported me during the time I have spent here.

I also thank to Dr. Javier Rodríguez Viejo for accepting to be the tutor of this thesis.

Special thanks go to Dr. Isabelle Berbezier the head of the group Epitaxial Semiconductor Nanostructures, Institute of Microelectronics Materials and Nanosciences of Provence (IM2NP), Marseille - France for receiving me in her team and giving me the opportunity to use all the equipments from her lab. Isabelle, thank you for supporting and helping me. Part of the results presented in this thesis is the product of the fruitful collaboration with her team. Thanks to all the members of the Epitaxial Semiconductor Nanostructures group for their support and friendship during the time spend in Marseille.

Many thanks go to the Romanian community from the Institut de Ciencia de Materials de Barcelona. In the period spend in ICMAB I had the opportunity to meet and to share pleasant moments with: Corina, Costana, Angela, Roxana, Ani, Radu, Anca, Ana, Marius, Oana and Adnana. During these years they supported, helped and encouraged me, changing my mood any time I needed.

Finally, I would like to express my deepest gratitude to my family, for their care and support and for loving me enough to let me follow my own way. Special thanks to my ***mother***, for her love, encouragement and support all along. She is always beside me no matter what I am facing. Vă mulţumesc!

List of publications and conferences attended during my PhD

I. Publications

1. Probing local strain and composition in Ge nanowires by means of tip - enhanced Raman scattering

J. S. Reparaz, N. Peica, R. Kirsten, A. R. Goñi, G. Callsen, M. R. Wagner, G. Callsen, M. I. Alonso, M. Garriga, **I. C. Marcus**, I. Berbezier, A. Ronda, J. Maultzsch, C. Thompson, A. Hoffman

Submitted to ***Nannoscale*** (2012)

2. Influence of Ge nanoclustering on the composition and strain determination by Raman scattering of $Si_{1-x}Ge_x$/Si alloys

J. S. Reparaz, **I. C. Marcus**, A. R. Goñi, M. Garriga, M. I. Alonso

Submitted to ***J. App. Phys.*** (2011)

3. In-plane epitaxial growth of self-assembled Ge nanowires on Si substrates patterned by a focused ion beam

I. C. Marcus, I. Berbezier, A. Ronda, M. I. Alonso, M. Garriga, A. R. Goñi, E. Gomes, L. Favre, A. Delobbe, P. Sudraud

Cryst. Growth Des., *2011*, 11(7), 3190

4. Effects of pulsed laser radiation on epitaxial self-assembled Ge quantum dots grown on Si substrates

A. Perez del Pino, E. Gyorgy, **I. C. Marcus**, J. Roqueta, M. I. Alonso

Nanotechnology, *2011*, 22, 22(29):295304

5. Evidence of quantum confinement effects on interband optical transitions in Si nanocrystals

M. I. Alonso, **I. C. Marcus**, M. Garriga, A. R. Goni, J. Jedrzejewski, I. Balberg

Phys. Rev. B, *2010*, 82(4), 45302

6. Structural studies of copper doped 2TeO2-PbO-Ag2O glass by FT-IR and Raman spectroscopies

R. C. Lucacel, **I. C. Marcus**, I. Ardelean, O. Hulpus

Eur. Phys. J. Appl. Phys., *2010*, 51, 30901

II. Conferences attended

1. **Probing local strain and composition in Ge nanowires by means of tip - enhanced Raman scattering**

J. S. Reparaz, N. Peica, R. Kirsten, A. R. Goñi, G. Callsen, M. R. Wagner, G. Callsen, M. I. Alonso, M. Garriga, **I. C. Marcus**, I. Berbezier, A. Ronda, J. Maultzsch, C. Thompson, A. Hoffman

17th International Winterschool on New Developments in Solid State Physics, 12 - 17 February, 2012, Mauterndorf, Austria

Poster presentation

2. **Self assembled Ge nanowires grown on FIB nanopatterns**

I. C. Marcus, I. Berbezier, A. Ronda, M. I. Alonso, M. Garriga, A. R. Goñi, E. Gomes, L. Favre, A. Delobbe, and P. Sudraud

E-MRS ICAM IUMRS 2011 Spring Meeting, 9-13 May, Nice, France

Oral presentation

3. **Effects of pulsed laser radiation on epitaxial self-assembled Ge quantum dots grown on Si substrates**

A. Perez del Pino, E. Gyorgy, **I. C. Marcus**, J. Roqueta, and M. I. Alonso

E-MRS ICAM IUMRS 2011 Spring Meeting, 9-13 May, Nice, France

Poster presentation

4. **Self assembled Ge nanostructures grown on FIB nanopatterned Si substrates**

I. C. Marcus, I. Berbezier, A. Ronda, M. I. Alonso, M. Garriga, A. R. Goñi, E. Gomes, L. Favre, A. Delobbe, and P. Sudraud

3rd International Conference on Nanostructures SElf-Assembly NanoSEA 2010, Cassis, France, 28 June - 2 July 2010

Oral presentation

5. **Self assembled Ge nanostructures grown on FIB nanopatterned Si substrates**
I. C. Marcus, I. Berbezier, A. Ronda, M.I. Alonso, M. Garriga, A.R. Goñi, E. Gomes, L. Favre, A. Delobbe, and P. Sudraud
8th International Workshop on Epitaxial Semiconductors on Patterned Substrates and Novel Index Surfaces, Como (Italy), 14-18 June 2010
Oral presentation

6. **FIB nanopatterning for SiGe nanostructures self-assembly on Si substrate**
G. Amiard, I. Berbezier, M. Aouassa, L. Favre, A. Ronda, **I. C. Marcus,** and I. Alonso
6th International Workshop on Functional and Nanostructured Materials FNMA09, 23-30 September 2009, Sulmona-L'Aquila, Italy
Poster presentation

7. **Boron delta doping layers as templates for deposition of Ge quantum dots on Si**
I. C. Marcus, L. Garzón, M. Schmidt, M. Garriga, M. I. Alonso, A. R. Goñi and C. Ocal
Second Spanish Workshop on Nanolithography, 10-12 November, 2008, Bellaterra, Barcelona, Spain
Poster presentation

8. **Dependence of the Ge nanostructure formation on B delta doping during MBE growth**
L. Garzon, **I. C. Marcus**, M. Schmidt, M. Garriga, M. I. Alonso, A. R. Goñi and C. Ocal
VI Congreso Español de microscopia de fuerzas y de efecto túnel; Fuerzas y Túnel 2008, 22-25 de Septiembre, 2008, Segovia, Spain
Poster presentation